BREAKUP OF LIQUID DROPLETS

A Dissertation
Presented to
The Academic Faculty

by

Prashant Khare

In Partial Fulfillment
of the Requirements for the Degree
Doctor of Philosophy in the
School of Aerospace Engineering

Georgia Institute of Technology
May 2014

BREAKUP OF LIQUID DROPLETS

Approved by:

Professor Vigor Yang, Advisor
School of Aerospace Engineering
Georgia Institute of Technology

Professor Ben T. Zinn
School of Aerospace Engineering
Georgia Institute of Technology

Professor Suresh Menon
School of Aerospace Engineering
Georgia Institute of Technology

Professor Caroline L. Genzale
School of Mechanical Engineering
Georgia Institute of Technology

Professor Timothy C. Lieuwen
School of Aerospace Engineering
Georgia Institute of Technology

Date Approved: 8 November 2013

dedicated to my beloved parents

and

to the inquisitiveness of the human mind

PREFACE

This thesis is a product (almost a tangent) of a Multidisciplinary University Research Initiative (MURI), sponsored by the US Army Research Office. The goal of the project was to explore the physics (and chemistry) governing the spray and combustion of gelled hypergolic propellants. We started the project by studying a very fundamental problem of a non-reacting liquid jet in quiescent environment using a traditional Eulerian-Lagrangian framework but quickly realized that there are no reliable models for droplet dynamics in the literature which can be used with confidence to study practical problems of interest. Probing deeper into the literature revealed that even the physics governing droplet behavior is elusive. We had a choice to use an Eulerian-Eulerian framework and conduct direct numerical simulations (DNS) to resolve the full range of length and time scales involved in the problem but decided otherwise because of its cost prohibitive nature (even without chemical reactions!). A quick order of magnitude study and a sample numerical calculation suggested that, perhaps it would be wiser to use the Eulerian-Eulerian framework to explore the underlying physics and develop models for droplet fragmentation, collision and splashing using multiphase DNS studies, and then use those correlations in the Eulerian-Lagrangian framework to attack the large-scale problem. This approach seemed tractable and not as cost prohibitive as a full scale DNS calculation. I undertook this opportunity to explore the physics behind single droplet breakup and the result is this thesis. In this thesis, we have tried to address some of the outstanding issues confronting the spray community, specifically relevant to single droplet deformation and breakup from a purely hydrodynamics perspective, without considering vaporization and chemical reactions.

ACKNOWLEDGEMENTS

This has been a intellectually stimulating and personally enriching journey over the last few years and it would not have been possible without the support of a lot of people. I would like to acknowledge their support and thank each one of them as I begin the next chapter of my life and enter the *real world*. First and foremost, I would like to thank my advisor, Prof. Vigor Yang, for giving me an opportunity to work under his guidance. It has been a real privilege working with him. He has been a constant source of inspiration and his support, encouragement and comments have been instrumental throughout the course of my graduate studies.

I would also like to express my sincere thanks to Prof. Ben Zinn, Prof. Suresh Menon, Prof. Timothy Lieuwen and Prof. Caroline Genzale for taking out time to serve on my Ph.D. thesis committee and providing valuable suggestions and recommendations. I also want to express my gratitude to Prof. S. S. Gokhale, my undergraduate advisor, who has been a great mentor over the years and who encouraged and inspired me to join graduate school. I would also like to acknowledge the financial support by the US Army Research Office who funded my research under the Multidisciplinary University Research Initiative (MURI), contract number W911NF-08-1-0124. I am also thankful to Dr. Stéphane Popinet for allowing me to use his VOF and AMR algorithms.

I cannot undermine the support of my friends and lab mates, who have contributed to the completion of my thesis. I found wonderful friends in Nicolas Reveles, Rajiv Shenoy and Dolly Sinha during the course of my Ph.D. Their support was most essential and I couldn't have finished my thesis without them. They were there for me at each and every step and kept me sane by humoring me. I cannot forget to

thank my close friends from college, Gaurav Jain and Hitesh Dhawan, who have been great buddies for a long time now and whose support has been vital for me to pursue my dreams.

Last but definitely not the least, I owe this Ph.D. thesis to my parents and my sister. Their love and support throughout my life has been the driving force which has kept me focused on my goals. My parents have been my role models since childhood and none of this would have been possible without their blessings.

TABLE OF CONTENTS

LIST OF TABLES

LIST OF FIGURES

NOMENCLATURE

$(.)_{cc}$	Cell centered
$(.)_{fc}$	Face centered
δ	Dirac delta function
Γ	Adsorption
κ	Local curvature
κ_b	Boltzmann constant = $1.3806488 \times 10^{-23} m^2 kg s^{-2} K^{-1}$
κ_e	Eotvos constant = $2.1 \times 10^{-7} J mol^{-2/3} K^{-1}$
λ	Mean free path
λ_c	Critical wavelength
λ_j	Wavelength for maximum instability of a cylindrical liquid jet
μ	Dynamic viscosity
μ_n	Chemical potential of a species, n
∇_S	Surface gradient operator
$\overline{v}$	Molar volume
ρ	Density
σ	Surface tension
θ	Fraction of the surface covered

$\triangle t$	Time step
$\triangle$	Cube length
$\widehat{i}$	Unit vector in x direction
$\widehat{j}$	Unit vector in y direction
$\widehat{j}$	Unit vector in z direction
$\widehat{\mathbf{u}}$	Normal velocity
$\widehat{t}_{\perp}$	Unit vector normal to the solid boundary
$\widehat{t}_{\perp}$	Unit vector tangential to the solid boundary
$\widehat{t}$	Family of unit tangent vectors to the interface
$\widetilde{\tau}$	Shear stress tensor
A	Area
a	Speed of sound, m/s
A_m	Molar surface
$A_{frontal}$	Frontal area of a sphere of equivalent surface area
AMR	Adaptive mesh refinement
$b(T)$	Adsorption coefficient
C_d	Coefficient of drag
CFL	CourantFriedrichsLewy
CSF	Continuum surface force
d_j	Jet diameter

F	Free energy
f	Volume fraction
f_i^d	Steady-state drag force
f_i^l	Lift force
f_i^v	Virtual mass force
$f_i^{\nabla p}$	Force due to the local pressure gradient and the shear-stress of the carrier phase
FFT	Fully threaded tree
HF	Height function
I	Identity tensor
LJ	Lennard-Jones
m	Consistency index
n	Flow behavior index
p	Pressure
p_{cr}	Critical pressure
p_r	Reduced pressure
Q	Partition function
R_1 and R_2	Principal radii of curvature
s_s	Surface entropy per unit area
$SAMR$	Structured adaptive mesh refinement

SPC/E	Extended simple point charge model
T_{cr}	Critical temperature
u_j	Jet velocity
v_{ad}	Volume of gas adsorbed
x	Mole fraction
$\mathbf{F_{st}}$	Surface tension force
$\mathbf{n}$	Interface normal
$\mathbf{u}$	Velocity vector
BOAS	Beads-on-a-string

SUMMARY

Liquid droplet breakup and dynamics is a phenomena of immense practical importance in a wide variety of applications in science and engineering. Albeit, researchers have been studying this problem for over six decades, the fundamental physics governing droplet deformation and fragmentation is still unknown, not to mention the formulation and development of generalized correlations to predict droplet dynamics. The presence of disparate length and time scales, along with the complex unsteady physics, makes this a formidable problem, theoretically, experimentally and computationally. One of the important applications of interest and the motivation for the current research is a liquid fueled propulsion device, such as diesel, gas turbine or rocket engine. Droplet vaporization and ensuing combustion is accelerated if the droplet size is smaller, which makes any process leading to a reduction in drop size of prime importance in the combustion system design. This thesis is an attempt to address several unanswered questions currently confronting the spray community. Unanswered questions include identification and prediction of breakup modes at varying operating conditions, quantitative description of fundamental processes underlying droplet breakup and generalized correlations for child droplet size distributions and drag coefficient associated with the deformation and fragmentation of Newtonian and non-Newtonian fluids.

The present work is aimed at answering the above questions by investigating the detailed flowfield and structure dynamics of liquid droplet breakup process and extracting essential physics governing this complex multiphase phenomena. High-fidelity direct numerical simulations are conducted using a volume-of-fluid (VOF)

interface capturing methodology. To isolate the hydrodynamic mechanisms dictating droplet breakup phenomena, evaporation and compressibility are neglected, and numerical studies are performed for incompressible fluids at isothermal conditions.

For Newtonian fluids, four different mechanisms are identified- oscillatory, bag, multimode and shear breakup modes. Various events during the deformation and fragmentation process are quantitatively identified and correlations are developed to predict the breakup mechanisms and droplet size distributions for a broad range of operating conditions. It was found that for $We > 300$ and $Oh < 0.1$ for $\rho_l/\rho_g = 8.29$, the child droplet size distributions can be modeled by a log-normal distribution. A correlation to predict the sauter mean diameter, d_{32}, is also developed, given by $\frac{d_{32}}{D} = \frac{8We^{-0.72}}{C_d}$.

Temporal evolution of momentum balance and droplet structure are also used to calculate the drag coefficient at each time step from first principles. Results show that the drag coefficient first increases to a maximum as the droplet frontal area increases and then decreases at the initiation of breakup. The drag coefficient reaches a steady value at the end of droplet lifetime, corresponding to the momentum retained by the droplet. A correlation to predict the time-mean drag coefficient given by, $\frac{C_d}{C_{d,0}} = 2We^{-0.175}$, is developed, which indicates that the time averaged drag coefficient decreases with Weber number.

The motivation to study non-Newtonian liquid droplet breakup stems from the various advantages gelled propellants offer as compared to traditional liquid or solid propellants in combustion systems, particularly in rocket engines. It was found that the breakup behavior of pseudoplastic, non-Newtonian liquids is drastically different as compared to Newtonian droplets. Several flow features commonly exhibited by non-Newtonian fluids are observed during the breakup process. The breakup initiates with the formation of beads-in-a-string due to the non-Newtonian nature of the fluid under consideration. This is followed by rapid rotation of the droplet with the appearance

of helical instability and liquid budges, which forms the sites for primary and satellite droplet shedding. Child droplet size distribution are also examined and it is found that a Gaussian curve universally characterizes the droplets produced during non-Newtonian droplet breakup process.

To put all things in perspective, the objectives of the thesis were two folds: (1) elucidate breakup physics for Newtonian and non-Newtonian liquid droplet deformation and breakup, and (2) develop correlations which can be used in an Eulerian-Lagrangian framework to study large-scale engineering problems. It is hoped that this research contributed to droplet breakup and dynamics literature by providing a more thorough and quantitative understanding of the breakup phenomena of liquid droplets and furnished models which can be used in future research endeavors.

CHAPTER I

INTRODUCTION

1.1 Overview and Motivation

Multiphase flows are ubiquitous in nature. Our most common experiences in daily life revolve around free surface multiphase flows- water jets from the shower heads, sprinklers in the garden, water bodies such as lakes, rivers and oceans. Another prevalent example of multiphase flows, which we all are familiar with, is cloud formation and subsequent rain/snow fall. This is perhaps one of the most complicated natural phenomenon whose mysteries still eludes us. Recent work by Villermaux & Bossa (2009) & Villermaux (2007) has emphasized the importance of single droplet fragmentation and proposed how that information can be used to quantitatively understand the overall size distribution of raindrops. To add to the complexity, occasional occurrence of cloud bursting at different parts of the globe, acts as an anomaly and needs to be explored. Other naturally occurring multiphase phenomena, which are of significant importance are geophysical flows and includes the fluid dynamics of glaciers, volcanoes and magma oceans. On the industrial scale, multiphase flows and droplet dynamics, in particular, play an exceedingly important role. Mineral ore such as iron, aluminium, copper, which are mined in huge quantities every year, are required to flow at some stage during their extraction. Fluidized beds, bubbly flow in nuclear reactors, inkjet printing, gas-particle flows in chemical reactors, cavitating pumps and turbines, electrophotography used in copy machines, laser and LED printers are a few examples of process technologies where multiphase flows plays a vital role. The significance of multiphase flows with regards to air pollution has been well recognized, especially during recent times. Of particular practical interest (concern) is the

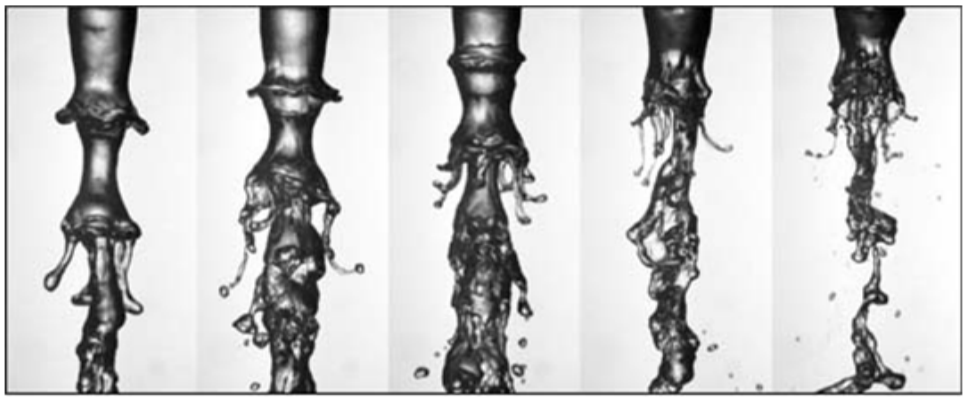

Figure 1.1. Snapshots of an 8-mm-diameter, slow (0.6 m/s) water jet destabilized by a coaxial fast air stream. Development of the axisymmetric shear instability, digitations at the wave crests, and ligament formation for air velocities increasing from 20 to 60 m/s are shown (Villermaux, 2007). Reproduced with permission. ©Annual Reviews.

pollution created by liquid-fueled propulsion devices such as automobiles, gas turbine engines in aircraft and power plants, where droplet breakup, vaporization and ensuing combustion is responsible for creating gases and particulates which are identified as pollutants. Most of the above mentioned applications revolve around droplet dynamics which makes it imperative to explore the fundamental aspects of droplet behavior. Moreover, to control these processes, there is a need to develop generalized correlations valid over a wide range of operating conditions which can predict the detailed behavior of such flows and the fluid dynamic phenomena they manifest.

As mentioned briefly in in the previous paragraph, one of the most important applications where droplet dynamics plays a vital role in practical systems of interest are liquid fueled propulsion devices. In combustion systems, in general, the evaporation of fuel and combustion is accelerated if the droplet size is smaller, which makes any process leading to a reduction in drop size of prime importance in combustor design. To accomplish this task, liquid fuel is atomized via several processes. One such process which is often used in a wide variety of applications including fuel injectors is called air-blast atomization. This atomization process works on the principle of transfer of kinetic energy from a coaxial high speed gaseous jet to the liquid jet at a

Figure 1.2. F-1 engine. Picture obtained from `http://www.nasa.gov/centers/marshall/images/content/118676main_F-1Engine_955x1360.jpg` on 8/26/2013.

high momentum flux ratio. This transfer of energy destabilizes the liquid jet thereby breaking it into ligaments and droplets. Figure 1.1 shows snapshots of a water jet destabilized by a coaxial air stream. An example where air blast atomization process is used, is a liquid rocket engine, where liquid oxygen (LOX) is atomized by a high speed coaxial hydrogen gas jet.

Another common atomization technique used in rocket engines is atomization via impinging jets. Figure 1.2 shows a picture of the F-1 rocket engine which was used in the Apollo program. Figures 1.3 and 1.4 shows examples of liquid sheets formed by two jets impinging on each other. In general, for a propulsion system employing impinging jets for spray atomization, the breakup process takes place in two steps, primary and secondary. This process is schematically shown in Figure 1.5. Primary atomization takes place as the fuel and oxidizer jets leave the injectors and impinge

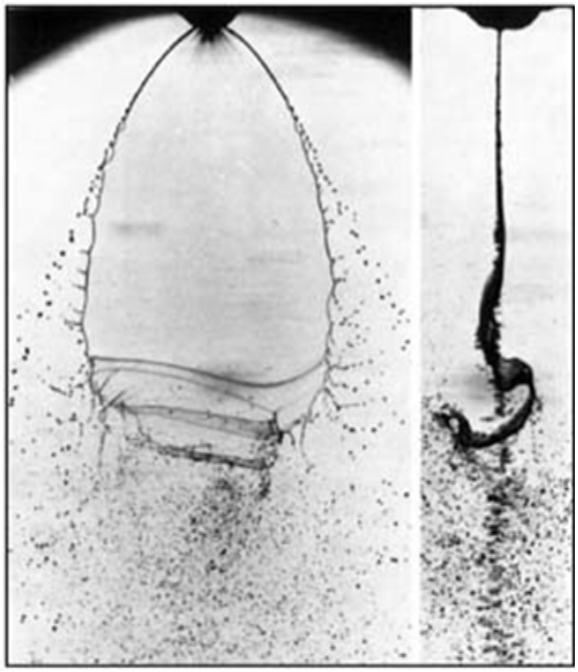

Figure 1.3. A liquid sheet from a fan spray nozzle (Villermaux, 2007). Reproduced with permission. ©Annual Reviews.

on each other under the action of aerodynamic, viscous, inertial, and tensile forces. The dynamic head of the injected propellant destabilizes the liquid streams, creating a liquid sheet, which disintegrates into ligaments and droplets (Taylor, 1960; Dombrowski & Hooper, 1964; Hasson & Peck, 1964; Huang, 1970; Ibrahim & Przekwas, 1991; Yang & Anderson, 1995; Lin, 2003; Bremond & Villermaux, 2006; Li & Ashgriz, 2006; Jung *et al.*, 2010). The shape and size of the ligaments and droplets produced during primary atomization depend on the flow and ambient conditions, as well as the injector geometry. These fluid structures further disintegrate to form finer droplets. This process is also called secondary atomization in the literature and is the focus of the current thesis. The final droplet size distribution is governed by how the products of primary atomization disintegrate. This makes the study of single droplet breakup immensely important. The significance of single droplet fragmentation is also bolstered by the recent work by Villermaux & Bossa (2009). There are

several parameters which can influence droplet dynamics including physical properties such as surface tension (for the liquid phase), viscosity & thermal conductivity of the two phases, relative velocity between the liquid and the gas and the ambient pressure and temperature conditions. To make matters even more complicated, the presence of turbulence, vaporization and combustion, in addition to the deforming and breaking liquid droplet widens the range of length and time scales considerably, making the whole process almost intractable, specially at higher flow rates. Even after decades of research, the fundamental physics underlying droplet breakup (even in a non-evaporating environment) is still elusive, not to mention the formulation and development of physics based generalized correlations to predict droplet dynamics and the final droplet size distribution. This thesis is an attempt to address some of these outstanding issues.

The next few sections describes the various experimental and numerical approaches which have been used in the literature to decipher the droplet breakup phenomena. An account of the contributions made to breakup physics using those approaches will be given in subsequent chapters as a preface to the results obtained during the current research work.

1.2 Experimental Methods

Extensive experimental investigations have been conducted to study droplet breakup and dynamics. Most of the experimental setups can be classified into three major groups - liquid drop exposed to an air stream from a nozzle, flow behind a shock wave in a shock tube and drop tower experiments. In each of these experiments the liquid droplet(s) was subjected to external forcing by the surrounding gas (air in most cases). In the following sections, a brief description of the various experiments is presented.

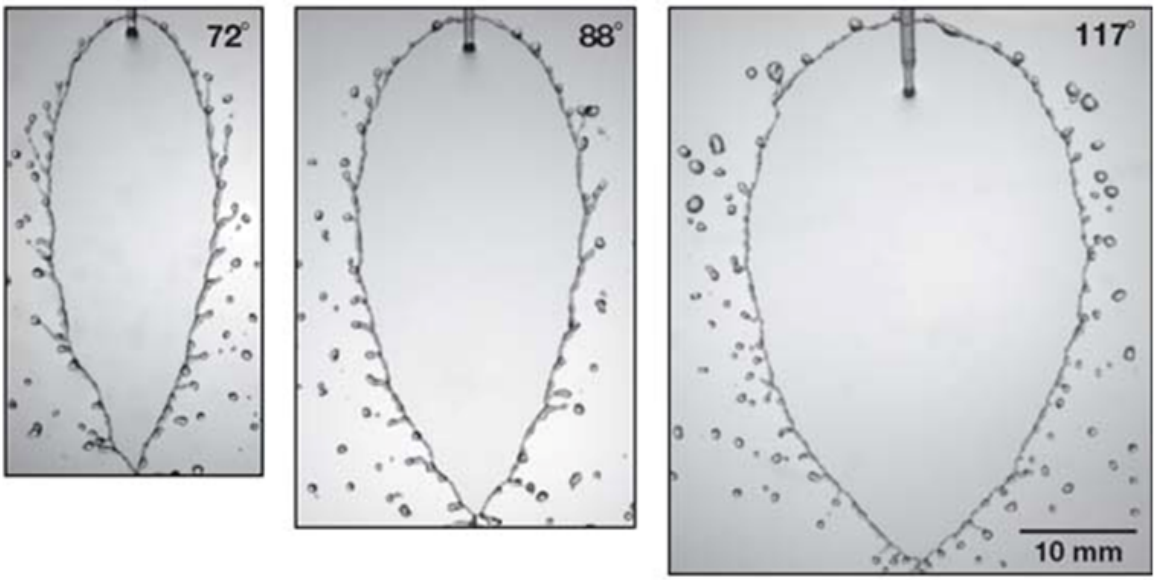

Figure 1.4. Water sheet fragmentation for three collision angles. The jet velocity is equal to 4 m/s and the jet diameter is 1.05 mm. Elongation of ligaments is clearly enhanced when the collision angle is decreased (Villermaux, 2007). Reproduced with permission. ©Annual Reviews.

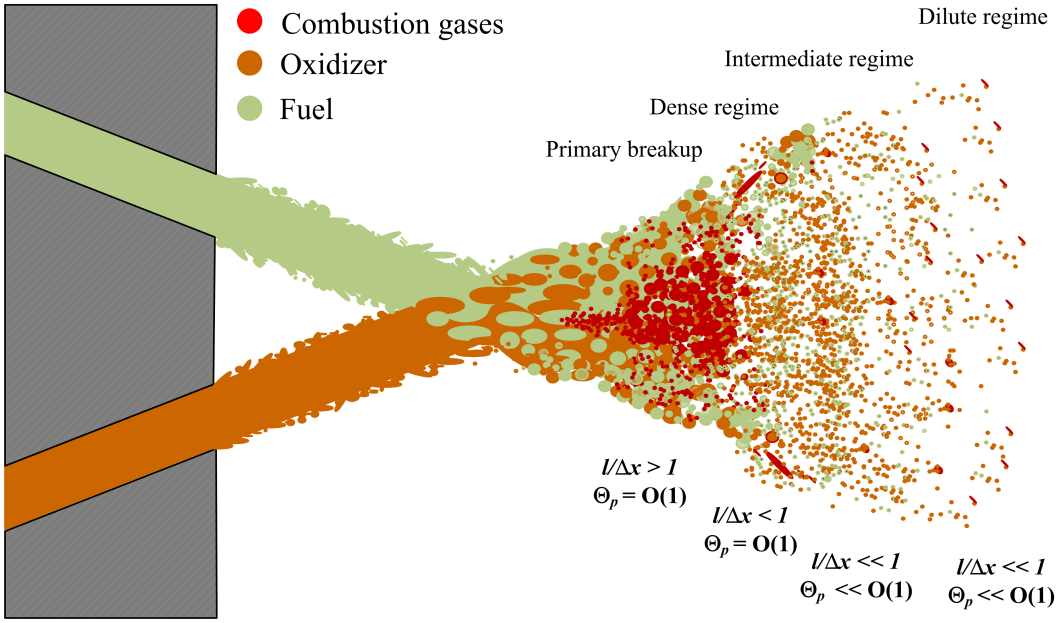

Figure 1.5. Schematic of impinging jets and droplet dynamics.

1.2.1 Shock Tube Experiments

Shock tube experiments have been used to study single droplet deformation and fragmentation for over five decades. In this section, a typical shock tube experimental arrangement is described as was used by Dabora (1966). The basic philosophy is simple, a shock wave travels over a droplet which is falling into the driven section of a shocktube. The passing shock wave creates a uniform flow which causes deformation and breakup of the droplet. Droplet morphology is recorded using shadowgraphy and a high speed camera installed in the shocktube viewing window. The testing time varies from 2 ms to 200 μs corresponding to a shock Mach numbers of 1.5 and 5 respectively. The time lapse between the passage of the shock front and the arrival of the reflected shock wave is defined as the testing time. To determine the testing time a thin film heat transfer gauge and a pressure gauge is flush mounted on the test section walls. The interface is indicated by the change in slope of the heat transfer trace. The sensitivity of the heat transfer and pressure gauges is typically about 2 mv/cm and 50 psi/cm respectively.

The driven section of the shocktube is generally open to atmosphere, therefore the pressure ratio and the shock strength is entirely controlled by the pressure generated in the driver. Gases such as He, H_2 and N_2 are usually used as the carrier fluid in experiments exploring single droplet dynamics. Steel diaphragms are placed between the flanges of the driven and driver sections and are designed to rupture at a certain pressure depending on the design conditions of shocktube. An example of the photographs obtained using this experimental configuration is shown in Figure 1.6. This experimental setup and its variants have been used extensively by researchers to study single droplet breakup and dynamics (Ranger & Nicholls, 1968; Krauss & Leadon, 1971; Gel'fand *et al.*, 1974; Boiko *et al.*, 1987; Hsiang & Faeth, 1992, 1993; Faeth *et al.*, 1995; Hsiang & Faeth, 1995; Chou *et al.*, 1997; Chou & Faeth, 1998; Joseph *et al.*, 1999; Dai & Faeth, 2001). Contribution of these experiments to the

droplet physics literature will be presented in Chapter 4.

1.2.2 Droplet in an Air Jet

This is one of the other popular experimental configurations used to study the dynamics of liquid droplets. In this setup a droplet (or a series of droplets) is subjected to an air flow either from a wind tunnel or from a compressed air tank. The contents of this section are primarily based on the work of Arcoumanis *et al.* (1994, 1996) and Krzeczkowski (1980) but similar experimental apparatus have been used by other researchers in the past as well (Joseph *et al.*, 1999; Lopez-Rivera & Sojka, 2009; Lopez-Rivera, 2010; Theofanous *et al.*, 2004), to study droplet breakup and dynamics. Schematic of the setup is shown in Figure 1.7 (Arcoumanis *et al.*, 1994). Liquid droplets are injected into a near uniform flow exiting a nozzle. The breakup characteristics are recorded using high speed photography. The camera is positioned in a direction perpendicular to the direction of the air jet to focus on the initial stages of droplet breakup. The backdrop is illuminated using a CU10 laser, focused on to an optical fiber which transports it to the camera through a semi transparent screen to diffuse the light. A He-Ne laser beam is used to achieve synchronisation of the camera with the falling droplet as shown in the schematic figure. An example of the photographs obtained using this experimental configuration is shown in Figure 1.8.

1.2.3 Instrumentation

Droplet deformation and breakup involves a wide range of length and time scales. In order to capture the small deformations on the droplet surface and elsewhere, several techniques have been used in the literature. Among them, single- and double-pulsed shadowgraphy and holography have been extensively used to observe the properties of the parent drop and size and velocity distributions of the child droplets. The working principles of these two techniques are described in brief in this section. Most common droplet delivery method, the vibrating capillary tube drop generator, is also

Figure 1.6. An example of the photographic sequence of liquid droplet breakup obtained using a shocktube experimental facility (Dabora, 1966).

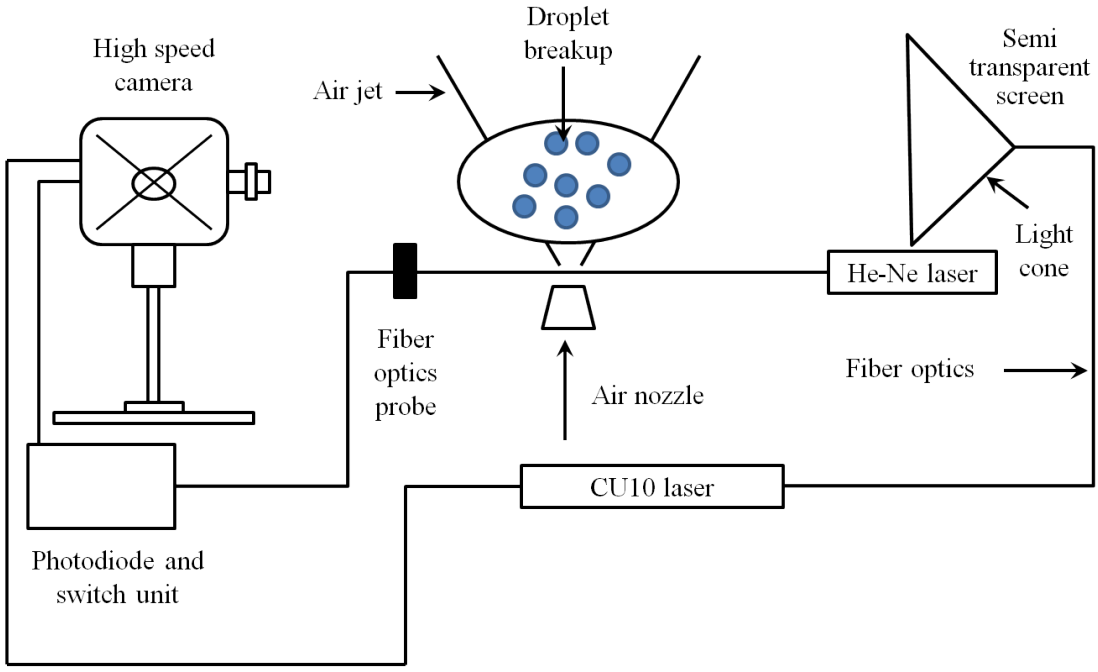

Figure 1.7. Schematic of the experimental setup to study breakup of liquid droplets exposed to an air jet (Arcoumanis *et al.*, 1994).

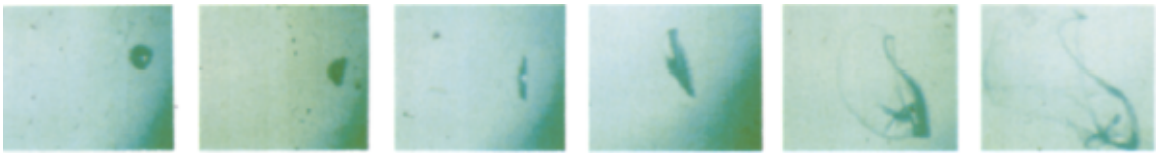

Figure 1.8. An example of the photographic sequence of liquid droplet breakup obtained by exposing a water droplet to an incoming air stream at $We = 21$ (Arcoumanis *et al.*, 1994).

discussed at the end of the section. There are several other techniques which have been used for visualization and measurement, the details of which can be referred to in the literature.

In droplet dynamics literature, in general, holographic techniques are used to examine the outcome of droplet breakup, while shadowgraphs and images from high-speed photography are used to observe the overall dynamics. To improve the image contrast, the illumination source is often pulsed and hence called pulsed- shadowgraphy and holography. Before describing double (pulsed) holography, it is useful to understand the basic principles of holography and perhaps the difference between photography and holography. When an object is illuminated, light is scattered and an "object wave" is created, which contains the optical information of the object. The brightness of the object is encoded in the amplitude of the light wave, while the phase stores the shape of the object. During photography this object wave darkens the photographic film but only the light intensity is recorded and the phase information in the plane of the screen is lost. Therefore the object wave can never be completely restored and the result is a 2D image. On the other hand, it is possible to reconstruct the object wave completely using holography which uses interference and diffraction properties of light. The basic principle is simple- the object as well as the film are illuminated with the same laser. The object wave generated from the object and the reference wave interfere, producing a fringe pattern in the holographic layer. The optical information of the object is stored in the form of brightness modulations of the fringes and the distance between the fringes. When the hologram is illuminated with a light resembling the reference wave (called the reconstruction wave), it is diffracted by the interference pattern of the hologram and the original object wave is constructed. Thus, it looks like a 3D image of the object to an observer looking at the hologram.

The advantage of holographic interferometry or double holography is that small

deformations (< 1 μm) of diffused reflecting objects can be measured. In double exposure holography, two holographic recordings of the same object are stored on one photographic layer. The first one is that of an undisturbed object and the other of a slightly deformed object. While reconstruction, both object waves are illuminated and they interfere with each other creating visible interference fringes encompassing the whole object. The density of the fringes then represents the deformation distribution. For deformations more than 100 μm, the fringes are very closely spaced making data interpretation very difficult. Ideally, if using a He-Ne laser, the lower threshold of identifiable deformation is well below 0.1 μm but the lowest resolvable object size can differ in practice. For example, in experiments conducted by Chou & Faeth (1998), which employed pulsed holography to study droplet breakup phenomena in bag breakup regime, allowed objects as small as 3 μm to be observed and as small as 5 μm to be measured with 5% accuracy. The book by Ackermann & Eichler (2007) is an excellent reference for further reading on holography and its use in various scientific applications.

As mentioned before, pulsed shadowgraphy is often used to capture the overall dynamics of the droplet breakup process. It has been extensively used as a visualization tool in fluid dynamics and heat transfer experiments. To start with, it should be clearly noted that a shadowgraph is a shadow of an object and not its optical image. A basic shadowgraphy setup consists of an expanded and collimated laser beam, the object and a reasonably flat reflective screen (and perhaps a camera and a computer to process the images/videos). Without the object in the field of view, the screen is illuminated uniformly. When the object is present, the light is deflected, refracted and bent from its original path because of optical inhomogeneities, casting a shadow on the screen. The gradient of the deflection angle or equivalently the Laplacian of the refractive index is responsible for producing the shadowgraph. The inherent simplicity of shadowgraphy is by far its major advantage, while its essential ambiguity

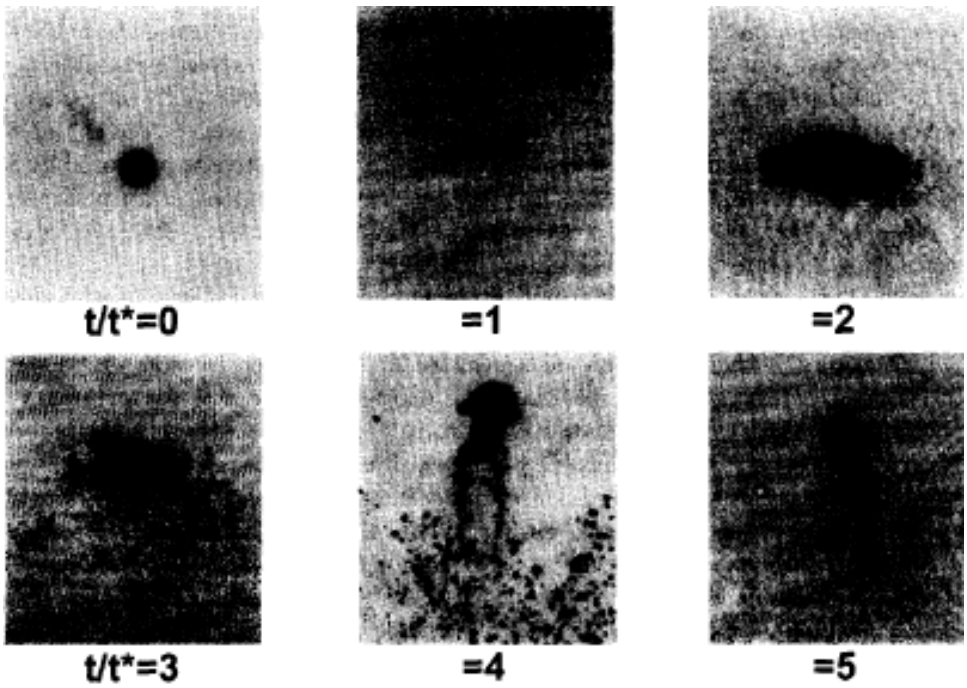

Figure 1.9. Shadowgraph of shear breakup of a 590 μm water droplet in a shocktube experiment. Operating conditions: $We = 250$ and $Oh = 0.0044$ (Chou *et al.*, 1997).

- being a shadow rather than an image, is the cause of most of its limitations. If the screen is at a large distance from the object, light rays can undergo transformation forming "caustics", which is its major drawback. An example of shadowgraph obtained during a droplet breakup experiment is shown in Figure 1.9 (Chou *et al.*, 1997).

In most of the experiments on droplet breakup, single stream of liquid droplets are produced using vibrating capillary devices. Rayleigh's analysis of capillary jet instability is the basic working principle of these devices. According to Rayleigh (1878), the wavelength for maximum instability for a jet with diameter, d_j is given by:

$$\begin{gathered} \lambda_j = 4.058 d_j \\ \text{or equivalently, } f_j = u_j / 4.058 d_j \end{gathered} \tag{1.1}$$

When a liquid is forced through a capillary tube at relatively low pressures, a drop is formed at the end which increases in size until the surface tension force can no

longer balance the force of gravity and the droplet falls. As the head is increased, at a critical pressure, a jet is formed with a diameter equal to the capillary tube exit diameter. If this liquid jet is subjected to forced oscillations with a frequency given by Equation 1.1, uniform liquid droplets are produced. This concept is the underlying principle in the development of various drop generators for the production of monosized liquid droplets. One such drop generator was developed by Dabora (1967), the variants of which have been extensively used in experiments conducted to study droplet breakup phenomena (Dabora, 1966; Ranger & Nicholls, 1968; Hsiang & Faeth, 1992, 1993; Faeth *et al.*, 1995; Hsiang & Faeth, 1995; Chou *et al.*, 1997; Chou & Faeth, 1998; Dai & Faeth, 2001). An electrostatic drop selection system, originally developed by Sangiovanni & Kesten (1977), is often installed with the vibrating capillary setup to ensure sufficient spacing between the droplets, hence minimizing drop-drop interaction.

1.3 Numerical Approaches

Rapid advances in computing technology (both hardware and software) over the last couple of decades, have led to the development and use of sophisticated numerical tools to understand the behavior of complex multiphase flow phenomena. Even though experiments have been conducted to elucidate multiphase flow physics for a long period of time, the complicated flow physics underlying such fluid dynamics phenomena is still elusive. This is primarily due to the wide range of scales involved in the problem, which makes it difficult to take measurements, especially inside the liquid phase, for example in droplet dynamics studies. In the light of phenomenal growth in computing power, numerical approaches, especially direct numeral simulations (DNS), have proven to be a viable alternative to resolve these issues. One of the criteria to classify numerical methods used in multiphase flow literature is based on the treatment of interface/boundary between the various phases. This is perhaps

the single most important feature which separates numerical strategies used to study single phase from multiphase flows. Based on this, various numerical approaches can be divided into two broad classes, namely, interface tracking and interface capturing techniques. The next two sub-sections give a brief overview of these two methodologies. We have used interface capturing, VOF methodology in this research initiative, the details of which are presented in Chapters 2 and 3.

1.3.1 Interface Tracking

Interface or front tracking methods, requires a moving mesh to "track" the interface as the flow evolves. These methods provide the interface location and curvature with high accuracy but suffer when there are large deformations and topology changes. Examples of such flow dynamic phenomena include breakup and coalescence among others. In such flow conditions, if mesh topology is not modified by reconnecting the sharp interfaces, front tracking methodologies have a tendency to break down because of the presence of singularities in the primitive variables (Cristini & Tan, 2004). Front/interface tracking techniques include immersed boundary (IB) methods (Mittal & Iaccarino, 2005; Peskin, 1982, 2002), boundary-integral methods (Zinchenko *et al.*, 1997, 1999; Pozrikidis, 1992), finite-element methods (Wilkes *et al.*, 1999), and marker and cell methods (Harlow & Welch, 1965). Usually in front tracking algorithms, the interface is represented by a discrete set of Lagrangian markers. The interface is then advected by the local flow velocity, thus tracking the boundary between the different fluids.

1.3.2 Interface Capturing

Interface capturing techniques are suited for simulating multiphase phenomena involving extreme deformation and topology change because the interface evolves through the mesh. Level-set, volume of fluid (VOF), phase-field and lattice Boltzmann methodologies fall in this category. To take advantage of the merits of level-set and VOF

methods, hybrid level-set-VOF methods have also been developed recently (Sussman & Puckett, 2000) and are also classified under interface capturing techniques. In interface capturing techniques, the interface evolves through the computing mesh, generally modeled as a scalar variable. The fluid properties, such as viscosity, density and thermal conductivity are smooth while the surface tension force is treated as a volume force in a thin region around the interface. We shall discuss level-set and VOF methods which are the two most popular interface capturing methods used in the literature to simulate droplet breakup phenomena, in the following subsections. Details of phase-field and lattice Boltzmann techniques used in multiphase flow research can be obtained from the reviews of Chen (2002), Chen & Doolen (1998) and Aidun & Clausen (2010) respectively.

1.3.2.1 Level-Set Method

Level-set methods take the "analysis view" for the representation and tracking of moving interfaces (Sethian & Smereka, 2003). In level-set techniques a scalar variable $\phi : R^2 \times [0, \infty) \rightarrow R$ is defined such that $\phi = 0$ represents the interface $\Gamma(t)$ at any given time. The equation for the evolution of ϕ corresponding to the interface motion is given by:

$$\phi_t + \mathbf{u}.\nabla\phi = 0 \tag{1.2}$$

ϕ is a signed function whose sign distinguishes the two phases. Advantage of level-set methods include, (a) ability to compute geometric quantities, such as normal vectors and curvature easily by the use of derivative operators applied to the level-set function, and, (b) the level-set equation 1.2 is unchanged in higher dimensions and provides an easy way to extend the algorithm from a lower to a higher dimension. One considerable disadvantage of level-set methods is its poor mass conservation property. The level-set advection equation has a tendency to accumulate errors, therefore in order to maintain a proper thickness of the interface, the level-set function has to be

reinitialized periodically. Conversely, this reinitialization, as pointed by Sethian & Smereka (2003), is a significant source of error in the front position, and should be avoided.

1.3.2.2 Volume of Fluid Method

The volume of fluid method is based on the "set theoretic view" where the characteristic function $\psi(\mathbf{x}, t)$ is 1 inside the interface and 0 elsewhere. Similar to level-set function, the advection equation can be written as:

$$\psi_t + \mathbf{u}.\nabla\psi = 0 \tag{1.3}$$

Volume of fluid method proceeds in two steps:

(a) Interface reconstruction using the stored volume fraction data in each computation cell. This is generally accomplished using piecewise linear interface construction technique.

(b) Propagation is the second step after interface reconstruction in volume of fluid methodology. The motion of the interface by the fluid, once it has been reconstructed is modeled using a suitable algorithm.

In the current research, we have adopted VOF methodology, the details of which are described in Chapter 3. VOF methods have an excellent mass conserving property because the advection algorithm is based on discrete representation of Equation 1.3 (Scardovelli & Zaleski, 1999). That being said, since the interface information is not directly stored, care has to be taken during interface propagation and flux calculations to ensure consistency and avoid non-physical solutions. One of the other drawbacks of VOF methods is the complexity in the reconstruction step where interface normal and curvature calculations can introduce errors. Topology changes during extreme deformation or breakup events are implicit in the formulation and thus the method is suited for the study of droplet breakup physics. In addition, since volume fraction

values of only the neighboring cells are needed to update the the volume fraction in a given computational cell, it is relatively easy to implement VOF method in parallel.

1.4 Research Objectives

This thesis is an attempt to address several unanswered questions currently confronting the spray community. Unanswered questions include identification and prediction of breakup modes at varying operating conditions, quantitative description of fundamental processes underlying droplet breakup and generalized correlations for child droplet size distributions and drag coefficient associated with the deformation and fragmentation process. As mentioned in Section 1.1, current understanding of droplet breakup phenomena is still primitive and is based on visual interpretation of experimental images, such as shown in Figures 1.6 and 1.9, which do not reveal much qualitative information, let alone quantitative description of the phenomena. The present work is aimed at answering the above questions by investigating the detailed flowfield and structure dynamics of liquid droplet breakup process and extracting essential *quantitative* physics governing this complex multiphase phenomena. High-fidelity direct numerical simulations are conducted using a volume-of-fluid (VOF) interface capturing methodology. To isolate the hydrodynamic mechanisms dictating droplet breakup phenomena, evaporation and compressibility are neglected, and simulations are performed for incompressible fluids at isothermal (298 K) conditions. The specific objectives are summarized below:

1. Newtonian fluids

    (a) Quantitative understanding of different breakup modes

    (b) Development of generalized regime diagram for a broad range of operating pressure conditions to predict the droplet breakup mechanism

    (c) Develop correlations to predict child droplet size distributions

(d) Determination of drag coefficient of deforming and fragmenting liquid droplets and development of correlations to predict droplet drag for a wide range of Weber numbers

2. Non-Newtonian fluids

   (a) Identify the underlying physics behind droplet breakup of liquids exhibiting shear-thinning, power-law behavior

   (b) Preliminary study of droplet size distributions

1.5 Thesis Organization

The thesis is organized in seven chapters. Chapter §1 (present chapter) gives a broad overview of multiphase flow research leading to the motivation. Details of various experimental and numerical techniques used to study droplet breakup dynamics are then described followed by the specific research objectives of the current research. Theoretical and mathematical formulation of this multiphase flow dynamics problem is described in Chapter §2. Governing equations, boundary conditions and non-dimensional numbers are detailed in this chapter. The most important physical property of interest during droplet breakup phenomena - surface tension, its dependence on pressure, temperature and surrounding fluids and measurement technique, is also discussed in detail.

Numerical methods including time integration schemes, spatial discretization of advection, viscous and surface tension terms are described in the next chapter. Details of volume of fluid advection scheme, time step constraints and adaptive mesh refinement are followed by validation and verification studies in Chapter §3. Results are divided under three headings: Newtonian droplet breakup physics, drag coefficient of deforming and fragmenting Newtonian droplets, and non-Newtonian droplet breakup and dynamics. Chapter §4 examines the details of oscillatory, bag, multimode and

shear breakup mechanisms. Generalized regime diagram and correlations for child droplet size distributions are developed next. The next chapter presents results concerning the drag coefficient of deforming and fragmenting liquid droplets, along with the development of correlation to predict coefficient of drag at a wide range of Weber numbers. Chapter §6 explores the breakup of shear-thinning non-Newtonian liquid droplets. A preliminary study on droplet size distributions obtained for power-law liquids is also included in this chapter. The thesis ends with a summary of conclusions and recommendations of future work in Chapter §7.

CHAPTER II

THEORETICAL FORMULATION

The theoretical and mathematical formulation of this multi-phase, multi-fluid problem is based on a complete set of incompressible Navier-Stokes equations with surface tension. Conservation equations for mass and momentum are solved with an interface capturing, volume of fluid methodology. The basic assumptions made during the current study are described in brief. The governing equations are then presented along with appropriate boundary conditions. Spatial discretization and adaptive mesh refinement (AMR) methodology used in this research is described in detail. The important non-dimensional parameters along with the physical fluid properties governing the physics under consideration are also discussed in the last section of the chapter.

2.1 Governing Equations and Boundary Conditions

The governing equations are based on three basic assumptions: the continuum hypothesis, the hypothesis of sharp interfaces and fluid incompressibility. To shed light on the validity of the continuum assumption for the current problem, lets consider the measurement of density inside a box. When the box is small, the density fluctuates. It becomes smoother as the box dimension increases and can be approximated by a continuous function, ρ (Batchelor, 2000). For liquids at NTP, this happens for length scales of the order of $10^{-9}m$ (Tryggvason, 2011). For gases, the important length scale dictating the validity of the continuum hypothesis is the mean free path, λ, the average distance that a molecule travels between successive collisions. If the length scale under investigation, $l >> \lambda$, the gas obeys Navier-Stokes equations to a very good approximation. For the current problem in hand the length scales under

consideration are much larger than the mean free path and continuum hypothesis, thus seems to an excellent assumption for studying the droplet breakup phenomena.

One of the other assumptions made during the current study, is the postulate of sharp interfaces. Interface is the boundary between different fluids. Fluid properties, such as viscosity, thermal conductivity, density and state generally changes across the interface. According to the sharp interface hypothesis, it can be assumed that the interface has a vanishing thickness and the transition from one phase to another takes place at very small scales (Tryggvason, 2011). The most important intermolecular force influencing the droplet breakup physics, capillarity, has been modeled using surface tension. Surface tension is assumed to be concentrated on the sharp interface. A detailed description of surface tension will be given in the last section of this chapter.

The main objective of the thesis is to understand the physics and dynamics associated with droplet breakup phenomena. The liquid can easily be treated as incompressible for obvious reasons. Owing to the operating conditions ($M << 1$) considered in the current research, the last major assumption made in this thesis is that of fluid incompressibility.

Conservation of mass can be written as:

$$\frac{\partial \rho}{\partial t} + \nabla.(\rho \mathbf{u}) = 0 \tag{2.1}$$

where $\mathbf{u}$ is the velocity vector and $\rho = \rho(\overrightarrow{x}, t)$ is the density. By definition, $\nabla.(\rho \mathbf{u}) = \mathbf{u}.\nabla\rho + \rho\nabla.\mathbf{u}$. For incompressible flows the velocity field is divergence free and equation 2.1 translates to evolution equation of density as:

$$\frac{\partial \rho}{\partial t} + \mathbf{u}.\nabla\rho = 0 \tag{2.2}$$

and mass conservation equation transforms to:

$$\nabla.\mathbf{u} = 0 \tag{2.3}$$

At this point, it is useful to note that there is no requirement for the density to be same everywhere for incompressible flows. To elucidate this more clearly, lets consider

the Lagrangian description of fluid flow. For incompressible flows, the density of a fluid packet can vary from one packet to another but it should remain constant for a particular packet. Since the fluid packets are distributed spatially and the distribution can change with time because of advection of fluid packets, the density distribution changes both, spatially and temporally, and can be evaluated using equation 2.2. An excellent description of incompressibility and solenoidal nature of the velocity distribution in incompressible flows is given in Batchelor (2000).

The momentum conservation is given by:

$$\frac{\partial \rho \mathbf{u}}{\partial t} + \nabla . (\rho \mathbf{u}\mathbf{u}) = -\nabla p + \nabla . \widetilde{\tau} + \mathbf{F_{st}} \tag{2.4}$$

where $\mathbf{F_{st}}$ is the surface tension force per unit volume and $\widetilde{\tau}$ is the shear stress tensor given by:

$$\widetilde{\tau} = \mu \left(\nabla \mathbf{u} + (\nabla \mathbf{u})^T \right) \tag{2.5}$$

where $\mu = \mu(\overrightarrow{x}, t)$ is the dynamic viscosity. μ is constant for Newtonian fluids but can vary with shear strain for non-Newtonian fluids. We shall look at both the fluids while discussing the droplet breakup phenomena. The governing equations are written in an Eulerian reference frame and we are interested in capturing the fluid interface. A volume of fluid scalar variable, f, is introduced to trace the multi-fluid interface. It is defined as the volume fraction of a given fluid in each computational cell. f is defined as follows:

$$f = \begin{cases} 0 & fluid\ 1 \\ \\ 1 & fluid\ 2 \end{cases} \tag{2.6}$$

The density and viscosity in each computational cell is defined as a linear function of the volume fraction variable, f and are given by:

$$\rho = f\rho_1 + (1 - f)\rho_2 \tag{2.7}$$

$$\mu = f\mu_1 + (1 - f)\mu_2 \tag{2.8}$$

The advection equation for the density can then be replaced with an equivalent advection equation for the volume fraction

$$\frac{\partial f}{\partial t} + (\mathbf{u}.\nabla)\, f = 0 \tag{2.9}$$

The mathematical formulation described above is often referred to as "one-fluid" or "whole-domain" approach in the literature. The governing equations are written for the all the different phases without using the jump condition at the interface. The jump condition at the fluid interface translates to singularities in the governing equations. It can easily be shown that this formulation is equivalent to that written for each phase separately with the pressure jump condition at the interface. As pointed out by Tryggvason (2011), the one-fluid approach can be interpreted in two ways, in a weak sense where the governing equations are satisfied only in the integral form or by admitting solutions using step and delta functions. In the current research, we have resorted to the latter approach by modeling the surface tension effects using a delta function (refer Equation 2.10). Surface tension effects on the fluid motion have been modeled using the continuum surface force (CSF) model developed by Brackbill *et al.* (1992).

$$\mathbf{F_{st}}(\overrightarrow{x_1}) = \sigma \int_S \kappa(\overrightarrow{x_2})\widehat{n}(\overrightarrow{x_2})\delta(\overrightarrow{x_1} - \overrightarrow{x_2})dS \tag{2.10}$$

where σ is the surface tension force, κ the local curvature and δ the Dirac delta function. The curvature is evaluated by:

$$\kappa = \frac{1}{R_1} + \frac{1}{R_2} \tag{2.11}$$

where R_1 and R_2 are the principal radii of curvature of the interface. The surface tension force in each computational cell at the interface is approximated by:

$$\mathbf{F_{st}} = \sigma\kappa\delta\widehat{n} \tag{2.12}$$

Lets consider the governing equations in the pressure jump condition form. Equation 2.4 can be written for each phase as:

$$\frac{\partial \rho \mathbf{u}}{\partial t} + \nabla.(\rho \mathbf{u}\mathbf{u}) = -\nabla p + \nabla.\widetilde{\tau} \tag{2.13}$$

Jump condition exists in the neighborhood of the singular surface S. The stress conditions are given by:

$$[-pI + \widetilde{\tau}]_S.\widehat{n} = \sigma\kappa\widehat{n} + \nabla_S\sigma \tag{2.14}$$

where I is the identity tensor, ∇_S is the surface gradient operator and $[.]_S$ represents the jump of a quantity across the surface S. If surface tension is assumed to be constant, $(\nabla_S\sigma = 0)$, the shear stress condition becomes:

$$[\widehat{t}.\widetilde{\tau}.\widehat{n}]_S = 0 \tag{2.15}$$

The normal stress condition is:

$$[-p + \widehat{n}.\widetilde{\tau}.\widehat{n}]_S = \sigma\kappa \tag{2.16}$$

Equation 2.16 reduces to Laplace's equation, which defines the pressure jump across the two interfaces because of surface tension, and is given by:

$$\triangle p_s = \sigma\kappa \tag{2.17}$$

In incompressible flows, pressure is not a thermodynamic property and is solely a function of the velocity field. To have a closer look at pressure, lets take the divergence of Equation 2.4. If the velocity field is solenoidal, this yields the following:

$$\nabla^2 p = -\rho\frac{\partial^2(u_i u_j)}{\partial x_i \partial x_j} \tag{2.18}$$

In fact, the satisfaction of this Poisson equation is necessary to enforce incompressibility and solenoidal nature of the velocity field. Since the density, ρ, viscosity, μ and surface tension, σ are not functions of temperature (all the numerical experiments being conducted at constant temperature conditions) during the current study, the

continuity and momentum equations are decoupled from the energy equation and it is not necessary to solve the energy equation to obtain the velocity and pressure fields.

The governing equation described above are subject to certain boundary conditions, namely, the no slip, no penetration and interface pressure jump condition. Lets define $\widehat{t}$ and $\widehat{n}$ as a family of tangent and normal vectors, then the no slip and no penetration conditions are given by:

$$\mathbf{u}.\widehat{t}_{\perp} = 0 \tag{2.19}$$

$$\mathbf{u}.\widehat{n}_{\perp} = 0 \tag{2.20}$$

Zero pressure gradient condition is imposed on across the liquid/gas interface and is given by:

$$\nabla p.\widehat{n}_{\perp} = 0 \tag{2.21}$$

2.2 Non-dimensional Numbers

Non-dimensional numbers are useful to characterize dynamically similar flows. Non-dimensionalizing the Navier-Stokes equations described in the previous section for incompressible fluids with surface tension yields:

$$\nabla^*.\mathbf{u}^* = 0 \tag{2.22}$$

$$\frac{\partial \mathbf{u}^*}{\partial t^*} + \nabla^*.(\mathbf{u}^*\mathbf{u}^*) = -\nabla^* p^* + \frac{1}{\mathbf{Re}}\nabla^*.\widetilde{\tau}^* + \mathbf{F}^*_{\mathbf{st}} \tag{2.23}$$

$$\frac{\partial f}{\partial t^*} + (\mathbf{u}^*.\nabla^*)\, f = 0 \tag{2.24}$$

$$\mathbf{F}^*_{\mathbf{st}}(\overrightarrow{x}^*) = \frac{\mathbf{1}}{\mathbf{We}} \int\limits_{\mathbf{S}^*} \kappa^*(\overrightarrow{y}^*)\widehat{\mathbf{n}}(\overrightarrow{y}^*)\delta^*(\overrightarrow{x}^* - \overrightarrow{y}^*)\mathbf{dS}^* \tag{2.25}$$

Examination of the above non-dimensionalized equations reveal the dominant effects influencing various multiphase phenomena. Various non-dimensional parameters dictating the droplet deformation and breakup phenomena are summarized in Table

Table 2.1. Relevant non-dimensional parameters for Newtonian liquid droplet breakup process.

Non dimensional number	Definition
Weber number, We	$\rho_g U^2 D/\sigma$
Ohnesorge number, Oh	$\mu_l/\sqrt{\rho_l D\sigma}$
Reynolds number, Re	$\rho_g U D/\mu_g$
Density ratio	ρ_l/ρ_g
Viscosity ratio	μ_l/μ_g
Mach number, M	U/a

2.1. Here, D is the diameter of the droplet; U, the relative velocity of the droplet with respect to the ambient; ρ_g and ρ_l, the density of the liquid and gaseous phases; μ_g and μ_l, the gas and liquid dynamic viscosities; a is the speed of sound and σ is the surface tension of the liquid phase. Weber (Weber, 1931) and Reynolds numbers are the ratio of inertial to surface tension and viscous forces, respectively. Ohnesorge number (Ohnesorge, 1936) on the other hand is the ratio of viscous to surface tension forces. To understand Oh number in a more physical manner, consider $Oh^2 = \mu_l^2/\rho_l D\sigma$. This quantity can be viewed as an inverse of a Reynolds number based on capillary velocity. Capillary velocity, $V_{cap} = \sigma/\mu_l$, is the velocity at which a viscous fluid thins and eventually breaks (McKinley, 2005).

2.3 Numerical Model and Spatial Discretization

The numerical model used in this thesis is based on Gerris flow solver (Popinet). In the following section the numerical model and spatial discretization employed in Gerris will be described in brief. The details of the various numerical schemes will

be discussed in Chapter 3. The governing equations described in section 2.1 are solved using a projection method based on variable density fractional step numerical methodology. The fractional step projection method computes an interim velocity field in the first step. This is followed by the computation of the pressure field by solving the Poisson equation and the projection of the interim velocity distribution onto a divergence free velocity field. A quad/octree spatial discretization is used in combination with a multilevel Poisson solver to solve for the pressure distribution. An example of the octree grid architecture and AMR used during the current research is shown in Figure 2.1. As clearly seen Cartesian grid system is used in the study. All the primitive variables- momentum components, pressure and volume fraction are collocated at the cell centers of the discretized volume. The numerical solution procedure employs finite-volume formulation and the cell centered values are volume averaged for the corresponding volume of the finite-volume. This collocated definition of primitive variables is useful for mesh adaptation, as well as, during the implementation of the Gudunov scheme for the non-linear convective terms. To treat the viscous terms accurately, an approximate projection method developed by Almgren *et al.* (2000) is used. The scalar VOF variable, f, is obtained by solving the advection equation for the volume fraction. A piecewise-linear geometrical VOF scheme (Scardovelli & Zaleski, 1999) generalized for quad/octree spatial discretization is used to solve equation 2.9. The value of the volume fraction in each cell then corresponds to the fraction of each cell filled with the reference phase. Computational cells completely filled with fluid 1 are characterized by $f = 0$ and fluid 2 by $f = 1$, and cells containing the interface are characterized by $0 < f < 1$. Since face-centered velocities are divergence-free, the function f is then advected using these velocities.

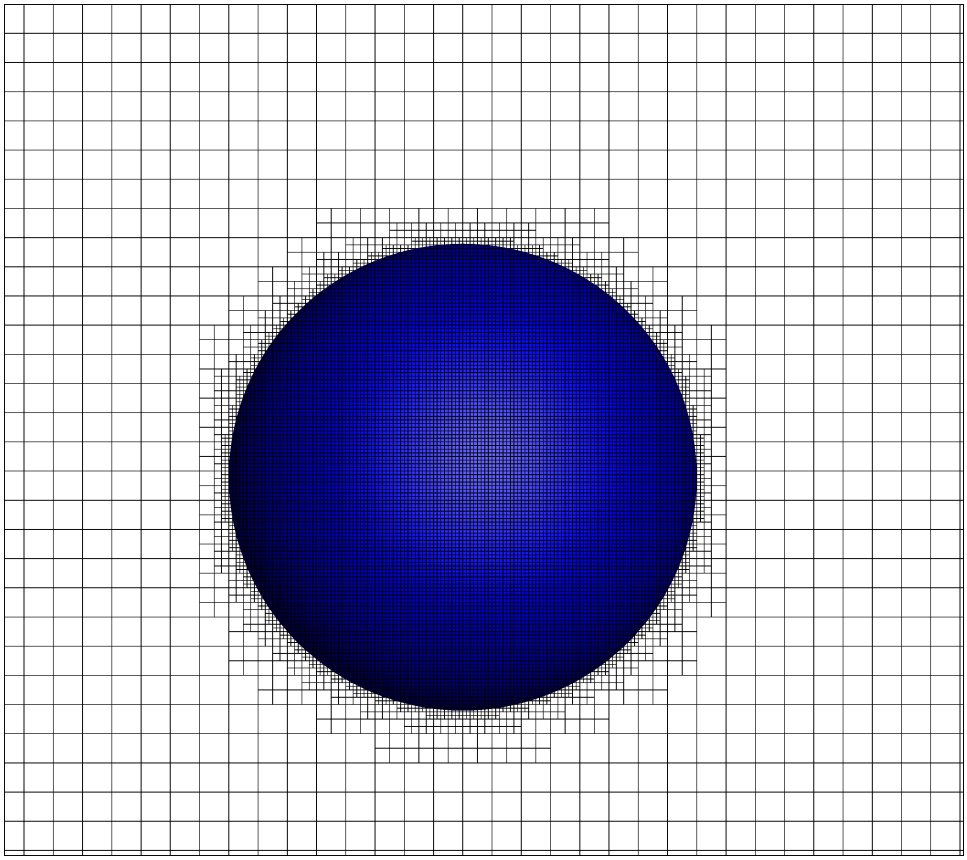

Figure 2.1. An example of adaptive mesh refinement used to study droplet breakup. The interface is resolved by adapting the grid near the droplet surface. The blue color represents the droplet.

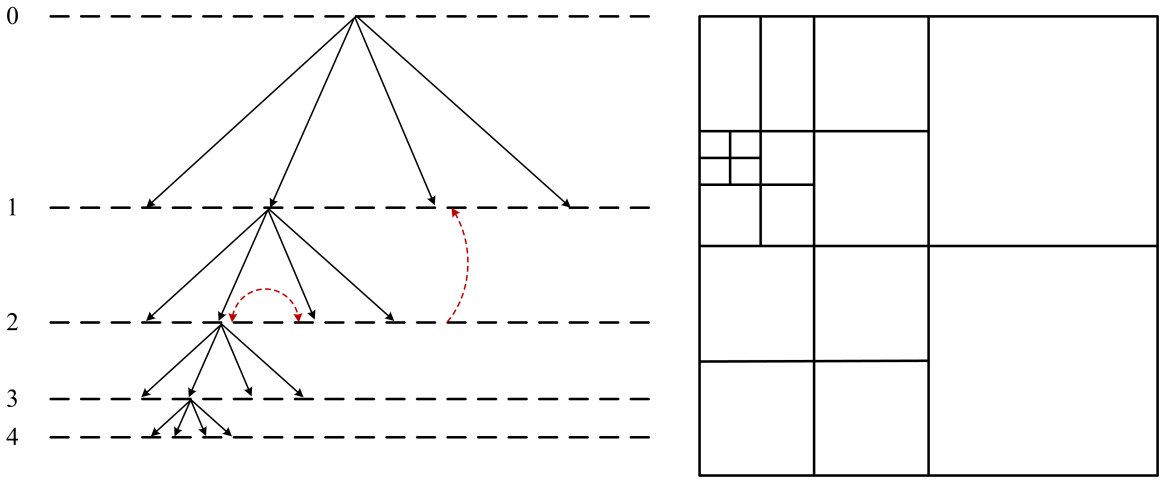

Figure 2.2. An example of quadtree discretization and corresponding hierarchy tree. The red colored dashed lines show the pointers to cells at the same level and to parent level cells.

2.3.1 Quad/Octree Data Structure and Adaptive Mesh Refinement

The domain is spatially discretized using cubic (square in 2D) computational cells organized as octree (quadtree in 2D) (Popinet, 2003; Samet, 1990). Researchers have used this type of discretization methodology in the past to study incompressible separated flows (Greaves & Borthwick, 1998), compressible flows, including shock propagation and shock-bubble interactions (Khokhlov, 1998) and fluid flow with moving boundaries (Greaves, 2004). An example of the quadtree (octree in 3D) is shown in Figure 2.2. The whole domain is a square (cube in 3D) and it is subdivided into smaller squares at subsequent levels of refinement. Each finite volume is referred to as a cell. The base cell is called the root of the tree and a leaf cell is a cell which cannot have any children. Each parent cell can have up to four children (8 in 3D). The root cell is designated as level 0 and the level of each subsequent cell is defined by parent level plus one to a group of four child descendants. Each cell has $\mathcal{N}_d$ direct neighbors in the same level, which can be accessed through the face, $\mathcal{C}_d$. Mixed cells are defined as the cells which are cut by a solid boundary.

Lets summarize the definitions of the various terms used in this thesis to describe

the graded quad/octree partitioning (Popinet, 2009).

- **Root cell**. The base of the cell tree. The root cell does not have a parent cell and all cells in the tree are descendants of the root cell.
- **Children cell**. The direct descendants of a cell. Cells other than leaf cells have four children in two dimensions (quadtree) and eight in three dimensions (octree).
- **Parent cell**. The direct ancestor of a given cell.
- **Leaf cell**. The highest cells in the cell tree. Leaf cells do not have children.
- **Cell level**. By convention the root cell is at level zero and each successive generation increases the cell level by one.
- **Coarser cell**. Cell $\mathcal{A}$ is coarser than cell $\mathcal{B}$ if level $(\mathcal{A})$ < level $(\mathcal{B})$ and conversely for finer cells.

Calculations at the cell boundaries are simplified by the following constraints:

1. direct neighboring cells cannot differ by a level more than one;
2. diagonally neighboring cells cannot differ by a level more than two; and
3. cells directly neighboring a cell containing the fluid/fluid interface should be at the same level.

These constraints greatly simplify the gradient and flux calculations. The first two constraints are less restrictive and usually impose gradual refinement. The third constraint on the other hand forces all the cells cut by the fluid/fluid interface to be at the same level and therefore is much more restrictive. One of the major issues with quad/octree grid partitioning is its inability to deal with highly non-isotropic flows since this sort of data structure imposes locally isotropic refinement. Approaches

to rectify this issue include using rectangular cells instead of square cells or using variable quad/octree hierarchy (Berger & Aftosmis, 1998). In general, the desirable characteristics of a data structure are:

(a) efficiently access adjoining cells;

(b) efficiently access cell levels and spatial coordinate information; and

(c) traverse cells at a given level, leaf cells and mixed cells efficiently.

In this research, a fully threaded tree (FFT) structure (Khokhlov, 1998) is used. The whole computational domain is level 0 i.e., the root cell (refer Figure 2.2). Cells on level 1, 2, 3 and 4 are child cells, while level 4 cells are the leaf cells. Cells at level 2 are coarser than that of level 1 and so on and so forth for levels 3 and 4. Using this approach, neighboring cells as well as different cell levels and spatial coordinates can be accessed using $\mathcal{O}(1)$ as opposed to $\mathcal{O}(logN)$ using a conventional linked list. The cost to perform operation (c) is $\mathcal{O}(NlogN)$. Every cell can efficiently access its child, neighbour, and parent cells. Only one pointer is needed to access these cells since cells in the tree are organized in groups and kept in contiguous memory locations. Each group of child cells also has a pointer to a parent cell and six (four in 2D) pointers to parent cells of neighbouring groups. The primitive state variables are stored at cell centers.

Often multiphase problems involve length and time scales varying over several orders of magnitude. Impinging jets, liquid jet in cross flow, droplet breakup, droplet collision and impact are a few examples. Traditionally, fixed mesh (structured) approaches have been used in numerical simulations to explore fluid dynamics phenomena. This meshing methodology have either considered uniform grids i.e., same refinement level throughout the computational domain or non-uniform i.e., finer mesh in the *expected* region of high gradients and coarser grid elsewhere. Even though several researchers in the past have used fixed mesh successfully for dynamically evolving

interfacial flows, this approach can be computationally extremely expensive and often cost prohibitive. Adaptive mesh refinement technique is one of the most efficient ways to mitigate this problem. The basic concept behind AMR methodology is to adapt the grid according to the specified criteria so that grid is only refined in regions where higher resolution is needed, while the rest of the computational domain uses a coarser mesh. AMR is specially useful for numerical simulation of multiphase flows where the fluid/fluid interface evolves in time. The AMR implementation in Gerris is based on structured grids. Structured mesh offers simplification in implementing the various numerical algorithms and reduces the computational overhead, in addition to the excellent mass conservation characteristics of this gridding methodology. The octree discretization further assists in the implementation of the multigrid V-cycle solver for the solution of the Poisson equation. Structured adaptive mesh refinement (SAMR) grid methods have been successfully used by researchers to explore a wide range of physical phenomena, ranging from large scale numerical relativity, cosmology and astrophysics simulations (Bryan & Norman, 2000; Bergmans *et al.*, 2005; Choptuik, 2000) to fluid dynamics and combustion simulations (Bell, 2005; Myers, 2000; Pernice *et al.*, 2000; Jourdren, 2005). The grid adaptation criteria depends on the physics under consideration. For the problem in hand, gradient and value based refinements are used at the liquid interface and the droplet interior respectively, to resolve the droplet shape, interior and the near flowfield. This is achieved by using a refinement indicator in each cell. The grid is refined or coarsened by comparing the refinement indicator to a predefined threshold value.

2.4 Surface Tension

The concept of tension in a free liquid surface is a familiar one, and is often given as an explanation to the tendency of liquid surfaces to take a shape with minimum potential energy. One of the most common examples of the effect of surface tension

force is the spherical shape of raindrops falling from the sky. Liquid molecules exert intermolecular forces on each other inside a liquid body. The directional nature of these forces, on an average, is random because of their fluctuating nature. As a result the average force experienced by a given molecule over a finite period of time is zero. This is analogical to the random motion of a gas in equilibrium which can be described by a Maxwellian velocity distribution and on an average the molecules have a zero random velocity. Since the average force experienced by a liquid molecule is zero, the work done by the molecule to move a given distance is also zero. The situation is different for the molecules on the interface/surface. These molecules are not surrounded by other molecules symmetrically and have to do a certain amount of work against the unbalanced forces in order to reach the free liquid surface. The direction of the forces is normal to the free surface (Burdon, 1940). In addition, the presence of different gas/liquid/solid on the other side of the interface play a major role in defining the nature of unbalanced forces experienced by the interfacial molecules. The surface molecules possess a potential energy because of the work done in reaching the surface. This is called the surface energy. The surface tension, σ, is defined as surface energy per unit area. It is expressed in N/m.

To look at the inter-molecular forces defining the surface tension, lets consider the molecular dynamics definition of surface tension (Alejandre *et al.*, 1995):

$$\sigma = \frac{1}{2} < P_{ZZ} - (P_{XX} + P_{YY}) > \tag{2.26}$$

where the angular brackets denote time averaging and $P_{\alpha\beta}$ is the $\alpha\beta$ component of the pressure tensor and is given by:

$$\begin{aligned} VP_{\alpha\beta} = & \sum_{i=1}^{N} m_i \left(\mathbf{v}_i\right)_\alpha \left(\mathbf{v}_i\right)_\beta \\ & + \sum_{i=1}^{N-1} \sum_{j>i}^{N} \sum_{a=1}^{3} \sum_{b=1}^{3} \left(\mathbf{r}_{ij}\right)_\alpha \left(\phi_{iajb}\right)_\beta \end{aligned} \tag{2.27}$$

where V is the volume of the system, N the number of molecules, m_i and $\mathbf{v}_i$ are the

molecular mass and velocity of the center of mass respectively. $\mathbf{r}_{ij}$ is the distance vector between the center of mass of molecules i and j. a and b are the sites of interest on any given molecule. The force between atom a in molecule i and atom b in molecule j, ϕ_{iajb} is given by:

$$\phi_{iajb} = -\frac{\mathbf{r}_{iajb}}{r_{iajb}} \left[\frac{dU\left(r_{iajb}\right)}{dr_{iajb}} \right] \tag{2.28}$$

r_{iajb} is the distance between atom a in molecule i and atom b in molecule j. $U(r_{ab})$ is the interaction between molecules. As an example, consider the extended simple point charge (SPC/E) model for water, the intermolecular interactions consists of three point charges located at the oxygen and hydrogen sites. The surface tension can be decomposed into Lennard-Jones and the Columbic surface tension components, which takes into account the short- and long-range intermolecular interactions respectively.

$$\begin{aligned} U\left(r_{ab}\right) =& 4\epsilon_{OO} \left[\left(\frac{\sigma_{OO}}{r_{OO}} \right)^{12} - \left(\frac{\sigma_{OO}}{r_{OO}} \right)^{6} \right] \\ &+ \frac{1}{4\pi\epsilon_0} \sum_{a=1}^{3} \sum_{b=1}^{3} \frac{q_a q_b}{r_{ab}} \end{aligned} \tag{2.29}$$

Here, q_a is the charge on site a and r_{ab} is the distance between sites a and b on two different molecules. The Lennard-Jones parameter is only evaluated between the oxygen sites and is given by: $\sigma_{OO} = 3.166\ \mathring{A}$ and $\epsilon_{OO} = 0.6502\ kJ/mol$ while $q_O = -0.8476|e|$ and $q_H = -q_O/2$.

2.4.1 Thermodynamics of Interfaces

Consider a one component liquid-gas equilibrium. Gravity has been neglected because of its negligible contribution for most applications. The interface is assumed to be flat so that the principal curvatures are 0. The change in internal energy, dU with extensive parameters (N, V, T, A) can be expressed as:

$$dU = TdS - pdV + \sigma dA + \mu_n dN \tag{2.30}$$

where $pdV = p^{\alpha}dV^{\alpha} + p^{\beta}dV^{\beta}$. α and β are the two phases. Integrating this equation under conditions of equilibrium, and without the loss of generalization, the lower limit of integration can be chosen such that:

$$U = TS - pV + \sigma A + \mu_n N \tag{2.31}$$

The free energy and its gradient for a process can be written as:

$$\begin{aligned} F &= U - TS \\ F &= -pV + \mu_n N + \sigma A \\ dF &= -pdV - SdT + \mu_n dN + \sigma dA \end{aligned} \tag{2.32}$$

where F is the free energy, A the area, S the entropy, T is the equilibrium temperature and μ_n is the chemical potential of the species, n. If the grand thermodynamic potential, Ω, is used, Equation 2.32 translates to:

$$\begin{aligned} \Omega &= F - \mu_S N \\ \Omega &= -pV + \sigma A \\ d\Omega &= -pdV - SdT - Nd\mu_n + \sigma dA \end{aligned} \tag{2.33}$$

The thermodynamic definition of surface tension, then becomes:

$$\begin{aligned} \sigma &= \left(\frac{\partial F}{\partial A}\right)_{N,V,T} \quad \text{or equivalently,} \\ \sigma &= \left(\frac{\partial \Omega}{\partial A}\right)_{\mu_n,V,T} \end{aligned} \tag{2.34}$$

Consider an interface between a liquid and gas. The total volume, V can be divided into the gas and liquid volumes, V_g and V_l respectively, with $V = V_g + V_l$. The densities in the liquid and gas phase are ρ_l and ρ_g. The interfacial number of particles, N_s are defined by:

$$\begin{aligned} N_s &= N - N_g - N_l \\ \Gamma &= \frac{N_s}{A} \end{aligned} \tag{2.35}$$

Since the liquid and vapor coexist, p, μ_n and T are fixed and the interfacial free energy is given by:

$$\begin{aligned} &F_s = F - F_l - F_g \quad \text{where} \\ &F = -pV + \mu_n N + \sigma A, \quad F_l = -pV_l + \mu_n N_l, \quad F_g = -pV_g + \mu_n N_g \\ &\therefore F_s = \sigma A + \mu_n N_s \end{aligned} \tag{2.36}$$

If we use the grand thermodynamic potential, Ω, the interface contribution is:

$$\Omega_s = \Omega - \Omega_l - \Omega_g = -pV + \sigma A - pV_l - pV_g = \sigma A \tag{2.37}$$

Using Equation 2.32, we can derive an equation for the surface entropy.

$$dF_s = S_s dT + \mu_n dN_s + \sigma dA \tag{2.38}$$

Differentiating Equation 2.36 we get:

$$dF_s = \sigma dA + A d\sigma + \mu_n dN_s + N_s d\mu_n \rightarrow -s_s dT = d\sigma + \Gamma d\mu_n \tag{2.39}$$

where $s_s = S_s/A$ is the surface entropy per unit area. If the adsorption is 0, the surface entropy per unit area is given by:

$$s_s = -\frac{d\sigma}{dT} \tag{2.40}$$

If a substance adsorbs and its concentration is increased the interfacial tension decreases and vice versa.

The definitions of surface tension, free energy and surface entropy for mixtures can be extrapolated directly from the above equations. For example, if there are $\nu = 1, 2, 3, ..., M$ species, the number of particles in the interface and adsorption can be defined by:

$$N_s^\nu = N - N_l^\nu - N_g^\nu \quad \text{and} \quad \Gamma^\nu = \frac{N_s^\nu}{A}, \quad \nu = 1, 2, 3, ..., M \tag{2.41}$$

The interfacial free energy and the surface Gibbs-Duhem equation are:

$$\begin{aligned} F_s &= \sigma A + \sum_{\nu} \mu_n^{(\nu)} N_s^{(\nu)} \\ -s_s dT &= d\sigma + \sum_{\nu} \Gamma^{(\nu)} d\mu_n^{(\nu)} \end{aligned} \tag{2.42}$$

The statistical mechanical definition of surface tension in terms of partition functions is:

$$\sigma = \left(\frac{\partial F}{\partial A}\right)_{N,V,T} = -kT \left(\frac{\partial log Q}{\partial A}\right)_{N,V,T} \tag{2.43}$$

where Q is the partition function.

2.4.2 Temperature Dependence of Surface Tension

To determine the dependence of surface tension on temperature, lets consider a single component liquid in contact with a gas which is insoluble and non-adsorbable on the liquid surface. Under such conditions Equation 2.40 is valid and we have $s_s = -\frac{d\sigma}{dT}$. The entropy in this case is related to the difference in the state of matter at the surface and the bulk phases. The volume density and entropy decreases much faster than entropy density when transitioning from liquid to gas and the surface is located in a region where there is a positive excess of entropy (Rusanov & Prokhorov, 1996). Then according to Equation 2.40, the surface tension of pure liquids decreases with increase in temperature.

Several relations have been developed over the years which show the temperature dependence of surface tension. In general since the surface tension decreases with temperature for most liquids and vanishes at the critical point, the simplest equation takes the form (Guggenheim, 1945):

$$\sigma = \sigma_0 \left(1 - \frac{T}{T_{cr}}\right)^{\zeta} \tag{2.44}$$

where ζ is a constant. This equation can be used to model the surface energy per unit area and can be written as:

$$\overline{u} = \sigma_0 \left(T_{cr} - T\right)^{\zeta - 1} \left[T_{cr} + (\zeta - 1)T\right] \tag{2.45}$$

Table 2.2. Empirical relations for temperature dependence of surface tension for pure liquids.

Correlation	Reference
$\frac{d\left(\sigma \overline{v}^{2/3}\right)}{dT} = \kappa_e$	Eotvos (1886)
$\sigma \overline{v}^{2/3} = \kappa_e \left(T_{cr} - T - 6\right)$	Ramsay & Shields (1893)
$\sigma \left(\frac{1}{\overline{v}^{\alpha}} - \frac{1}{\overline{v}^{\beta}}\right)^{-2/3} = \kappa_e T_{cr} \left(1 - \frac{T}{T_{cr}}\right)$	Katayama (1916)
$\sigma = \sigma_0 \left(1 - \frac{T}{T_{cr}}\right)^{11/9}$	Guggenheim (1945)
$\sigma = \sigma_0 \left(1 - \frac{T}{T_{cr}}\right)^{0.234}$	van der Waals (1894)

Most common correlations which describe the temperature dependence of surface tension are listed in Table 2.2. All these relations are based on empirical data and most of them take the form of Equation 2.44 with different different values of ζ. Here T_{cr} is the critical temperature, $\overline{v}$ is the molar volume and κ_e is the Eotvos constant ($=2.1 \times 10^{-7} Jmol^{-2/3} K^{-1}$).

2.4.3 Dependence of Surface Tension on Pressure and Carrier Gases

To understand the behavior of surface tension as a function of pressure, it is necessary to fix temperature and composition. Unfortunately, most of the gases used in experiments are adsorbed on the liquid substrate and the effect of pressure cannot be investigated because of the change in composition on the surface. In practice, such effects are studied by using gases which are almost inert in terms of absorption and adsorption. Helium is one of the least soluble gases and thus has been almost exclusively used in experiments designed to investigate the pressure effect on surface

tension. For a two-phase binary system with a flat interface, it can be shown that (Rusanov & Prokhorov, 1996):

$$A_m \left(\frac{d\sigma}{dp}\right)_T = \overline{v}^{\sigma} - \overline{v}^{\alpha} - \frac{\left(\overline{v}^{\beta} - \overline{v}^{\alpha}\right)\left(x^{\sigma} - x^{\alpha}\right)}{\left(x^{\beta} - x^{\alpha}\right)} \tag{2.46}$$

where A_m is the molar surface, i.e., the surface area per unit mole of the surface layer, $\overline{v}$ is the molar volume of the particular phase (or the surface layer designated by $\overline{v}^{\sigma}$) and x is the mole fraction of an extraneous substance. If α represents the liquid and β the gas phase and the gas is not absorbed or adsorbed on the liquid surface, then $x^{\sigma} = x^{\alpha} \approx 0$ and 2.46 becomes:

$$A_m \left(\frac{d\sigma}{dp}\right)_T = \overline{v}^{\sigma} - \overline{v}^{\alpha} > 0 \tag{2.47}$$

The above equation suggests that surface tension should increase with pressure for a system where the gas enters the liquid very slightly (through absorption and adsorption). Once adsorption becomes substantial, $x^{\sigma} > x^{\alpha}$, and the second term in Equation 2.46 dominates and suggests a decrease in surface tension with increasing pressure. As pointed before, unfortunately, no conclusion can be made regarding the pressure effect once adsorption become appreciable. Figure 2.3 (Massoudi & King Jr., 1974; Luijten *et al.*, 1997) shows the variation of surface tension of water with pressure in the presence of various carrier gases. The first observation which can be made from the figure is that, in the presence of He, the surface tension of water slightly increases with pressure. This observation is consonance with Equation 2.47 because the adsorptivity of He on water surface is extremely low. To decipher the effect of pressure on the surface tension of water in the presence of H_2, N_2, CH_4, N_2O and CO_2, lets take a look at the adsorption behavior of gases as a function of pressure, known as adsorption isotherms in the literature.

In general, the adsorptivity of gases increases with pressure. The earliest adsorption isotherm was developed by Freundlich (1922). It was predominantly empirical

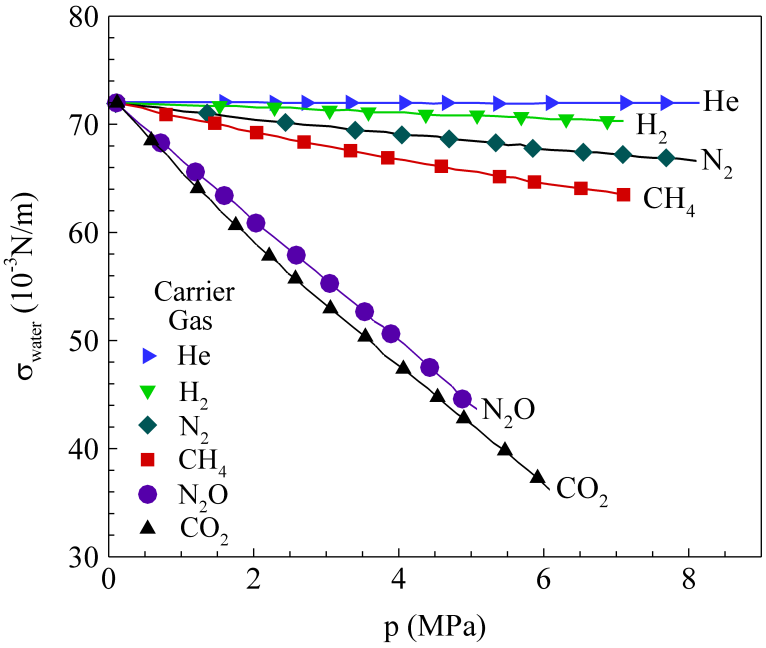

Figure 2.3. Variation of surface tension of water with pressure at 298 K in the presence of various ambient gases (Massoudi & King Jr., 1974; Luijten *et al.*, 1997).

in nature and there was no theoretical basis to the correlation. It took a form:

$$log v_{ad} = log\chi + \frac{1}{n} logp \tag{2.48}$$

where v_{ad} is the volume of gas adsorbed and n is a constant greater than 1. Probably the most celebrated theory in the field of adsorption is due to Langmuir (1918). The theory is based on two assumptions; (a) the force of interaction between the adsorbed molecules is negligible, and (b) the postulate of unimolecular adsorption. According to Langmuir's theory:

$$\begin{aligned} v_{ad}/v_{max} &= \theta = \frac{bp}{1+bp} \\ b &= \frac{\alpha_0 e^{q/\kappa_b T}}{\kappa_0 (2\pi m \kappa_b T)^{1/2}} \end{aligned} \tag{2.49}$$

where κ_b is the Boltzmann constant, α_0 is the condensation coefficient and m is the mass of the molecule. b is called the adsorption coefficient and is only a function of temperature. At high adsorbate pressures and thus high coverage, this simple

isotherm fails to predict experimental results and thus cannot provide a correct explanation of adsorption under these conditions. One plausible reason for this behavior is the possibility of multilayer adsorption. This means that the initial layer of adsorbate acts as a substrate surface itself, allowing for more adsorption beyond a saturated (monolayer) coverage. Over the last century or so, there have been several theories which considered multimolecular adsorption, i.e., adsorption more than one layer thick. One of the notable theories is called BET theory named after Brunauer, Emmett & Teller (1938). According to the BET isotherm, since condensation of the adsorbate is indefinite, the amount of adsorption increases as the pressure is increased. If adsorption is much stronger than condensation, the BET isotherm reduces to:

$$\theta = \frac{1}{1 - \frac{p}{p_0}} \tag{2.50}$$

where p_0 is the vapor pressure of pure condensed adsorbate. An excellent reference which describes the various adsorption theories in great detail the book by Brunauer (1945).

As evident from the discussion in the previous paragraph, gas adsorption generally increases with increase in pressure. Then according to Equation 2.46, the surface tension should decease with increasing pressure. In summary, the increase in adsorption of gases with pressure leads to the decrease in surface tension and explains the trends in Figure 2.3.

2.5 Closing Remarks

This chapter discussed the theoretical basis of the current research. Governing equation and boundary conditions were described first, followed by a brief discussion on the non-dimensional parameters, relevant for droplet dynamics study. Numerical model used to solve the discretized equations and octree spatial discretization were discussed next. The chapter ends with a detailed account of surface tension and its dependence on temperature, pressure and composition.

CHAPTER III

NUMERICAL METHODS

In this chapter, the numerical method used to solve the governing equations described in Chapter 2 are presented. The numerical schemes presented in this chapter are based on Popinet (2003, 2009) and Zakerzadeh (2008). The temporal discretization is introduced first, followed by the details of the numerical schemes used to model convective and viscous terms. The volume of fraction advection scheme is discussed next, along with the balanced force algorithm used to model surface tension. The generalized height function used in the balance force algorithm to estimate the curvature is then described. Examination of time step constraints is followed by verification and validation studies conducted, relevant to droplet deformation and breakup. In addition, results are compared with data from literature (whenever available), in subsequent chapters while discussing the results obtained during the current research effort.

3.1 Time Integration

A second order accurate, time staggered discretization for volume-fraction/density is used, given by:

$$\rho^{n+1/2}\left[\frac{\mathbf{u}^{n+1}-\mathbf{u}^{n}}{\triangle t}+\nabla.\left(\mathbf{uu}\right)^{n+1/2}\right]=-\nabla p^{n+1/2}+\nabla.\left[\widetilde{\tau}_{n}+\widetilde{\tau}^{n+1}\right]+{\mathbf{F_{st}}}^{n+1/2} \quad (3.1)$$

$$\frac{f^{n+1/2}-f^{n-1/2}}{\triangle t}+\nabla.\left(f^{n}\mathbf{u}^{n}\right)=0 \quad (3.2)$$

$$\nabla.\mathbf{u}^{n}=0 \quad (3.3)$$

A classical fractional step projection method is used to simplify the above equations, where the time discretization of the momentum equation (pressure form) is split into two steps, a predictor step followed by a corrector step. It can be written as (Popinet,

2009):

$$\rho^{n+1/2}\left[\frac{\mathbf{u}^{*}-\mathbf{u}^{n}}{\triangle t}+\nabla.\left(\mathbf{uu}\right)^{n+1/2}\right]=\nabla.\left[\widetilde{\tau}_{n}+\widetilde{\tau}^{*}\right] \tag{3.4}$$

$$\frac{f^{n+1/2}-f^{n-1/2}}{\triangle t}+\nabla.\left(f^{n}\mathbf{u}^{n}\right)=0 \tag{3.5}$$

$$\mathbf{u}^{n+1}=\mathbf{u}^{*}-\frac{\triangle t}{\rho^{n+1/2}}\nabla p^{n+1/2}+{\mathbf{F_{st}}}^{n+1/2} \tag{3.6}$$

$$\nabla.\mathbf{u}^{n+1}=0 \tag{3.7}$$

The above method requires the solution of a Poisson equation for pressure:

$$\nabla.\left[\frac{1}{\rho^{n+1/2}}\nabla p^{n+1/2}\right]=\nabla.\left(\frac{\mathbf{u}^{*}}{\triangle t}+\frac{{\mathbf{F_{st}}}^{n+1/2}}{\rho^{n+1/2}}\right) \tag{3.8}$$

Equation 3.8 is solved using an octree based multigrid solver (Popinet, 2003). It should be noted that the surface tension effects are incorporated with the pressure correction equation to implement the balanced force algorithm proposed by Francois *et al.* (2006). The basic idea is to consider these two terms together in order to cancel the discretization errors thereby enforcing an exact balance. The next section details the spatial discretization schemes used in the above equations.

3.2 Spatial Discretization

As described before in Section 2.3, a graded octree partitioning is used in conjunction with a Cartesian VOF approach to solve the governing equations. The primitive variables are calculated at the center of each cube, their values being the volume average of the corresponding cell. A Godunov momentum advection scheme (Bell *et al.*, 1989) is used for the discretization of the convective terms while the viscous terms are implemented using a Crank-Nicholson type of discretization. The next sections discuss the spatial numerical schemes used to discretize the various terms in Equations 3.4 and 3.6.

3.2.1 Advection Term

The advection term is evaluated using a conservative formulation. Gauss's divergence theorem can be used to convert the volume integral over a control volume, Ω, to a surface integral over a surface S.

$$\int_{\Omega} \nabla.\left(\mathbf{uu}\right)^{n+1/2} d\Omega = \frac{1}{\Omega} \int_{S} \mathbf{u}^{n+1/2} \left(\mathbf{u}^{n+1/2}.\widehat{n}_S\right) dS \tag{3.9}$$

where $\widehat{n}_S$ is the unit outward normal to the surface S. The discretized form of the advection terms in x-direction for the control volume shown in Figure 3.1 can be written as:

$$\begin{aligned}\int_{\Omega} \nabla.\left(\mathbf{uu}\right)^{n+1/2} d\Omega =& \frac{1}{\triangle}\big[\left(u_{i+1/2,j,k}u_{i+1/2,j,k} - u_{i-1/2,j,k}u_{i-1/2,j,k}\right) \\ &+ \left(v_{i,j+1/2,k}u_{i,j+1/2,k} - v_{i,j-1/2,k}u_{i,j-1/2,k}\right) \\ &+ \left(w_{i,j,k+1/2}u_{i,j,k+1/2} - w_{i,j,k-1/2}u_{i,j,k-1/2}\right)\big]^{n+1/2}\end{aligned} \tag{3.10}$$

The advection terms in the y and z direction can be written in a similar manner. A Godunov method (Bell *et al.*, 1989) is implemented which requires the face-centered values of the primitive variables. It is a second order Taylor series expansion in space and time. The face-centered values can be calculated either using the left (i, j, k) or the right $(i + 1, j, k)$ side of the face. In general, the Taylor series expansion for the face-centered values can be written as:

$$\mathbf{u}^{L,n+1/2}_{i+1/2,j,k} = \mathbf{u}^{n}_{i,j,k} + \frac{\triangle}{2}\partial_x \mathbf{u} + \frac{\triangle t}{2}\partial_t \mathbf{u} + O\left(\triangle^2, \triangle t^2\right) \tag{3.11}$$

∂_x is the cell-centered derivative in x direction extrapolated from the left side of the face denoted by the superscript L. The time derivative, ∂_t can be substituted from Equation 2.4, leading to:

$$\begin{aligned}u^{L,n+1/2}_{i+1/2,j,k} =& u^{n}_{i,j,k} + \left(\frac{\triangle}{2} - \frac{\triangle t}{2}u^{n}_{i,j,k}\right)\partial_x u^{n}_{i,j,k} \\ &+ \frac{\triangle t}{2}\left[\left(-v\partial_y u - w\partial_z u\right)^{n}_{i,j,k} + \frac{1}{\rho^{n}_{i,j,k}}\left(\mu\left(\nabla\mathbf{u} + \left(\nabla\mathbf{u}\right)^{T}\right)\right)^{n}_{i,j,k}\right]\end{aligned} \tag{3.12}$$

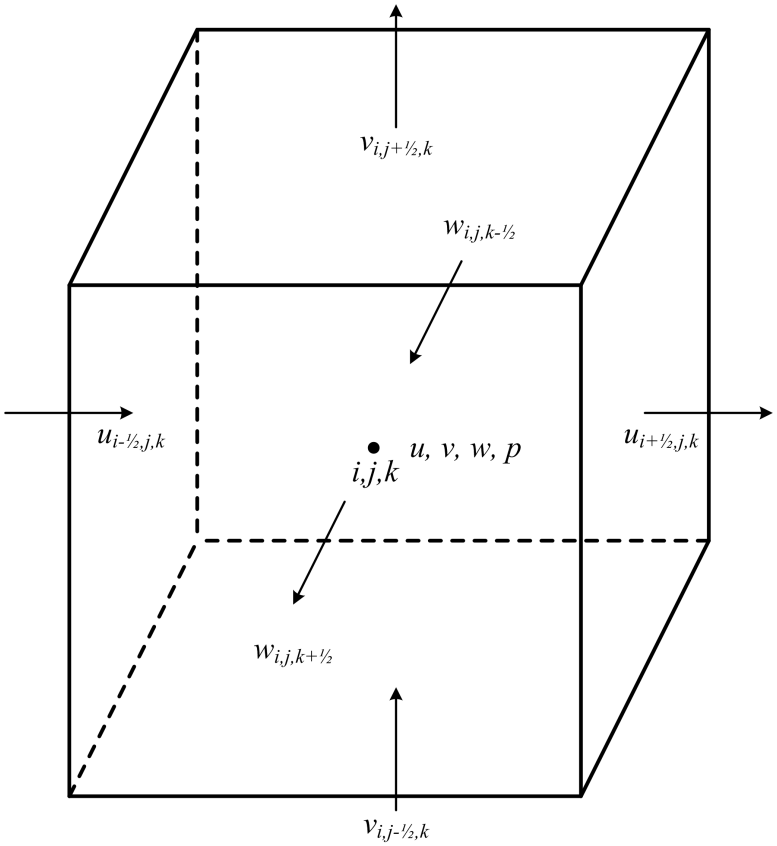

Figure 3.1. Computational cell with coordinates (i, j, k). The length of each side is $\triangle$. Velocities u, v, and w and pressure p are specified at the cell centers. Advection velocities are defined at the center of cell faces.

Similar equation can be written for extrapolating the face-centered values from cell center $(i+1, j, k)$. The y and z components of velocity can be evaluated using corresponding derivatives. The pressure and surface tension forces are not included in Equation 3.12 because they are only required in the projection step. The discretization of the viscous stress tensor, $\widetilde{\tau}$, will be presented in Section 3.2.2. Using a simple upwind scheme, the face-centered values can be extrapolated from the left or right of the face and corresponding to $u^{L,n+1/2}_{i+1/2,j,k}$ and $u^{R,n+1/2}_{i+1/2,j,k}$ respectively.

$$u^{L,n+1/2}_{i+1/2,j,k} = u^n_{i,j,k} + \frac{\triangle}{2} min\left(1 - u^n_{i,j,k}\frac{\triangle t}{\triangle}, 1\right) + \frac{\triangle t}{2}\left(-v\overline{\partial_y}u - w\overline{\partial_z}u\right)^n_{i,j,k} \tag{3.13}$$

where $\overline{\partial}$ is the upwind derivative given by:

$$\overline{\partial_y}u^n_{i,j,k} = \begin{cases} (\nabla u)^n_{i,j+1/2,k} & v^n_{i,j,k} < 0, \\ (\nabla u)^n_{i,j-1/2,k} & v^n_{i,j,k} > 0. \end{cases} \tag{3.14}$$

where ∇ is the face-centered gradient. $\overline{\partial_z}u^n_{i,j,k}$ can be computed in a similar fashion. The upwind value is chosen as:

$$\mathbf{u}^{n+1/2}_{i+1/2,j,k} = \begin{cases} \mathbf{u}^{L,n+1/2}_{i+1/2,j,k} & u^n_{i+1/2,j,k} > 0, \\ \mathbf{u}^{R,n+1/2}_{i+1/2,j,k} & u^n_{i+1/2,j,k} < 0, \\ \frac{1}{2}\left(\mathbf{u}^{R,n+1/2}_{i+1/2,j,k} + \mathbf{u}^{L,n+1/2}_{i+1/2,j,k}\right) & u^n_{i+1/2,j,k} = 0. \end{cases} \tag{3.15}$$

Similarly upwind values can be calculated for the faces perpendicular to y and z directions, $\mathbf{u}^{n+1/2}_{i,j+1/2,k}$ and $\mathbf{u}^{n+1/2}_{i,j,k+1/2}$ respectively. Face- and time-centered normal velocities, $\widehat{\mathbf{u}}^{n+1/2}$, are calculated in order to compute the advection term in Equation 3.9. To guarantee the conservative nature of the method, it is imperative for the normal velocities to be discretely divergence-free. Step 1 is to calculate the normal velocities as described above. The upwind state $\widehat{\mathbf{u}}^*$ is then selected for each face using Equation 3.15, where $u^n_{i+1/2,j,k}$ is obtained by linear interpolation of the cell-centered velocities sharing the face. To enforce divergence-free nature of the normal velocities,

a projection step is applied by solving:

$$\nabla.\left[\left(\frac{1}{\rho^{n+1/2}}\nabla p^{n+1/2}\right)_{fc}\right]_{cc} = \nabla.\left[\left(\frac{\mathbf{u}^*}{\triangle t} + \frac{\mathbf{F_{st}}^{n+1/2}}{\rho^{n+1/2}}\right)_{fc}\right]_{cc} \tag{3.16}$$

where $(.)_{fc}$ and $(.)_{cc}$ denote face- and cell-centered respectively. Face- and time-centered, divergence-free normal velocities are obtained by correcting $\widehat{\mathbf{u}}^*$ with the pressure solution. For example for a face $(i+1/2, j, k)$:

$$u^{n+1/2}_{i+1/2,j,k} = u^*_{i+1/2,j,k} - \frac{\triangle t}{\rho^n_{i+1/2,j,k}}\left[(\nabla p)_{i+1/2,j,k} + (\mathbf{F_{st}})_{i+1/2,j,k}\right] \tag{3.17}$$

Similar calculations can be performed for the faces perpendicular to y and z directions. Cell centered pressure gradient is also computed while correcting the normal velocities using simple averaging of gradient faces. For example for gradient in x direction for a cell, (i, j, k):

$$(\nabla_x p)_{i,j,k} = \frac{(\nabla_x p)_{i+1/2,j,k} + (\nabla_x p)_{i-1/2,j,k}}{2} \tag{3.18}$$

To compute the advection terms, the above process is repeated but this time using the divergence-free, face- and time-centered normal velocities obtained in Equation 3.17. This makes the approach robust, especially for flow around sharp edges.

3.2.2 Viscous Terms

The second term on RHS of the Equation 2.4 is the viscous term. The shear stress tensor $\widetilde{\tau}$ can be written as:

$$\widetilde{\tau} = D_1 + D_2 \tag{3.19}$$

where $D_1 = \mu\nabla\mathbf{u}$ and $D_2 = \mu\nabla\mathbf{u}^T$. Lets consider the expansion of D_1:

$$\begin{aligned}\nabla.\mu\nabla\mathbf{u} = &\left[\frac{\partial}{\partial x}\left(\mu\frac{\partial u}{\partial x}\right) + \frac{\partial}{\partial y}\left(\mu\frac{\partial u}{\partial y}\right) + \frac{\partial}{\partial z}\left(\mu\frac{\partial u}{\partial z}\right)\right]\widehat{i} \\ &+ \left[\frac{\partial}{\partial x}\left(\mu\frac{\partial v}{\partial x}\right) + \frac{\partial}{\partial y}\left(\mu\frac{\partial v}{\partial y}\right) + \frac{\partial}{\partial z}\left(\mu\frac{\partial v}{\partial z}\right)\right]\widehat{j} \\ &+ \left[\frac{\partial}{\partial x}\left(\mu\frac{\partial w}{\partial x}\right) + \frac{\partial}{\partial y}\left(\mu\frac{\partial w}{\partial y}\right) + \frac{\partial}{\partial z}\left(\mu\frac{\partial w}{\partial z}\right)\right]\widehat{k}\end{aligned} \tag{3.20}$$

Discretization of the x component of the above equation for a control volume (i, j, k) is given by (Zakerzadeh, 2008):

$$
\begin{aligned}
2\triangle\left[\frac{\partial}{\partial x}\left(\mu\frac{\partial u}{\partial x}\right)+\frac{\partial}{\partial y}\left(\mu\frac{\partial u}{\partial y}\right)+\frac{\partial}{\partial z}\left(\mu\frac{\partial u}{\partial z}\right)\right]_{i,j,k} &= \left[\left(\mu\frac{\partial u}{\partial x}\right)_{i+1/2,j,k}-\left(\mu\frac{\partial u}{\partial x}\right)_{i-1/2,j,k}\right] \\
&+\left[\left(\mu\frac{\partial u}{\partial y}\right)_{i,j+1/2,k}-\left(\mu\frac{\partial u}{\partial y}\right)_{i,j-1/2,k}\right] \\
&+\left[\left(\mu\frac{\partial u}{\partial z}\right)_{i,j,k+1/2}-\left(\mu\frac{\partial u}{\partial z}\right)_{i,j,k-1/2}\right]
\end{aligned}
\tag{3.21}
$$

Similar equations can be derived for the other two directions. To evaluate the individual terms in Equation 3.21 face-centered velocity gradients and dynamic viscosities are used:

$$
\begin{aligned}
\left(\mu\frac{\partial u}{\partial x}\right)_{i+1/2,j,k} &= \mu_{i+1/2,j,k}\frac{u_{i+1,j,k}-u_{i,j,k}}{\triangle} \\
\left(\mu\frac{\partial u}{\partial x}\right)_{i-1/2,j,k} &= \mu_{i-1/2,j,k}\frac{u_{i,j,k}-u_{i-1,j,k}}{\triangle} \\
\left(\mu\frac{\partial u}{\partial y}\right)_{i,j+1/2,k} &= \mu_{i,j+1/2,k}\frac{u_{i,j+1,k}-u_{i,j,k}}{\triangle} \\
\left(\mu\frac{\partial u}{\partial y}\right)_{i,j-1/2,k} &= \mu_{i,j-1/2,k}\frac{u_{i,j,k}-u_{i,j-1,k}}{\triangle} \\
\left(\mu\frac{\partial u}{\partial z}\right)_{i,j,k+1/2} &= \mu_{i,j,k+1/2}\frac{u_{i,j,k+1}-u_{i,j,k}}{\triangle} \\
\left(\mu\frac{\partial u}{\partial z}\right)_{i,j,k-1/2} &= \mu_{i,j,k-1/2}\frac{u_{i,j,k}-u_{i,j,k-1}}{\triangle}
\end{aligned}
\tag{3.22}
$$

Similar to D_1, the expansion of D_2 is given by:

$$
\begin{aligned}
\nabla.\mu\nabla\mathbf{u}^T &= \left[\frac{\partial}{\partial x}\left(\mu\frac{\partial u}{\partial x}\right)+\frac{\partial}{\partial y}\left(\mu\frac{\partial v}{\partial x}\right)+\frac{\partial}{\partial z}\left(\mu\frac{\partial w}{\partial x}\right)\right]\widehat{i} \\
&+\left[\frac{\partial}{\partial x}\left(\mu\frac{\partial u}{\partial y}\right)+\frac{\partial}{\partial y}\left(\mu\frac{\partial v}{\partial y}\right)+\frac{\partial}{\partial z}\left(\mu\frac{\partial w}{\partial y}\right)\right]\widehat{j} \\
&+\left[\frac{\partial}{\partial x}\left(\mu\frac{\partial u}{\partial z}\right)+\frac{\partial}{\partial y}\left(\mu\frac{\partial v}{\partial z}\right)+\frac{\partial}{\partial z}\left(\mu\frac{\partial w}{\partial z}\right)\right]\widehat{k}
\end{aligned}
\tag{3.23}
$$

D_2 is also discretized using a second order accurate central scheme. As an example let's consider the y component of the above equation for at (i, j, k):

$$2\triangle\left[\frac{\partial}{\partial x}\left(\mu\frac{\partial u}{\partial y}\right)+\frac{\partial}{\partial y}\left(\mu\frac{\partial v}{\partial y}\right)+\frac{\partial}{\partial z}\left(\mu\frac{\partial w}{\partial y}\right)\right]=\left[\left(\mu\frac{\partial u}{\partial y}\right)_{i+1/2,j,k}-\left(\mu\frac{\partial u}{\partial y}\right)_{i-1/2,j,k}\right]+\left[\left(\mu\frac{\partial v}{\partial y}\right)_{i,j+1/2,k}-\left(\mu\frac{\partial v}{\partial y}\right)_{i,j-1/2,k}\right]+\left[\left(\mu\frac{\partial w}{\partial y}\right)_{i,j,k+1/2}-\left(\mu\frac{\partial w}{\partial y}\right)_{i,j,k-1/2}\right] \tag{3.24}$$

The discretization in the other two directions is analogous to the above equation. A harmonic mean is used to obtain the value of viscosity, μ, at the face-centers. For example:

$$\mu_{i+1/2,j,k}=\frac{2\mu_{i+1,j,k}\mu_{i,j,k}}{\mu_{i+1,j,k}+\mu_{i,j,k}} \tag{3.25}$$

where the viscosity is calculated according to Equation 2.8 and is a function of the volume fraction in a given cell. Similar expressions can be obtained for the viscosity evaluation at other faces.

3.2.3 Surface Tension

Surface tension estimation and its implementation is one of the most difficult aspects of the application of VOF methods to interfacial flows. In the current research, surface tension is evaluated using Equation 2.10, approximated by the Continuum Surface Force (CSF) approach proposed by Brackbill *et al.* (1992). According to CSF:

$$\sigma\kappa\delta_S\widehat{\mathbf{n}}\approx\sigma\kappa\nabla f \tag{3.26}$$

This approach has been reported by several researchers (Popinet & Zaleski, 1999; Harvie *et al.*, 2006; Jamet *et al.*, 2002; Lafaurie *et al.*, 1994; Scardovelli & Zaleski, 1999) to suffer from parasitic currents when applied to the case of stationary droplet in theoretical equilibrium. The spurious currents scale as the inverse of the Weber

number Harvie *et al.* (2006). To resolve this problem we consider a balanced force algorithm proposed by Francois *et al.* (2006) where the spurious currents are mitigated by a consistent coupling of the surface tension force with pressure gradient forces within the flow algorithm. It should be noted that for the current study (for most of cases), the Weber numbers are relatively large and even if the original CSF model was used the magnitude of spurious currents would have been relatively minute. The surface tension force, $\mathbf{F}_{st}$, is non-zero only on faces where the face gradient of the volume fraction is non-zero. To ensure this, discrete approximations of gradient of pressure and volume fraction should be compatible. In the present collocated scheme, this is performed by the following:

1. apply the surface tension force to the auxiliary face-centered velocity field $\mathbf{u}^*_{fc}$ as:

$$\mathbf{u}^*_{fc} \longleftarrow \mathbf{u}^*_{fc} + \frac{\triangle t \sigma \kappa^{n+1/2}_{fc}}{\rho f^{n+1/2}_{fc}} \nabla_{fc} f^{n+1/2} \tag{3.27}$$

2. apply the corresponding cell-centered surface tension force to $\mathbf{u}^*_{cc}$ as:

$$\mathbf{u}^*_{cc} \longleftarrow \left[\mathbf{u}^*_{cc} + \frac{\triangle t \sigma \kappa^{n+1/2}_{fc}}{\rho^{n+1/2}_{fc}} \nabla_{fc} f^{n+1/2} \right]_{cc} \tag{3.28}$$

This is exactly how the pressure term is treated in the approximate projection method. To see an explicit example of the spatial discretization used in the above steps, lets consider a cube face, $(i + 1/2, j, k)$. Surface tension can be estimated by:

$$(\mathbf{F}_{st})_{i+1/2,j,k} = \sigma \kappa_{i+1/2,j,k} (\nabla f)_{i+1/2,j,k} \tag{3.29}$$

where $\kappa_{i+1/2,j,k}$ is the curvature at the cell face interpolated from the cell center values:

$$\kappa_{i+1/2,j,k} = \begin{cases} \frac{1}{2} (\kappa_{i,j,k} + \kappa_{i+1,j,k}) & \text{if the interface is between } (i,j,k) \text{ and } (i+1,j,k) \\ \kappa_{i,j,k} & \text{if the interface is completely inside } (i,j,k) \end{cases} \tag{3.30}$$

Since in Equation 3.18, the cell centered pressure is computed simply by taking the mean of the adjacent faces, the surface tension force is calculated in a similar manner. As an example the cell centered surface tension force in x direction can be estimated by:

$$(\mathbf{F}_{st})_x = \frac{(\sigma\kappa\nabla f)_{i+1/2,j,k} + (\sigma\kappa\nabla f)_{i-1/2,j,k}}{2} \tag{3.31}$$

3.2.3.1 Height Function Curvature Calculation

To evaluate the surface tension term (eq. 3.26), estimation of interface curvature is required. In addition, interface advection and geometrical flux estimation depends on the accuracy of curvature evaluation as described in Section 3.3.2. The curvature of the interface in the current numerical methodology is calculated using the height function (HF) approach. It is a VOF based technique for the calculation of interface normals and curvatures. The method proceeds in three basic steps beginning with the determination of interface normal along with the direction of the maximal component. This is followed by the summation of the volume fractions along the direction of maximum normal component to evaluate the "height" function. In the last step the curvature is calculated using second-order central differences. Lets illustrate the above mentioned procedure for 2D and 3D cases. A 7x3 stencil is constructed around the interface as shown in Figure 3.2. In this example $|n_x| < |n_y|$. The red line represents the fluid-fluid interface and the normal in the $(i,j)^{th}$ cell is shown by the green arrow. The heights, g_i, is evaluated by summing the volume fractions vertically (in this case). For example, for g_{i-1}

$$g_{i-1} = \triangle \sum_{w=j-3}^{w=j+3} f_{i-1,w} \tag{3.32}$$

g_i and g_{i+1} can be calculated similarly. The heights are then used to calculate the interface normal and the curvature, κ given by:

$$\begin{aligned} \mathbf{n} &= (g_x, -1) \\ \kappa &= \frac{g_{xx}}{\left(1 + g_x^2\right)^{3/2}} \end{aligned} \tag{3.33}$$

where the derivatives are calculated using second-order central differences, $g_x = \frac{g_{i+1} - g_{i-1}}{2\triangle}$ and $g_{xx} = \frac{g_{i+1} - 2g_i + g_{i-1}}{\triangle^2}$.

A similar procedure is followed in 3D with a 7x3x3 stencil as shown in Figure 3.3, which shows the top view of an octree discretization. In this example the normal has the maximum component in the z direction (pointing into the paper). The interface normal and curvature for a cube (i, j, k) is then calculated by:

$$\begin{aligned} &\mathbf{n} = (g_x, g_y, -1), \text{ and} \\ &\kappa = \frac{g_{xx}\left(1 + g_y^2\right) + g_{yy}\left(1 + g_x^2\right) - 2g_{xy}g_xg_y}{\left(1 + g_x^2 + g_y^2\right)^{3/2}} \end{aligned} \tag{3.34}$$

The cross derivative is given by:

$$g_{xy} = \frac{g_{i+1,j+1} + g_{i-1,j-1} - g_{i-1,j+1} - g_{i+1,j-1}}{4\triangle^2} \tag{3.35}$$

The CSF model (3.27) requires face-centred interface curvature estimates. The face-centred curvatures are computed either by averaging the cell-centred curvatures of the neighbouring cells when they both contain the interface, or by taking the value of the cell-centred curvature in either cell containing the interface. L_∞ norms of interface curvature obtained by the height function approach, as described above, consistently shows second-order convergence as shown by Tryggvason (2011).

3.3 Volume of Fluid Advection

The volume of fluid advection equation (3.2) is solved using a piecewise-linear geometrical VOF scheme as explained in detail by Scardovelli & Zaleski (1999). There are two basic steps in our geometrical VOF scheme:

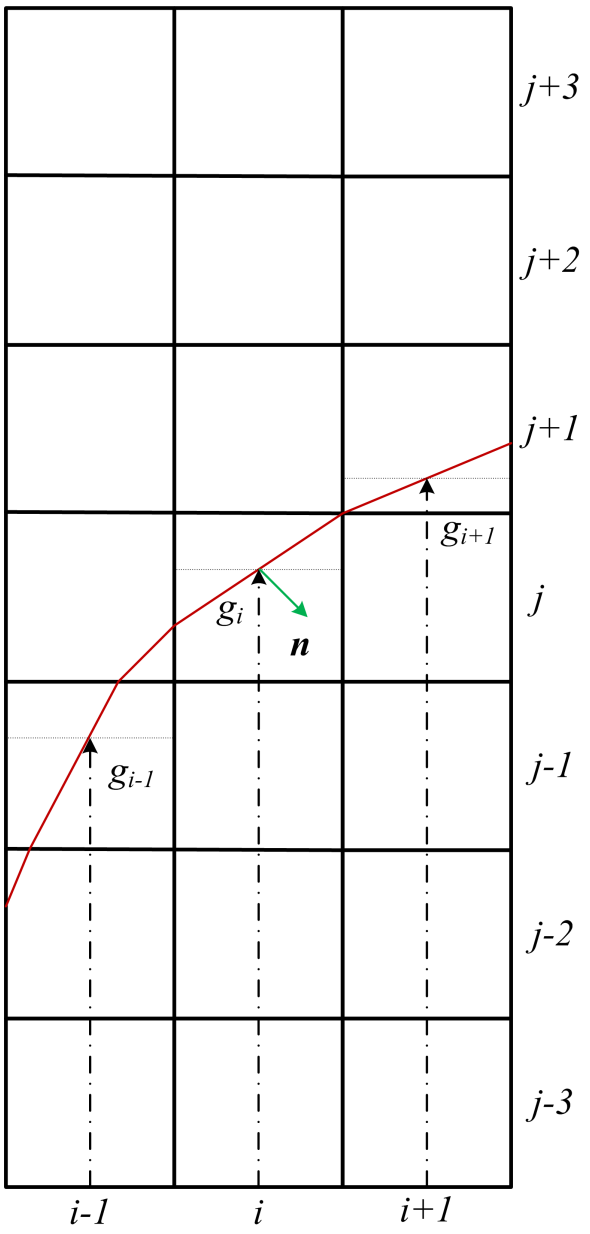

Figure 3.2. 7x3 stencil used to compute the height function when $|n_x| < |n_y|$.

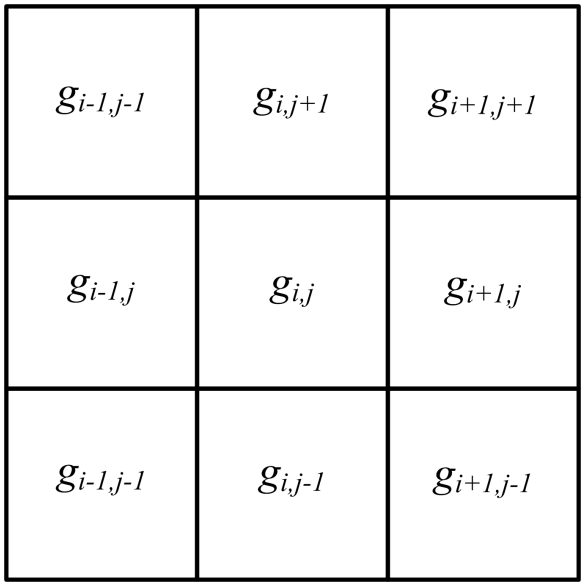

Figure 3.3. 7x3x3 stencil used to compute the height function in 3D.

1. interface reconstruction; and

2. interface advection and geometrical flux computation.

These two steps are explained in brief below.

3.3.1 Interface Reconstruction

The interface is represented by a plane in our VOF scheme, described by:

$$m_1 x_1 + m_2 x_2 + m_3 x_3 = \beta \tag{3.36}$$

Here m_1, m_2 and m_3 are the components of the normal vector $\mathbf{m}$ with position vector (x_1, x_2, x_3) and sides $\triangle x_1$, $\triangle x_2$ and $\triangle x_3$. β has a unique value determined by ensuring that the volume of fluid contained in the cell and lying below the plane is f. The method used to determine the volume fraction given $\mathbf{m}$ and β or inversely β given f

and **m** is adopted from Scardovelli & Zaleski (2000). For the forward problem:

$$V = \begin{cases} \dfrac{\beta^3}{6m_1m_2m_3} & \text{if} \quad 0 \le \beta < m_1 \\ \dfrac{\beta(\beta - m_1)}{2m_2m_3} + V_1 & \text{if} \quad m_1 \le \beta < m_2 \\ \dfrac{\beta^2(3m_{12} - \beta) + m_1^2(m_1 - 3\beta) + m_2^2(m_2 - 3\beta)}{6m_1m_2m_3} & \text{if} \quad m_2 \le \beta < m_3 \end{cases}$$

There are two possibilities for the fourth case:

$$V = \begin{cases} \dfrac{\beta^2(3 - 2\beta) + m_1^2(m_1 - 3\beta) + m_2^2(m_2 - 3\beta) + m_3^2(m_3 - 3\beta)}{6m_1m_2m_3} & \text{if} \quad m_3 \le \beta \le 1/2 \\ \dfrac{2\beta - m_{12}}{2m_3} & \text{if} \quad m_{12} \le \beta \le 1/2 \end{cases} \tag{3.37}$$

$V_1 = m_1^2/max(6m_2m_3, \epsilon)$ where ϵ is an arbitrary small number and is used as a delimiter to ensure that the denominator of V_1 does not become zero. $m_{12} = m_1 + m_2$ and $m = min(m_{12}, m_3)$. For the inverse problem:

$$\begin{aligned} &\beta = \sqrt[3]{6m_1m_2m_3V} && \text{if} \quad 0 \le V < V_1 \\ &\beta = \frac{1}{2}\left(m_1 + \sqrt{m_1^2 + 8m_2m_3(V - V_1)}\right) && \text{if} \quad V_1 \le V < V_2 \\ &P(\beta) = a_3\beta^3 + a_2\beta^2 + a_1\beta + a_0 = 0 && \text{if} \quad V_2 \le V < V_3 \end{aligned} \tag{3.38}$$

Again there are two possibilities for the fourth case:

$$\begin{aligned} &P(\beta) = b_3\beta^3 + b_2\beta^2 + b_1\beta + b_0 = 0 && \text{if} \quad V_{31} \le V \le 1/2 \\ &\beta = m_3V + \frac{m_{12}}{2} && \text{if} \quad V_{32} \le V \le 1/2 \end{aligned}$$

where $V_2 = V_1 + (m_2 - m_1)/2m_3$, $V_3 = V_{31} = [m_3^2(3m_{12} - m_3) + m_1^2(m_1 - 3m_3) + m_2^2(m_2 - 3m_3)]/(6m_1m_2m_3)$ when $m = m_3$ or $V_3 = V_{32} = m_{12}/2m_3$ when $m = m_{12}$. The coefficients of the two cubic polynomials are given by:

$$a_0 = m_1^3 + m_2^3 - 6m_1m_2m_3V$$

$$a_1 = -3(m_1^2 + m_2^2)$$

$$a_2 = 3m_{12}$$

$a_3 = -1$

$b_0 = m_1^3 + m_2^3 + m_3^3 - 6m_1m_2m_3V$

$b_1 = -3(m_1^2 + m_2^2 + m_3^2)$

$b_2 = 3$, and

$b_3 = -2$

In the third and fourth region, the roots of the cubic polynomial $P(\beta)$ are found such that:

1. $P(\pm\infty) = \mp\infty$, and
2. for a given V, the middle root of the three real roots of $P(\beta)$ is the proper root.

The process of interface reconstruction is accomplished in the following steps:

(a) Traversing from leaf to root, for each non-leaf computational cell, the volume fraction is set as the average of the children's volume fraction.

(b) Next, for each cell containing the interface, the stencil volume fraction, $f_{i,j,k}$ is populated with the volume fraction of a (virtual) cell of size $\triangle$, centered at $x_{i,j,k}$ and entirely contained in the smallest cell of size larger than or equal to $\triangle$ containing $x_{i,j,k}$. Once this is done, $\mathbf{m}$ is calculated using $f_{i,j,k}$ and MYC scheme. This is followed by the the computation of β. β and $\mathbf{m}$ are then stored as state variables. A more detailed description of interface reconstruction technique is given by Popinet (2009).

3.3.2 Interface Advection and Flux Computation

Once the interface is reconstructed, the next step is to calculate the volume fraction advection and volume fluxes. The numerical scheme used during the current research

endeavour is demonstrated for a single 2D computational cell below:

$$f^*_{i,j} = f^{n-1/2}_{i,j} V^{n-1/2}_{i,j} + \Phi^{n-1/2}_{i-1/2,j} - \Phi^{n-1/2}_{i+1/2,j} f^{n+1/2}_{i,j} V^{n+1/2}_{i,j} = f^*_{i,j} V^*_{i,j} + \Phi^*_{i,j-1/2} - \Phi^*_{i,j+1/2} \tag{3.39}$$

where $V_{i,j}$ is the effective volume of the cell and $\Phi_{i+1/2,j}$ is the volume flux of the first fluid through the right boundary of the computational cell. $V_{i,j}$ is defined by using the reduction and increase of the cell volume due to the one-dimensional velocity field, given by:

$$V^*_{i,j} \equiv V^{n-1/2}_{i,j} + \left(u^n_{i-1/2,j} - u^n_{i+1/2,j}\right) \triangle\triangle t V^{n+1/2}_{i,j} \equiv V^*_{i,j} + \left(u^n_{i,j-1/2} - u^n_{i,j+1/2}\right) \triangle\triangle t \tag{3.40}$$

The volume flux, Φ can be calculated using the geometrically reconstructed interface. Two kinds of situations are encountered for the octree spatial discretization used in the current research:

1. Flux calculation for cells of the same size: This is illustrated in Figure 3.4. The total volume fluxed from cell A to cell B is demarcated by the dashed line. The first fluid is marked by the dark triangle. Basically the area of the triangle is an estimate of of the volume flux $\Phi_{i+1/2,j}$ which can be easily calculated. This method might be more tricky and difficult to adapt for general grid systems but for the current spatial discretization, it is quite simple to implement.

2. Flux calculation for cells of different sizes: This is shown in Figure 3.5. Here cell A is a coarse cell while cells B and C are one size finer. The flux is calculated separately from the top and bottom halves of the coarse cell A shown in the figure by A and A' respectively. The equation for the interface is determined independently for the two halves. Once this is done, a procedure similar to the above is followed to calculate the volume fluxes.

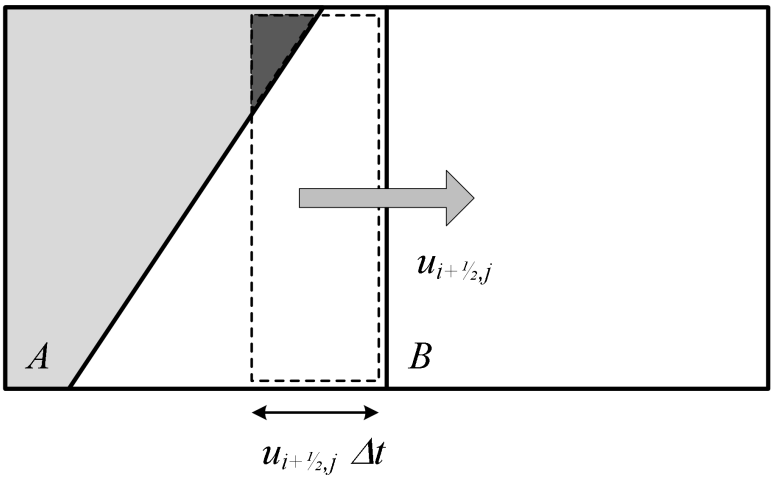

Figure 3.4. Geometrical flux estimation for computational cells of the same size.

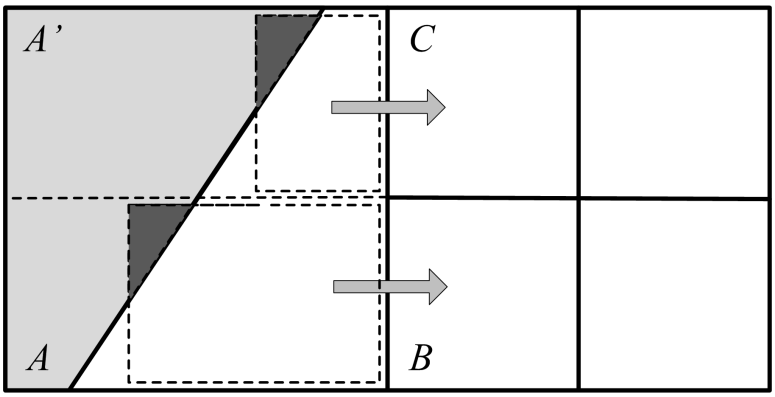

Figure 3.5. Geometrical flux estimation for computational cells of different sizes.

3.4 Time Step Constraints

The various numerical schemes used for the spatial discretization of the governing equations impose restrictions on the maximum allowable time step that can be used to ensure numerical stability. These constraints are determined by the convective, viscous and surface tension terms.

1. Convective terms: The constraint imposed by the convective term is probably the most well known constraint and is defined by the Courant Friedrichs Lewy (CFL) condition given by:

$$max\left[\frac{|\mathbf{u}_{i,j,k}|\triangle t_{ad}}{\triangle}\right] < CFL_{max} \tag{3.41}$$

   This restriction ensures that the fluid volume convected to the neighboring cell is not more than the amount of fluid in the cell. We use a conservative value of 0.5 for CFL number during our simulations to ensure consistency and stability.

2. Surface tension terms: The stability condition for the explicit treatment of surface tension is restricted by the appropriate time step resolution of the capillary waves and is given by (Brackbill *et al.*, 1992):

$$\frac{c_\phi \triangle t_{st}}{\triangle} < \frac{1}{2} \tag{3.42}$$

   where c_ϕ is the capillary wave phase velocity:

$$c_\phi = \sqrt{\frac{\sigma\widetilde{\nu}}{\rho_1 + \rho_2}} \tag{3.43}$$

   Similar to the restrictions imposed by convective terms, we use a conservative value of 0.5 in Equation 3.42. This ensures that two opposite moving capillary waves do not enter the same cell from opposite directions. The phase velocity of a capillary wave (eq. 3.43) traveling on the interface depends on the density of the two fluids on either side of the interface, surface tension and wave number.

The maximum allowable time step can be found by estimating the maximum phase velocity. The capillary phase velocity in turn depends on the maximum value of the wave number, $\widetilde{\nu}_{max} = \pi/\triangle$, corresponding the minimum grid resolution ($2\triangle$) required to resolve the wavelength. If these values are substituted in Equation 3.42, we get:

$$\triangle t_{st} = \sqrt{\frac{\rho_1 + \rho_2}{4\pi\sigma}\triangle^3} \tag{3.44}$$

Equation 3.44 can impose severe time step restrictions when surface tension is treated explicitly, which was the case in the current research. One of the ways to mitigate this is to use implicit schemes.

3. Viscous terms: The time step restriction imposed by the viscous terms is given by:

$$\triangle t_{vis} = min\left[\frac{\rho_{i,j,k}}{\mu_{i,j,k}}\frac{\triangle^2}{6}\right] \tag{3.45}$$

The time step chosen at a given instant is given by the minimum of the three values:

$$\triangle t = min\left(\triangle t_{ad}, \triangle t_{st}, \triangle t_{vis}\right) \tag{3.46}$$

3.5 Adaptive Mesh Refinement

One of the advantages of using a tree-based discretization, such as the one used for the current research is that, it is relatively simple to implement a flexible adaptive mesh refinement strategy. The mesh can be refined or coarsened depending on the criteria set to explore the particular physics under consideration as explained in Section 2.3.1. AMR implemented here is a two step process. In the first step, all the leaf cells satisfying the refinement criteria are updated (made finer). This is followed by coarsening of parent cells (of the leaf cells which were just refined) who do not satisfy the refinement criteria. Once the refinement/coarsening is complete the cell centered values of state variables have to initialized in the new cells. For the coarse

cells, it is easy to preserve quantities such as momentum - the cell centered values are computed by taking the volume average of their child cells. For the fine cells, this is a little more complicated. The value of state variables are initialized by linearly interpolating the parent cell values and their gradients. For a given child cell $\mathcal{C}$ with a parent $\mathcal{P}$, the initial value of any state variable, Ψ is given by:

$$\Psi(\mathcal{C}) = \Psi(\mathcal{P}) + \nabla_x \nabla_x \Psi(\mathcal{P}) + \nabla_y \nabla_y \Psi(\mathcal{P}) + \nabla_z \nabla_z \Psi(\mathcal{P}) \tag{3.47}$$

where $(\nabla_x, \nabla_y, \nabla_z)$ are the coordinates of the center of $\mathcal{C}$ relative to the center of $\mathcal{P}$. In general momentum and vorticity needs to be preserved when initializing the new cells. Equation 3.47 ensures local momentum conservation but some numerical noise is created in the voriticity. This issue can be resolved by using higher-order interpolation schemes.

3.6 Validation and Verification

Gerris has been validated by several researchers for a variety of flow conditions. Numerous validation cases were conducted by Popinet (2009) for surface tension driven interfacial flows. Some of these cases, especially relevant to the present research are: (1) second order convergence in case of stationary and moving droplet to the exact solution of Laplace's problem, (2) small-amplitude damped oscillations of a capillary wave with fluid of different densities, including high density ratio air-water systems, showing excellent agreement with theoretical results of Prosperetti (1981), and (3) three-dimensional capillary breakup of liquid jet showing excellent agreement with the theoretical analysis of Rayleigh (1892). Figure 3.6 shows the schematic diagram of the numerical setup for the current research problem. Physically, a single liquid droplet is impulsively started in a quiescent gaseous atmosphere. The spherical droplet deforms due to the action of aerodynamic forces and eventually breaks up. The deformation and fragmentation is resisted by the surface tension and viscous forces. As pointed out by researchers in the past, the magnitude of the inertial to surface tension force,

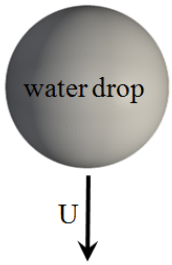

Figure 3.6. Computational setup. (Water droplet is given an initial velocity and the droplet structure and flowfield is tracked in time.)

i.e., the Weber number dictates the breakup mechanism (Krzeczkowski, 1980; Arcoumanis *et al.*, 1994; Faeth *et al.*, 1995; Arcoumanis *et al.*, 1996; Faeth, 1996, 2002). The dependence of We and Re on diameter and velocity at 1 and 100 atm is shown in Figures 3.7 and 3.8. Even though numerous experiments have been conducted over the last two decades to explore the breakup physics, no experimental investigation has been successful in measuring the local drop and ambient flowfiled that leads to the deformation and breakup of the droplets (Lopez-Rivera, 2010). This is primarily because droplet deformation and breakup process is truly a multiscale problem involving a wide range of time and length scales, in addition to the accelerating and unsteady nature of the problem. In the present work these length and time scales associated with droplet deformation and breakup phenomena are resolved to explain the breakup behavior quantitatively.

Before we begin the discussion of detailed flowfield and structure dynamics of the various breakup mechanisms, let us define our terminology since a lot of different terms have been used in the literature to describe different breakup modes. Oscillatory breakup - this has a fairly universal definition in the literature. We define it as a breakup process where the droplet oscillates, forming different shapes and eventually breaking up into relatively larger secondary droplets. Bag breakup - we identify this mode as the one with a bag or dome (inwards or outwards) structure and breakup initiation at the bag. Multimode breakup - this mechanism is identified with a stem

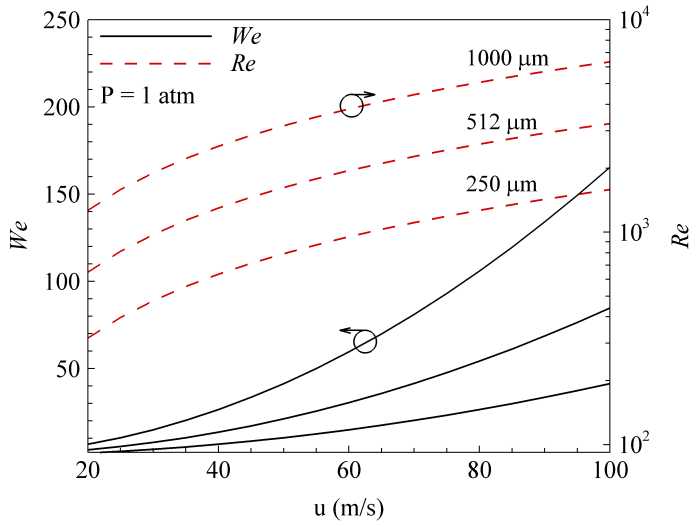

Figure 3.7. Dependence of diameter and velocity on Weber and Reynolds number at 1 atm.

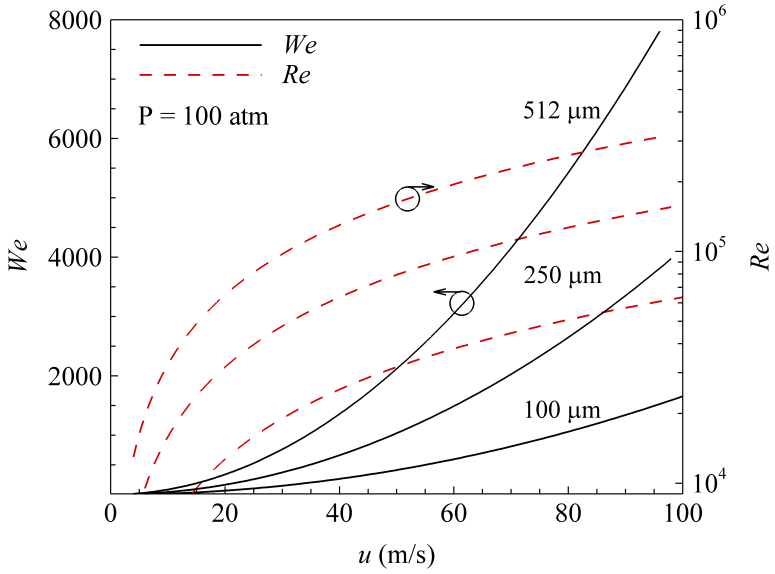

Figure 3.8. Dependence of diameter and velocity on Weber and Reynolds number at 100 atm.

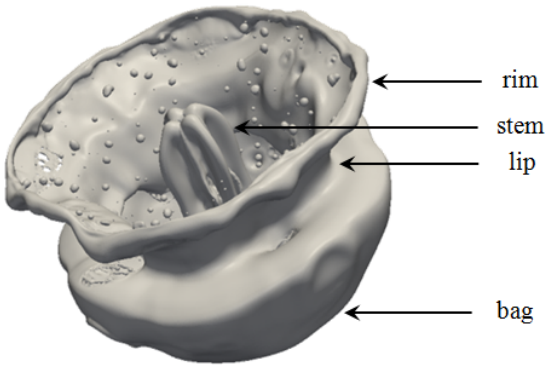

Figure 3.9. Figure showing the definitions of bag, lip, rim and stem.

protruding from the bag. Shear breakup - in our definition, sheet thinning and wave travelling breakup mechanisms fall in this category. The generalized regime diagram discussed later in Section 4.5 is based on these definitions. Several other terms, such as bag, lip, stem and rim will be used while discussing the droplet breakup phenomena. These are defined in Figure 3.9.

As a first step, we compare our simulation results with those of Han & Tryggvason (2001) owing to the similarity in configuration and comparable Weber number and density ratio. As shown in Figure 3.10, the current approach shows excellent agreement with results obtained by Han & Tryggvason (2001). We are capable of capturing the various shapes involved in the breakup process, including the bowl and backward facing droplet structure. It should be noted that results of Han & Tryggvason (2001) were obtained from an axisymmetric calculation where breakup of the droplet was not considered. Current results were obtained from a 3-D calculation with breakup.

Irrespective of the numerical method, challenges accompanying numerical simulation of incompressible two-phase systems increase multiple folds as the density ratio increases (Gorokhovski & Herrmann, 2008; Desjardins & Moureau, 2010). At this point, it should also be highlighted that standard V-cycle multigrid methods often exhibit extremely slow convergence rates in case of elliptic equations with discontinuous/stiff coefficients and source terms (Alcouffe *et al.*, 1981; Chan & Wan, 2000),

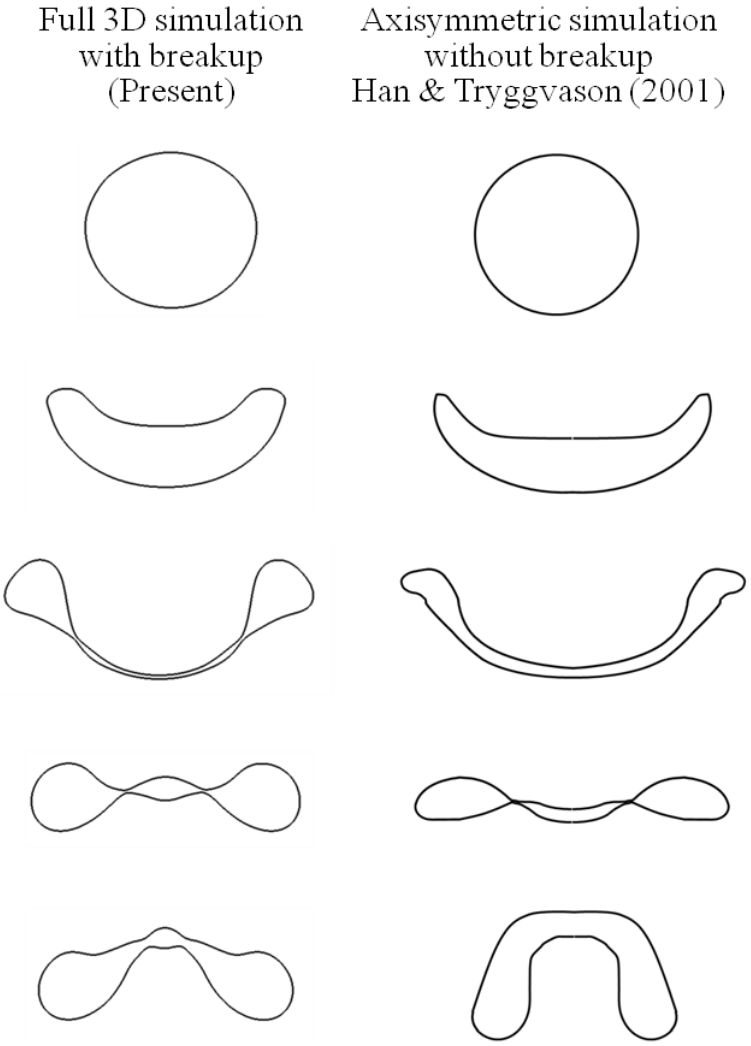

Figure 3.10. Comparison of present results (left) for $We = 24$, $\rho_l/\rho_g = 8.29$ with results from Han & Tryggvason (2001) (right) for $We = 18.7$, $\rho_l/\rho_g = 10$.

which is certainly the case for liquid/gas systems at low pressures. Time integration scheme used in the current approach involves a classical time-splitting projection method which requires the solution of the Poisson equation to get the pressure field:

$$\nabla . \left[\frac{\triangle t}{\rho_{n+1/2}} \nabla p_{n+1/2} \right] = \nabla . u_* \tag{3.48}$$

As mentioned before, equation 3.48 is solved using a standard multigrid V-cycle methodology and as a result, for large density ratio flows the above equation suffers from slow convergence rates. Extremely high grid resolution is required to resolve the large density gradients, surface tension at the interface and to ensure consistencies in the momentum equation. Even though the current methodology performs very well for several high density ratio systems, such as travelling capillary wave in an air/water system as shown by Popinet (2009), in comparison with other methods in the literature as presented by Gerlach *et al.* (2006), the convergence for high density ratio cases (usually due to low pressure conditions) can seriously degrade depending on the problem and interface topology (Popinet, 2009). Droplet breakup phenomenon at large density ratios is one such case. Obtaining accurate results for such a configuration requires very high grid resolution which quickly makes the numerical simulations cost prohibitive. For example, we show results for a water droplet in air environment which corresponds to shear breakup phenomenology at 1 atm pressure conditions. The diameter of the water droplet used for this case was 750 μm with an initial velocity of 95 m/s. The corresponding Weber and Reynolds numbers were 112 and 4518 respectively. The density ratio was 829. As seen in Figure 3.11, our numerical results capture the current understanding of shear breakup in the literature, i.e., the droplet breaks up via sheet thinning at the surface. Moreover, we also observe a wave moving on the surface of the droplet which was not observed very clearly in experiments because of the dense cloud of droplets surrounding the parent drop. This wave is eminent in the current setup because of the existence of Rayleigh-Taylor instability due to sudden acceleration of the droplet. We shall explain the shear breakup phenomena

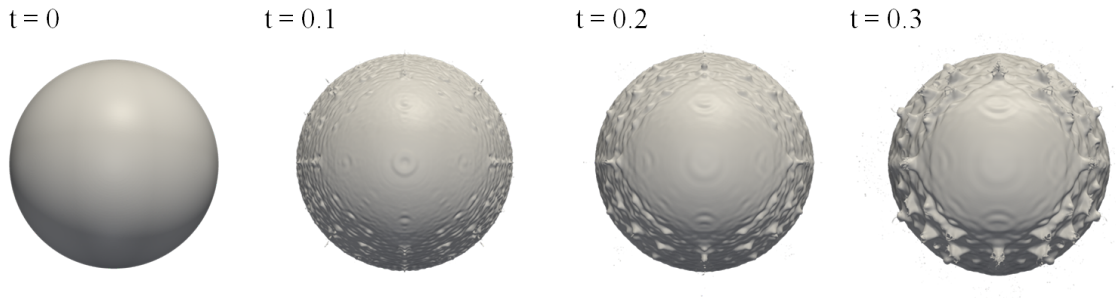

Figure 3.11. Shear breakup - We = 112, Re = 4518, ρ_l/ρ_g = 829. Temporal evolutions of 3D droplet structure (bottom view) in non-dimensional time. Droplet iso-surface in grey at various times. Non-dimensional time, t = T*U/D.

in detail later in the results section. The minimum grid size used for this calculation to obtain acceptable results was $1/2^{12}$ D ($0.18\mu m$), and it took about 52000 CPU hours to obtain the results shown in Figure 3.11 on a AMD Opteron 8431, 2.4 GHz, 64 GB, hexa-core, quad processor computing cluster. This computing resource was just enough to identify the type of breakup for this case. The computing cost becomes enormous if child droplet statistics such as final droplet size distribution are of interest.

In this thesis, we develop a regime diagram valid for a wide range of pressure conditions to identify the breakup types at a given operating condition. Correlations for child droplet statistics at lower density ratios are developed. The generalized regime diagram can then be used in conjunction with these correlations to predict child droplet statistics at other pressure conditions. We demonstrate this by comparing the sauter mean diameter for shear breakup regime predicted by experimental correlations with our SMD correlation in combination with the generalized regime diagram in the last section. As will be seen later, our correlation shows excellent agreement with experimental data for shear breakup regime, which further validates our approach. In Section 4.3, we also compare our bag breakup results with that of Sehgal *et al.* (1999), showing excellent qualitative agreement.

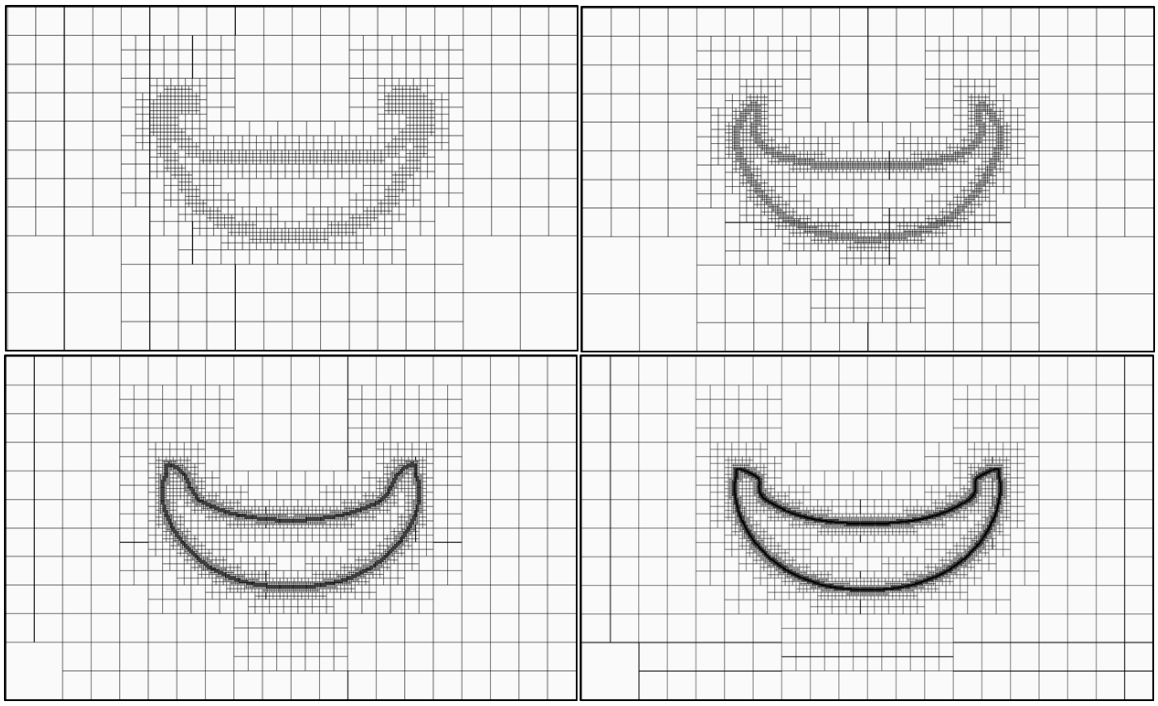

Figure 3.12. Grid sensitivity analysis using 8, 9, 10 and 11 cell levels at 2.5 μs.

Grid sensitivity analysis was also performed to identify the optimum grid resolution to resolve the various length scales involved in the droplet deformation and breakup process. For example, the grid sensitivity analysis was performed using a 100 μm water droplet with an initial velocity of 22 m/s. The corresponding Weber and Reynolds numbers were 80 and 13951 respectively. Cell levels of 8, 9 10 and 11 were used for the analysis. Figure 3.12 shows the AMR grid for the cell levels mentioned before at 2.5 μs during the temporal evolution of the droplet. It can be clearly seen that the interface resolution corresponding to the cell level of 10 is identical to that of 11. Cell levels of 8 and 9 cannot resolve the droplet shape properly. Similar studies were performed for other Weber numbers to identify the optimum grid resolution. For all the cases conducted during the current research, the maximum grid level ranges from 10-12 (in general, higher level for higher Weber number).

3.7 Closing Remarks

This chapter details the numerical schemes used to discretize the various terms in the equations governing the dynamics of liquid droplets. Time integration and spatial discretization of advection, viscous and surface tension terms are discussed followed by the the VOF advection scheme. Time step constraints and AMR are examined next. Validation and verification of the current approach is presented in the last section. Results are compared with those presented in the literature, showing excellent agreement.

CHAPTER IV

BREAKUP AND DYNAMICS OF NEWTONIAN LIQUID DROPLETS

4.1 General Overview and Literature Survey

Liquid droplet deformation and breakup resulting from primary atomization, in the presence of a relative fluid velocity, has been a matter of serious practical concern in a wide range of applications, including, but not limited to, dense spray combustion (Faeth, 1996, 2002), industrial and agricultural sprays, gas-liquid separators and two-phase flows in chemical reactors. In the particular case of liquid-fueled propulsion systems, such as diesel, gas-turbine and rocket engines, the system performance is conditioned by the fuel and oxidizer droplet size distribution and is usually the rate-controlling process (Faeth, 2002; Berthoumieu *et al.*, 1999). Droplet vaporization and ensuing combustion is accelerated if the droplet size is smaller, which makes any process leading to a reduction in drop size of prime importance in the combustion system design. In dense sprays, mixing of fuel and oxidizer is controlled by the droplet size, which is a direct consequence of the droplet breakup process (Faeth, 1996; Faeth *et al.*, 1995; Ruff *et al.*, 1992). In this chapter, we focus on exploring the fundamental processes underlying liquid droplet breakup. We also develop correlations based on first principles dictating the child droplet diameter distribution, and a generalized regime diagram to predict droplet breakup mechanism over a broad range of operating conditions.

Several reviews on droplet deformation and breakup were conducted in the past (Giffen & Muraszew, 1953; Hinze, 1955; Levich, 1962; Pilch & Erdman, 1987; Lefebvre, 1988; Wierzba & Takayama, 1988; Faeth *et al.*, 1995; Faeth, 2002; Gefland, 1996;

Clift *et al.*, 2005; Guildenbecher *et al.*, 2009). Based on the Weber number, droplet breakup has often been classified into breakup modes by researchers, over the last six decades (Hinze, 1955; Krzeczkowski, 1980; Pilch & Erdman, 1987; Hsiang & Faeth, 1992, 1995). The various breakup regimes identified by Hsiang & Faeth (1995) at atmospheric pressure for a variety of fluids are shown in Figure 4.1 for density ratios greater than 500. The figure shows oscillatory, bag, multimode, shear and piercing regimes with respective critical Weber numbers at 1 atm. It is quite clear from the figure that the breakup mechanism is dependent only on We for operating conditions where $Oh < 0.1$. Table 4.1 shows the diameters for various fluids corresponding to $Oh = 0.1$ along with the fluid properties (Hsiang & Faeth, 1995) used in the calculation. By definition, for a given fluid, the Ohnesorge number decreases with increasing droplet diameter. Figure 4.1 also shows the variation of Ohnesorge number (which is independent of velocity) as the droplet diameter changes, for various fluids. The black square symbol, with the x-coordinate of $Oh = 0.1$, corresponds to a water droplet of diameter 0.86 μm, which is smaller than droplet sizes encountered in most practical applications of interest. The operating conditions considered in this research in parameter space are shown by the shaded portion of 4.1, and corresponds to $Oh < 0.1$. As a consequence, for the current study, the most important non-dimensional parameter dictating the droplet breakup physics is the Weber number. Another research area which has not been explored in the past is the effect of pressure on droplet disintegration. In this chapter we will study the breakup process at a broad range of pressure conditions and quantify the critical Weber numbers at various pressures in the form of a generalized regime diagram.

As a droplet moves with a velocity relative to the ambient, it is acted upon by aerodynamic drag force. The drag force, in turn, creates differential pressure distribution around the droplet and causes it to deform. The other forces acting on the droplet are the surface tension force and the internal and external skin friction force due to the

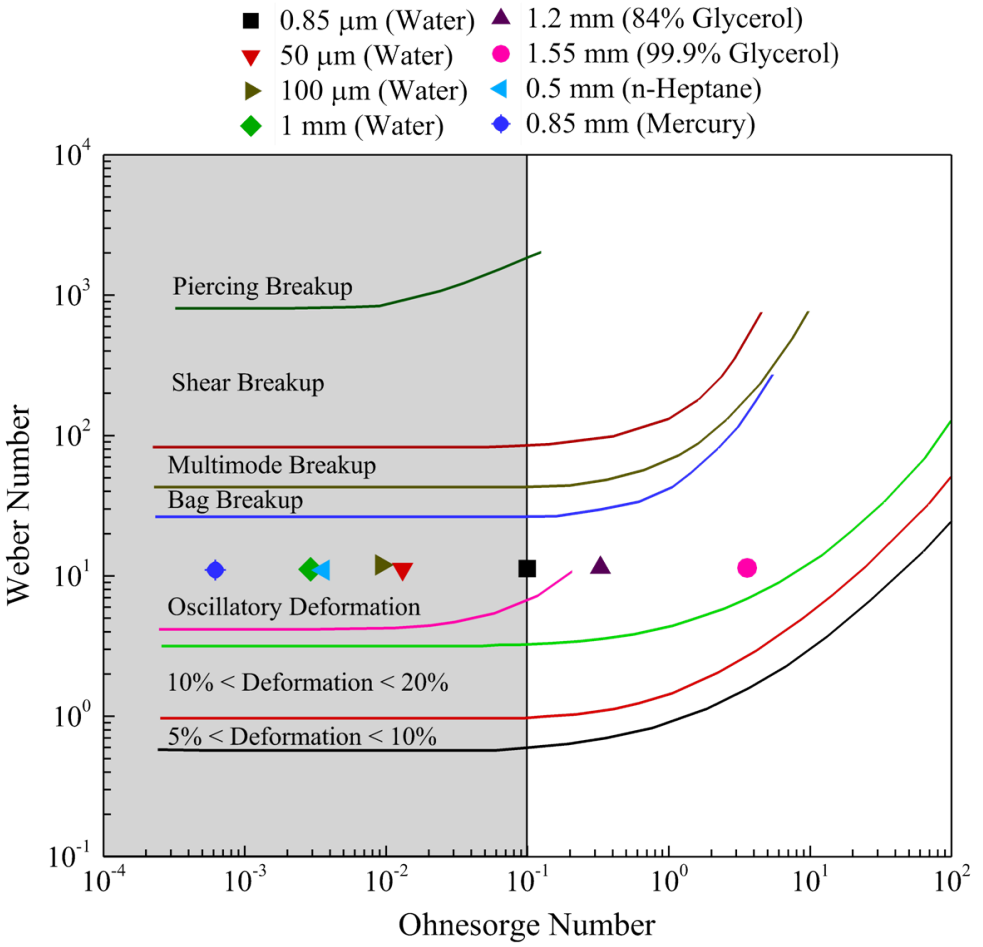

Figure 4.1. Breakup regime diagram at 1 atm and 298K. Variation of Oh for a fixed $We = 11$ with change in diameter (symbols show the variation of Oh number with diameter) (Hsiang & Faeth, 1995; Chou *et al.*, 1997).

Table 4.1. Droplet diameter for various liquids corresponding to $Oh = 0.1$.

Fluid	Density (kg/m^3)	Viscosity $\times 10^4$ $(kg/m-s)$	Surface tension $\times 10^3$ (N/m)	Diameter (μm)
Water	1000	7.89	72.8	0.86
n-Heptane	683	3.94	20.0	1.14
Mercury	13600	15	475.0	0.034
Glycerol 21%	1050	16	67.3	3.62
Glycerol 63%	1162	108	64.8	154.91

droplet and gas viscosity. These forces acting on the droplet can be associated with multiple time and length scales governing the droplet breakup phenomena. Table 4.2 shows the various time scales of interest. The convective time scale, τ_c, is dictated by the parent droplet diameter and velocity, irrespective of the fluid, and represents the time which the droplet spends in the region of interest. A more non-intuitive and interesting time scale is the deformation response time, τ_r, which is dependent on the physical properties of the droplet. It can be defined as the time required for the droplet to assemble its "resources" to resist the change in shape due to externally imposed forces. For example, if the droplet is made of a non-deformable substance, i.e., $\sigma \to \infty$, then by definition $\tau_r \to 0$, which means that the droplet instantaneously responds to the external force that it will not undergo deformation. On the other hand if a liquid droplet is subject to supercritical conditions, where $\sigma \to 0$ so that $\tau_r \to \infty$, suggesting that the droplet will never respond to a force trying to deform it. This makes physical sense because surface tension seizes to exist at supercritical conditions and there is no physical interface in the conventional sense to deform. The transport or the viscous time scales, $\tau_{v,l}$ and $\tau_{v,g}$, represents the time required for the

Table 4.2. Time scales.

Time Scale	Definition	Remarks
Convective time	$\tau_c = D/U$	
Deformation response time	$\tau_r = \sqrt{\frac{\rho_l D^3}{\sigma}}$	$\tau_r^2 = We\frac{\rho_l}{\rho_g}\tau_c^2$
Transport time (gas)	$\tau_{v,g} = \frac{D^2}{\nu_g}$	$\tau_{r,g}^2 = \frac{We}{Re^2}\frac{\rho_l}{\rho_g}\tau_{v,g}^2$
Transport time (liquid)	$\tau_{v,l} = \frac{D^2}{\nu_l}$	$\tau_{r,l}^2 = \frac{We}{Re^2}\frac{\rho_l}{\rho_g}\frac{\nu_l^2}{\nu_g^2}\tau_{v,l}^2$

viscous forces to come into effect during the whole process. The length scales include the various curvatures formed during the deformation process, as well as the myriads of different sized ligaments and child droplets produced during and after the breakup process. As an example, for a water droplet of 100 μm with an initial velocity of 50 m/s, the time scales vary from 2 μs to 625 μs corresponding to the convective, τ_c, and transport (gas), $\tau_{v,g}$, times scales. The presence of disparate length and time scales, along with the complex physics, makes this a formidable problem, theoretically, experimentally and computationally.

Depending on the magnitude of the inertial force in comparison with the restoring surface tension force, the droplet breaks up via oscillatory, bag, multimode or shear breakup mechanism. Figure 4.2 shows the various breakup modes observed by researchers for Newtonian droplets exposed to subsonic and supersonic air streams (Gel'fand *et al.*, 1974; Krzeczkowski, 1980; Borisov *et al.*, 1981; Arcoumanis *et al.*, 1994; Berthoumieu *et al.*, 1999; Theofanous *et al.*, 2004; Miller *et al.*, 2007).

A few studies on highly viscous and non-Newtonian droplet breakup under the action of an air jet have also been reported (Arcoumanis *et al.*, 1994, 1996; Joseph

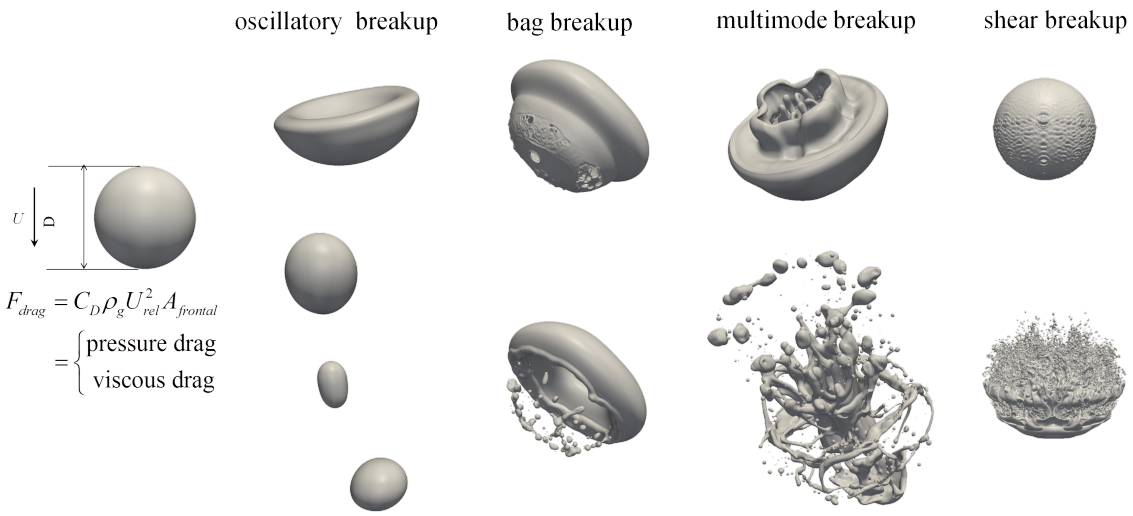

Figure 4.2. Various droplet breakup mechanisms observed by researchers for Newtonian liquids.

et al., 1999; Lopez-Rivera & Sojka, 2009; Lopez-Rivera, 2010). Krzeczkowski (1980) conducted experimental investigations to understand deformation mechanisms and droplet lifetimes for different fluids by examining disintegration of falling droplets in a wind tunnel. The density ratio was kept constant by the choice of liquids considered. It was concluded that the mechanism and duration of droplet deformation and breakup is a strong function of Weber number. Similar experiments were conducted by Arcoumanis *et al.* (1994) using high speed photography and pulsed laser illumination to study the breakup of Newtonian and viscoelastic non-Newtonian liquid droplets falling under gravity in a cross air stream. The droplet diameters ranged from 2.4 to 3.3 mm with air jet velocities ranging up to 360 m/s (Arcoumanis *et al.*, 1994, 1996). Three distinct breakup modes, bag and stamen, stripping, and chaotic, were identified and categorized based on the Weber number. Following this, three kinds of non-Newtonian fluid droplets were tested. Photographic evidence revealed that non-Newtonian droplets undergo stretching and shear stripping where fluid ligaments are shed from the droplet as the droplet falls in the air stream. It was also found that as the concentration of the thickening agent is increased, the total breakup time

increases. Theofanous *et al.* (2004) also conducted experiments on viscous droplets under the action of supersonic rarefied air streams. The experimental conditions consisted of droplet diameters between 3.5-4.5 mm and air flow speed up to Mach 3 with the gas density varying between 5×10^4 and $0.1 kg/m^3$. Similar to other experiments, four different breakup regimes were identified for TBP while for Glycerin, only three regimes were observed owing to its high viscosity. Recently, Lopez-Rivera (Lopez-Rivera & Sojka, 2009; Lopez-Rivera, 2010) conducted experiments to study non-Newtonian droplet breakup morphology. Six different solutions of CMC in water were used to study the effect of liquid rheology on the breakup process. The droplet diameter ranged from 2.2-2.8 mm. Bag and multimode breakup regimes were observed with extended bag sizes and persistent ligaments. Various breakup times were reported and correlated with Weber and Ohnesorge numbers. The TAB droplet breakup model (O'Rourke & Amsden, 1987) was modified to include inelastic non-Newtonian power law liquids and the modified TAB model was used to compare breakup times with the experimental data.

In addition to experiments listed before, extensive shock tube experiments have also been conducted to study the breakup characteristics of single droplets due to the flow behind the disturbance created by a travelling shock wave (Ranger & Nicholls, 1968; Krauss & Leadon, 1971; Gel'fand *et al.*, 1974; Boiko *et al.*, 1987; Hsiang & Faeth, 1992, 1993; Faeth *et al.*, 1995; Hsiang & Faeth, 1995; Chou *et al.*, 1997; Chou & Faeth, 1998; Joseph *et al.*, 1999; Dai & Faeth, 2001). Hsiang & Faeth (Hsiang & Faeth, 1992, 1993, 1995) studied the effect of steady and shock wave initiated disturbances on droplet breakup using pulsed shadowgraphy. The driven section of the shock tube had a length of 6.7 m with a rectangular cross section (38 mm wide $\times$ 64 mm high). The test location was 4.0 m from the downstream end. This provided test times of 17-21 ms in the uniform flow region behind the incident shock wave. The initial droplet size varied from 150-1550 μm. Quite a few liquids were studied covering a range of

initial conditions varying in the following range of non-dimensional numbers: We: 0.5-1000, Oh: 0.0006-4; ρ_l/ρ_g : 580-12000, and Re: 300-16000. Droplet deformation and breakup regime map was developed along with correlations for breakup times, droplet drag, size and velocities after breakup. These studies were followed by more detailed experiments by Chou *et al.* (Chou *et al.*, 1997; Chou & Faeth, 1998) and Dai & Faeth (2001) to investigate the temporal properties of the bag, shear and multimode breakup regimes, respectively. Temporal distributions of droplet size and velocities at various stages of the breakup process for bag and multimode breakup modes were observed and analyzed using simplified theories.

In contrast to experimental studies, limited literature exists on numerical investigations of droplet breakup phenomena. Han & Tryggvason (1999; 2001) conducted numerical simulations to study the effect of constant force and impulsive acceleration on droplet deformation, using a compressible, axisymmetric interface tracking technique. The work was limited to small density ratios of 1.15 and 10 and did not consider droplet breakup. The same problem was later simulated by Quan & Schmidt (2006) to examine droplet deformation and drag force induced by the deforming droplet using an incompressible, finite volume staggered mesh method coupled with a moving mesh interface tracing scheme. Similar axisymmetric calculations were conducted by Helenbrook & Edwards (2002) to study quasi steady deformation and drag of liquid droplets with density ratios between 5 and 500, viscosity ratios between 5 and 15, Weber numbers between 0.1 to 50, and Ohnesorge numbers between 10^4 and 10 using an arbitrary-Lagrangian-Eulerian unstructured mesh movement scheme. Correlations were developed to predict various droplet shapes and drag coefficient, taking into account the effect of internal circulation on aerodynamic drag. One of the few three-dimensional numerical simulations on single droplet breakup was conducted by Khosla *et al.* (2006). They conducted 3D and axisymmetric calculations using the volume-of-fluid (VOF) approach to study the breakup of a single liquid drop by gas

crossflow. Calculations were first conducted to simulate a water droplet in shock tube environment. It was concluded that shock interaction with the droplet did not have any effect on the droplet breakup process. Due to the immense computational expense, the rest of the simulations were conducted in an axisymmetric framework.

It is quite evident from the brief literature survey above that most of the experimental investigations on droplet breakup have been for $\rho_l/\rho_g > 500$ and $Oh < 0.1$ (Faeth, 1996). The numerical simulations, on the other hand, have been limited to low density ratios but, owing to the extreme computational burden, were formulated either with two-dimensional or axisymmetric assumption, which is not enough to explain the rich physics involved in this complex multi-phase phenomena. Moreover, from a purely fluid dynamics point of view, the underlying physics behind liquid droplet deformation and breakup is still elusive. This chapter will try to address several unanswered questions currently confronting the spray community. Unanswered questions include identification of breakup modes, quantitative description of fundamental processes underlying droplet breakup and generalized correlations for Newtonian liquid droplets over a broad range of operating conditions. In the present work we aim at answering the above questions by investigating the detailed flowfield and structure dynamics of liquid droplet breakup and extracting essential physics governing the breakup phenomena. Since limited literature exists for droplet breakup at higher pressures, during the present research effort, emphasis has been placed on droplet deformation and breakup at elevated pressures, which also represents typical pressure conditions inside a combustion chamber in a practical propulsion device. To isolate the hydrodynamic mechanisms dictating droplet breakup phenomena, evaporation is neglected, and simulations are performed at isothermal conditions. Since the breakup process is governed by non-dimensional parameters involving surface tension, σ, and viscosity, μ, property evaluation for numerical computations at room temperature and a range of operating pressures of interest is vital. Effect of pressure on

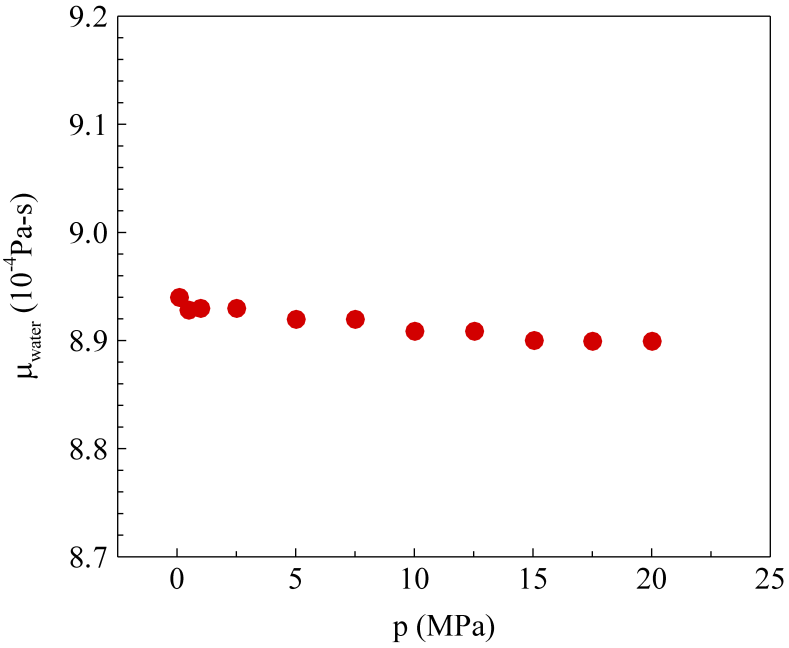

Figure 4.3. Viscosity of water as a function of pressure (Schmelzer *et al.*, 2005).

surface tension has already been discussed in Section 2.4 and is shown in Figure 2.3. The effect of pressure on the viscosity of water is not profound as seen in Figure 4.3 (Schmelzer *et al.*, 2005). In the present calculations, appropriate values of the surface tension and viscosity of water in the presence of air have been taken. The results in this chapter are based on Khare *et al.* (2011, 2012).

4.2 Oscillatory Breakup

This is the least violent of all the breakup modes. If a 100 μm water droplet is given an initial velocity of 12 m/s to achieve a $We = 24$, $Re = 7609$, at a density ratio of 8.29, oscillatory breakup is observed. Figure 4.4 shows the temporal evolution of events taking place during the oscillatory breakup of a droplet. The figure shows 3D iso-surface of the droplet on the top and streamlines and droplet surface contours on the bottom. As shown before, these results are in excellent agreement with the results obtained by (Han & Tryggvason, 2001) (refer Figure 3.10). In general, if the

aerodynamic forces are large enough, the droplet deforms until it breaks up following bag, multimode, shear breakup mechanism, otherwise, the droplet oscillates due to the restoring surface tension force and internal circulation (Karam & Bellinger, 1968). If the oscillations are unstable, the droplet breaks up into relatively larger fragments, which was the case during the present calculation. This observation is consistent with those made by previous researchers (Hsiang & Faeth, 1992; Han & Tryggvason, 2001; Lopez-Rivera, 2010).

In a nutshell, as the droplet starts to move in the ambient atmosphere, it first transforms into a bowl, followed by the inversion of the bowl forming a dome, and eventually breaks up into two child and a satellite droplet. The streamlines are first plotted in drop coordinate system as shown in Figure 4.4. The movement of the droplet in quiescent ambient creates two counter rotating vortices. Static pressure at the forward and rear stagnation points is higher than that at the sides, which is typical for flow over a sphere. This unequal static pressure distribution causes the droplet to deform laterally and forms a bowl with a lid. The droplet core velocity in the downward direction is much higher than the velocity at the edges. As a result the droplet edges are pushed in the direction opposite to the motion of the droplet, while overall the droplet is still moving downwards. This results in the formation of a bowl shape as opposed to a dome shape. If the droplet velocity and Reynolds number are small enough for a given Weber number, the droplet might deform to form a dome shaped structure as illustrated by (Hsiang & Faeth, 1995). Similar observations were made by Sehgal *et al.* (1999) for a density ratio of 1 using a Lattice-Boltzmann approach. The instantaneous Weber number associated with the moving droplet decreases owing to the reduction in the relative velocity of the droplet due to the action of drag force. As the instantaneous Weber number decreases, the fluid surface tension causes the droplet to oscillate and leads to the formation of a dome followed by the stretching of the droplet in the flow direction, after which, it eventually breaks,

first from the bottom, and then from the top, giving rise to two child and a satellite droplet. The breakup takes place via pinch-off, as result of shear stresses created by the retracting surface tension force which tries to minimize the surface area causing the liquid interface to recede and creating concentrated shear stresses at the point of breakup. As the droplet deforms, the velocity at different points inside the droplet is different and hence it becomes impossible to plot the results in a coordinate system fixed to the droplet, and so from here onwards, the results will be presented in fixed coordinate system as shown in the bottommost droplet iso-surface contours in Figure 4.4.

4.3 Bag and Multimode Breakup

Bag and multimode breakup mechanisms share several features, especially at the beginning of breakup process. Therefore, these two breakup modes are discussed together in this section. As the Weber number is increased beyond 30, the breakup mechanism changes. Temporal events taking place when a 50 μm water droplet is subjected to an initial velocity of 20 m/s are shown in Figure 4.5. This corresponds to a $We = 33$, $Re = 6342$ at a density ratio of 8.29. As in the case of oscillatory breakup, the droplet deforms due to unequal pressure distribution over the droplet periphery and flattens from the top. The flowfield associated with this breakup mechanism is analyzed by looking at the development of streamlines (in fixed coordinate system) and normalized gauge pressure contours as the droplet structure evolves. The gauge pressure is defined as $p_{gauge} = (p - p_{ambient})/\rho_g U^2$. Two counter rotating vortices are formed as the droplet starts moving. Since the droplet acts as a bluff body, it creates a wake as it moves downwards, thereby creating a high pressure region above the droplet. This leads to the formation of a thin bag/balloon structure. The bowl shaped structure formed in our simulations agrees well with the numerical simulations conducted by Han & Tryggvason (2001); Sehgal *et al.* (1999) at lower density ratios

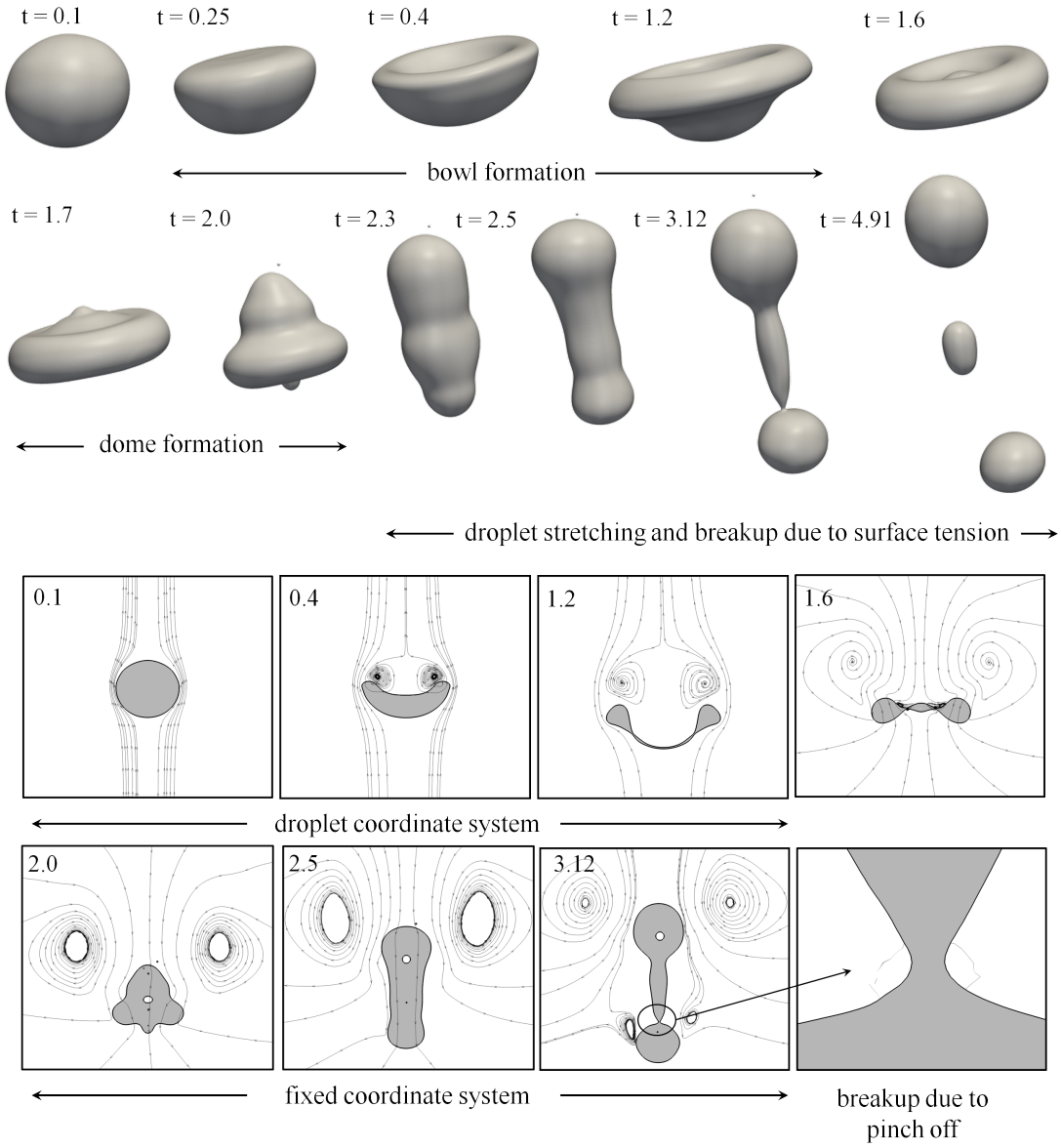

Figure 4.4. Oscillatory breakup - $We = 24$, $Re = 7609$, $\rho_l/\rho_g = 8.29$. Temporal evolutions of 3D droplet structure in non-dimensional time. Droplet iso-surface in 2D flooded in grey and streamlines at various times. Non-dimensional time, t = T*U/D. The first three contours show streamlines in drop coordinate system while the rest are in fixed coordinate system.

when the droplet was subjected to an impulsive acceleration. The formation of a bowl rather than a dome shape is also consistent with the observations and correlations presented by Hsiang & Faeth (1995). The bag keeps thinning due to higher pressure inside the bag as shown in Figure 4.5. As the droplet moves further into the ambient, the thinning of the bag causes the incompressible liquid to move towards the rim making it thicker than the bag. The bag, which is progressively becoming thinner, eventually cracks at multiple locations to form a web like structure. The breaking of the bag is caused due to the breakup of the thin film via capillary instability as shown in the zoomed plot in Figure 4.5. This event is followed by the breakup of the rim to form another set of child droplets. By the time the bag breaks up, the relative velocity between the droplet and the environment has decreased considerably and the instantaneous Weber number becomes very small. As a result, the rim breakup takes place via oscillatory breakup as discussed in the previous section. These results phenomenologically similar to those obtained by Sehgal *et al.* (1999) for bag breakup as shown in Figure 4.6 for a Weber number of 276 at a density ratio of 1.

One of the objectives of this work is to quantitatively identify the temporal locations of various events taking place during the breakup process. The droplet structure and shape is primarily determined by the surface tension force. Normalized surface energy, which is the product of overall surface area of the droplet and the surface tension, normalized by the initial value of surface energy, is calculated at each time step. Since the surface energy is normalized by its initial value, it starts at 1. Various events during the droplet lifetime can be predicted by analyzing the variation of normalized surface energy of the droplet. Figure 4.7 shows the time evolution of kinetic and surface energies associated with the droplet. As the droplet moves, the kinetic energy of the droplet decreases due to aerodynamic drag. Simultaneously, the surface energy increases due to droplet deformation which causes an increase in the effective surface area and hence the surface energy of the droplet. The location of

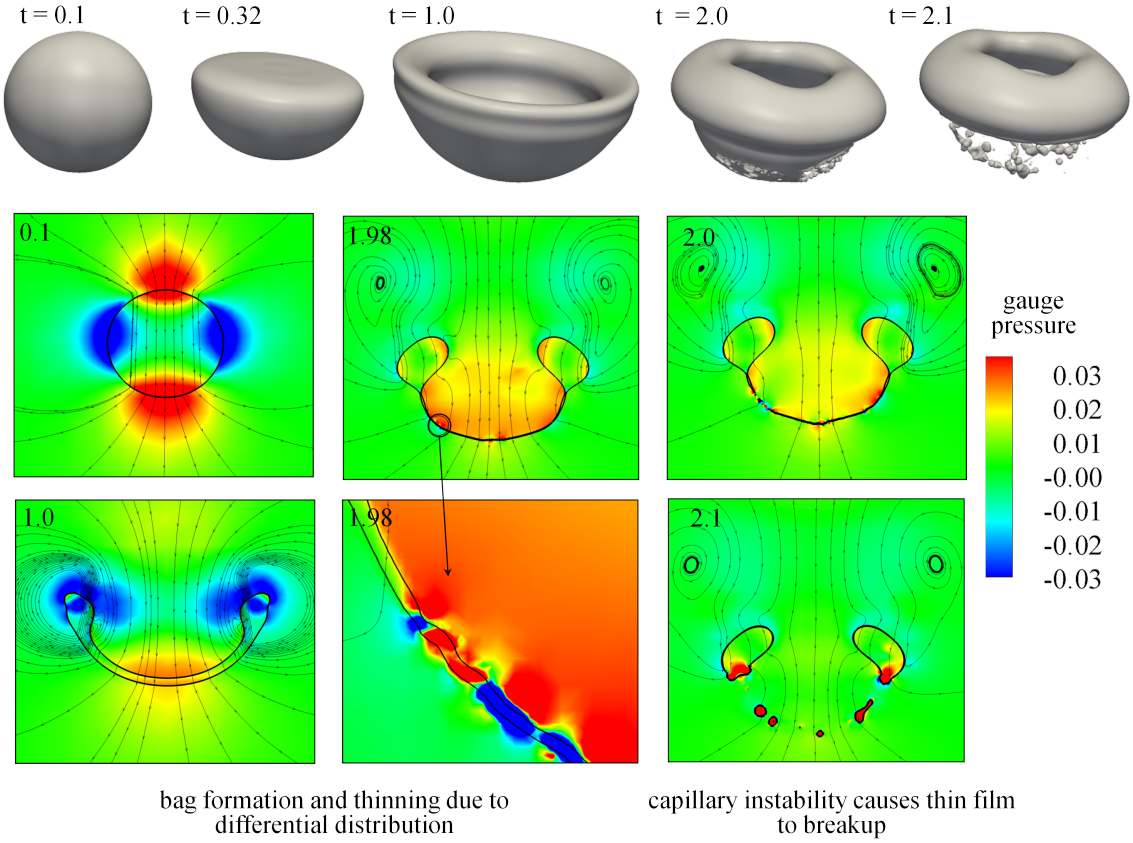

Figure 4.5. Bag breakup - $We = 33$, $Re = 6342$, $\rho_l/\rho_g = 8.29$. Temporal evolutions of 3D droplet structure in non-dimensional time. Droplet iso-surface in 2D, streamlines and normalized gauge pressure distribution in the droplet periphery at various times. Non-dimensional time, t = T*U/D.

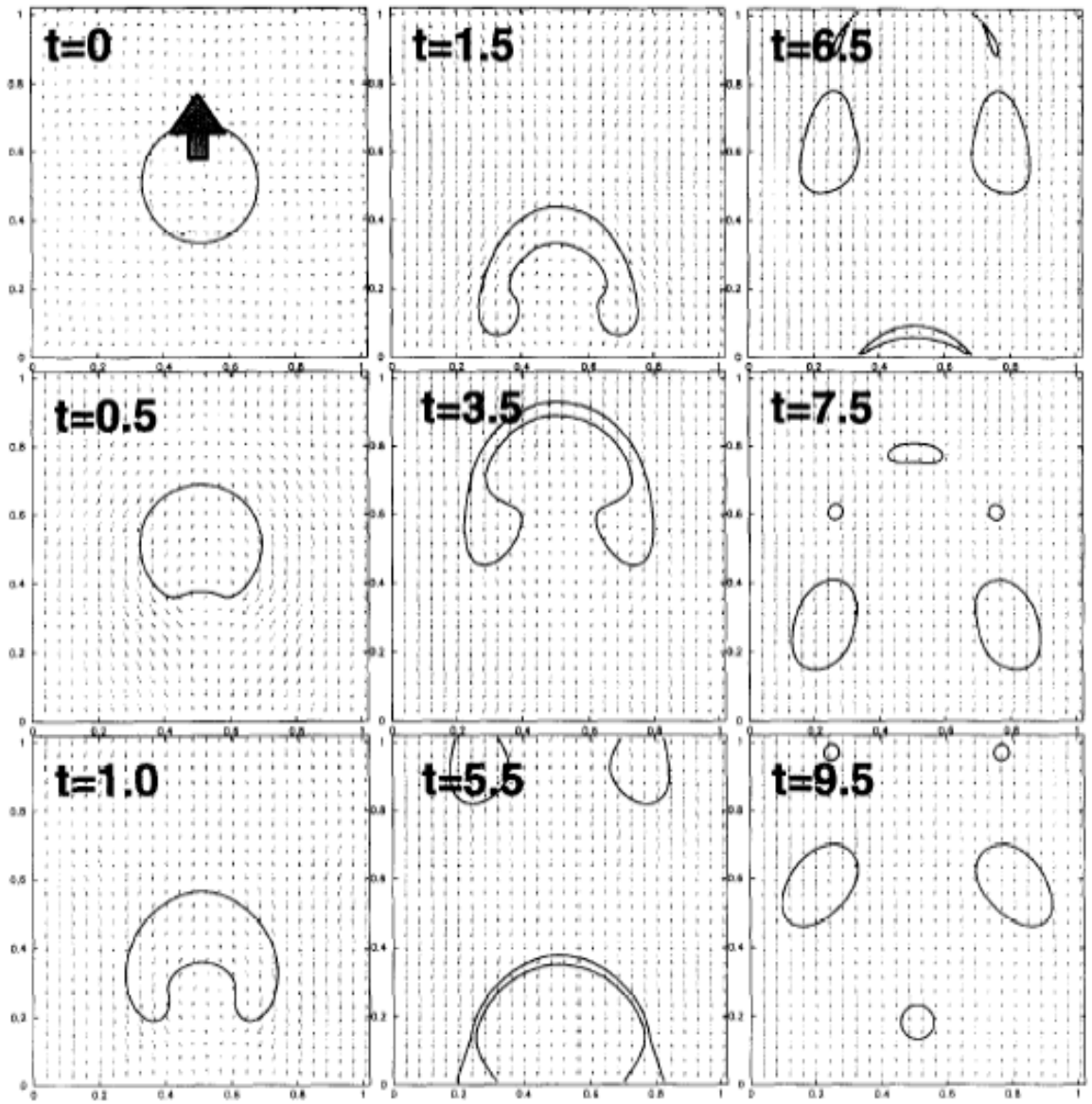

Figure 4.6. Bag breakup - $We = 276$, $Re = 113$, $\rho_l/\rho_g = 1$, $Oh = 0.15$. Temporal evolutions of 2D droplet structure (Sehgal *et al.*, 1999).

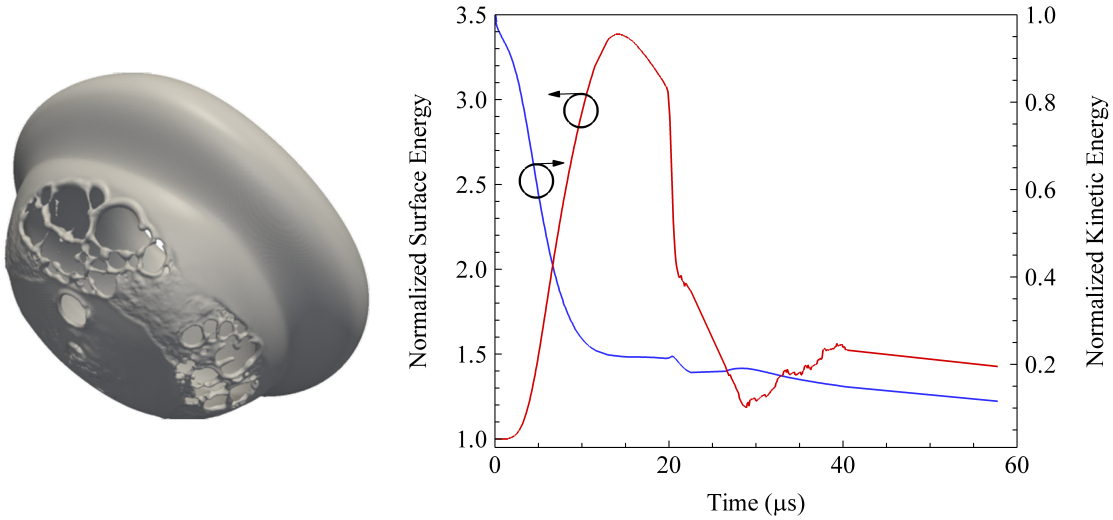

Figure 4.7. Evolution of surface energy of the droplet for the bag breakup regime. Breakup initiates at 20 μs.

the first point of breakup at 20 μs, as shown in Figure 4.7, is marked by a sharp decrease in the surface energy. As the droplet breaks up at the first point, there are two competing effects influencing the overall surface area; the liquid surface tension, which tries to minimize the liquid surface area, and the formation of child droplets, increasing the surface area. During the breakup in this particular case, the surface tension force dominates and the surface energy falls rapidly as the droplet is being broken up. Surface and kinetic energies of the droplet reach a stationary value once the droplet looses most of its momentum and is incapable of further deformation and breakup.

Figure 4.8 shows the multimode breakup mechanism. This breakup phenomenology is observed when a 100 μm water droplet is given an initial velocity of 42 m/s to achieve a $We = 292$. Typical temporal evolution of droplet deformation and breakup in the multimode breakup regime is shown in this figure. As clearly seen, the droplet morphology during the start of the breakup process is similar to bag breakup with an additional stem oriented in the direction opposite to the droplet motion. The events leading to the formation of the bowl shape are similar to that of the bag breakup

regime except for the fact that due to a higher inertial force, the droplet rim becomes thinner forming a "lip". The time scale governing the motion of the liquid from the bottom to the top of the droplet is much larger than the "effective" time scale associated with the action of inertial forces on the droplet. This also leads to the formation of a stem which protrudes from the bottom of the droplet. Once the droplet slows down due to aerodynamic drag, a rim and a bag is formed, similar to bag breakup. Meanwhile, the lip along with the bag stretches and undergoes thinning. The formation of the lip leads to the development of a recirculation zone and creates a low pressure region inside the droplet just below the rim as shown in the gauge pressure contours in Figure 4.8. This difference in pressure leads to lip thinning, eventually leading to its breakup via pinch off. Depending on the flow conditions, the initial breakup can take place in the bag or the lip. This is followed by the breakup of bag, rim, and finally the stamen. The breakup of bag and the rim takes place via the same processes as that of bag breakup mechanism. The stamen breaks up due to oscillatory breakup owing to the reduced momentum of the droplet because of the action of drag force. Multimode breakup mechanism essentially encompasses bag and oscillatory breakup modes with additional features represented by the formation of lip and stamen.

Figure 4.9 shows the time evolution of kinetic and surface energies associated with the droplet. Similar to bag breakup, the normalized surface energy first increases to a maximum due to droplet deformation and then decreases once the droplet starts to break up due to the effect of surface tension, which retracts the droplet interface, thereby reducing the overall surface area. In contrast to bag breakup where the decrease in surface energy was rather abrupt at the point of breakup, the surface energy in this case decreases much more gradually. This can be explained using that fact that the breakup initialization in case of multimode breakup is more violent and produces more child droplets as compared to bag breakup. As a result, even though

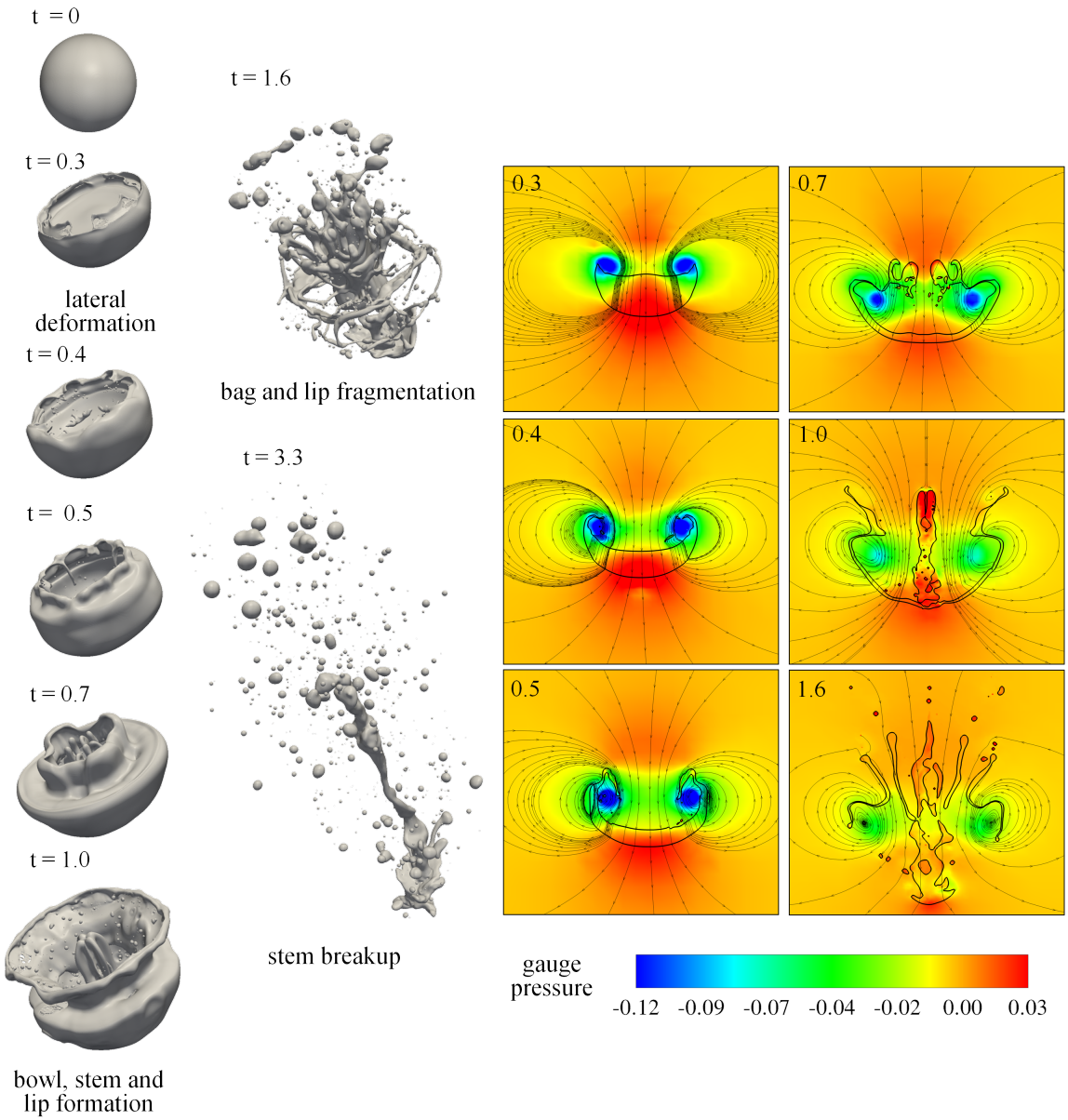

Figure 4.8. Multimode breakup - $We = 292$, $Re = 26635$, $\rho_l/\rho_g = 8.29$. Temporal evolutions of 3D droplet structure in non-dimensional time. Droplet iso-surface flooded, streamlines and gauge pressure contours. Non-dimensional time, t = T*U/D.

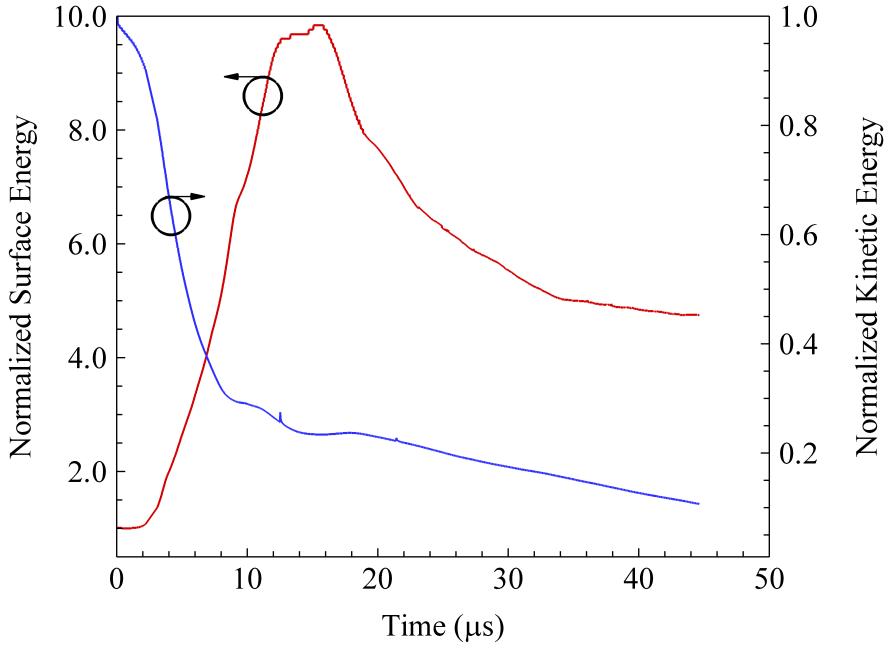

Figure 4.9. Evolution of surface and kinetic energy of the droplet for the multimode breakup regime.

the initialization of breakup is marked by decrease in surface energy, the rate at which the surface energy decreases is much lower than that of bag breakup.

4.4 Shear Breakup

We classify sheet thinning and wave travelling breakup as shear breakup throughout this thesis since the physics pertaining to shear and piercing breakup is similar (Lee & Reitz, 2000). As shown in Figure 4.10, shear breakup is the most violent of the four breakup regimes discussed in this chapter. In this particular case, the Weber number is 4237 at a density ratio of 8.29. The time associated with shear breakup process is the lowest in comparison to the other three regimes owing to extremely high inertial forces. In addition to sheet thinning we observe Rayleigh-Taylor (R-T) instability wave travelling on the droplet surface due to sudden acceleration of the denser droplet in a lighter medium. Bellman & Pennington (1954) investigated the effect of surface tension on R-T instability and found that there is a cutoff wave number below which

or equivalently a cutoff wavelength above which the perturbations become unstable, given by $\lambda_c = \sqrt{\dot{U}\left(\rho_l - \rho_g\right)/\sigma}$. A simple calculation using the time evolution of kinetic energy, shown in Figure 4.11, yields a cutoff wavelength ranging from 3.5 - 9.8 μm for this particular case, which is much smaller than the wavelength of smallest waves travelling on the droplet surface. The aerodynamic force exerted by the surrounding fluid causes deflection and thinning of the droplet periphery. This is enhanced by the unstable R-T waves travelling on the droplet surface. Sheet thinning of the droplet periphery in turn leads to the breakup of the parent droplet which is more or less like shedding of child droplets from the droplet surface. This is consistent with the observations made by several researchers in the past (Liu & Reitz, 1997; Lee & Reitz, 1999, 2000, 2001; Khosla *et al.*, 2006; Lopez-Rivera & Sojka, 2009). The thin film then breaks up into ligaments and child droplets. Since droplets are shed continuously in this breakup mechanism, as expected, we do not see a decrease in the surface energy, in fact as shown in Figure 4.11 the surface energy increases because of the rapid production of child droplets which increases the effective surface area and hence the surface energy. As a result, the previous approach of predicting the breakup initialization cannot be used for this breakup mechanism.

4.5 Generalized Regime Diagram

We studied the effect of pressure on the breakup process by conducting a thorough parametric study over wide range of pressure conditions and identified the critical Weber number for the various breakup modes discussed in this chapter. Qualitatively, the physics pertaining to different breakup mechanisms is similar at different pressure conditions. For example, Figures 4.12 and 4.13 shows the shear breakup morphology at 25 and 60 atm pressures respectively. Even though the fundamental breakup physics is independent of operating pressure, it was found that the critical

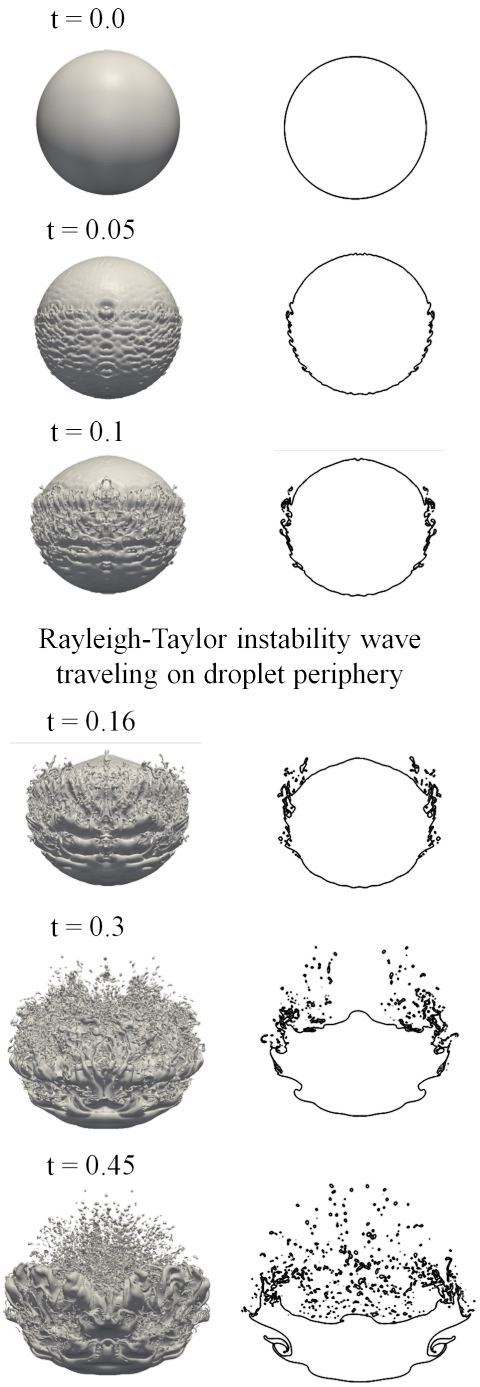

Figure 4.10. Shear breakup - We = 4237, Re =162350, ρ_l/ρ_g = 8.29. Temporal evolutions of droplet structure in non-dimensional time. Non-dimensional time, t = T*U/D.

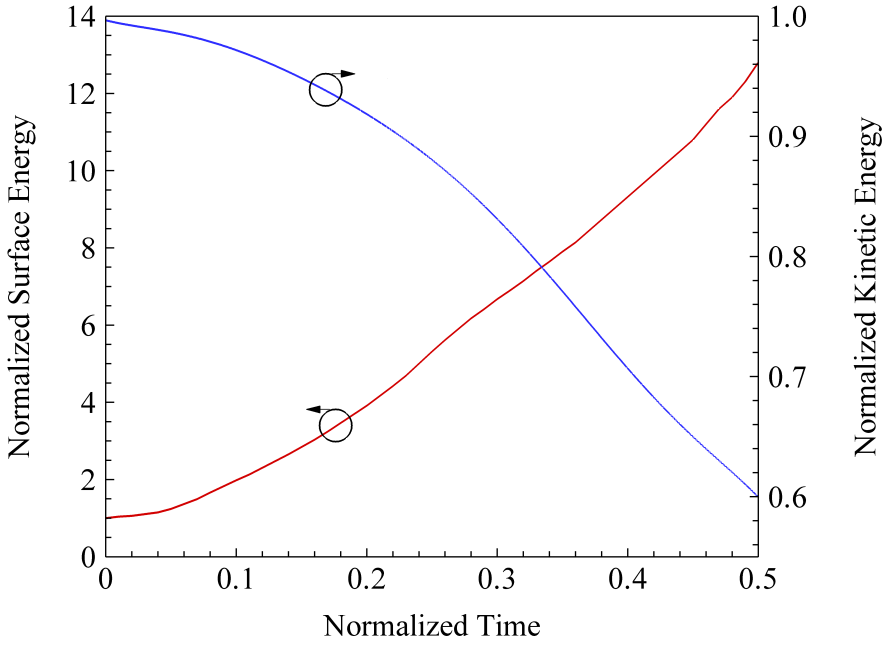

Figure 4.11. Temporal evolution of surface and kinetic energy of the droplet for shear breakup regime.

Weber number for water droplets corresponding to different breakup regimes is dependent on pressure, in addition to the Weber number. In particular, for 100 atm pressure conditions, the critical Weber numbers were found to be approximately 33, 110 and 1000, for bag, multimode and shear breakup regimes, respectively. This is shown graphically in Figure 4.14, which shows the calculation matrix for 100 atm, along with the critical Weber numbers for bag, multimode and shear breakup regimes identified during this work. These numbers differ considerably as compared to the one's found in the literature for lower pressure conditions (Hsiang & Faeth, 1995). It should be pointed out that even though experiments have been conducted at a wide range of density ratios, the density ratio in the experiments was varied by changing the liquid as opposed to changing the ambient pressure. In the present study, density ratio was changed by changing ambient pressure conditions. The difference in critical Weber numbers at different pressures suggests that the ambient pressure not

only changes the density ratio but has some other effect which, to the best of our knowledge, has not been identified before. The differences observed in critical Weber numbers at elevated pressure conditions can be explained using the fact that at higher pressures, the drag experienced by the droplet is much higher. This implies that the effective relative velocity between the droplet and the ambient environment reduces at a much higher rate as compared to lower pressures, i.e., the rate of change of momentum is much higher at high pressures. As a result the instantaneous Weber number decreases much faster and a higher Weber number is required to begin with for the droplet to undergo deformation and breakup (which shows phenomenological similarity to breakup process that occurs at lower pressure conditions) at higher pressure conditions. Qualitatively, our observations are confirmed by numerical simulations of droplet deformation and breakup performed by Sehgal *et al.* (1999), using a Lattice-Boltzmann method at a density ratio of 1. An empirical model was developed to take into account the pressure effect on the critical Weber number shown in Equation 4.1 which is valid for $Oh < 0.1$. Figure 4.15 shows the generalized regime diagram based on the developed model. It can be clearly seen that, as $p \rightarrow p_{cr}, We_{cr,p} \rightarrow \infty$, since $\sigma \rightarrow 0$ as $p \rightarrow p_{cr}$. The reference conditions for the model is 1 atm pressure, where experimental data exists. The black (experimental data, which was also confirmed by numerical simulations performed during the present study), green, red and blue symbols represent the critical Weber numbers for bag, multimode and shear breakup regimes at 1, 25, 60 and 100 atm pressures, respectively. In principle, this correlation can be used to predict the mode of breakup and the associated statistics at a broad pressure range. An example of the application of this correlation is present in the next section to predict SMD of the child droplet distribution at 1atm pressure conditions. The results agreed fairly well with the published experimental data.

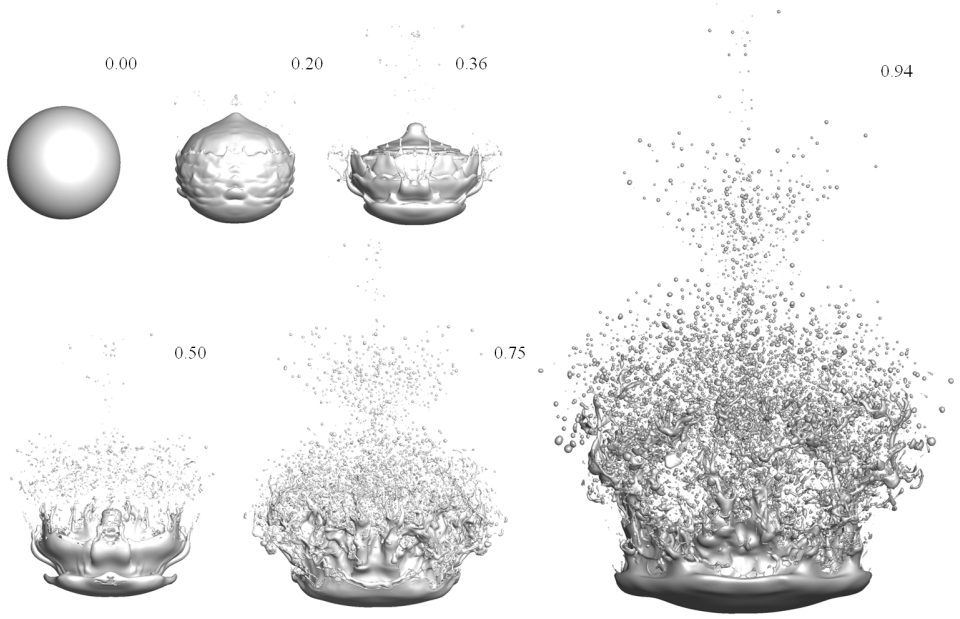

Figure 4.12. Shear breakup - $We = 373$, $P = 25$ atm. Temporal evolutions of 3D droplet structure in non dimensional time. Droplet iso-surface at various times. Non-dimensional time, t = T*U/D.

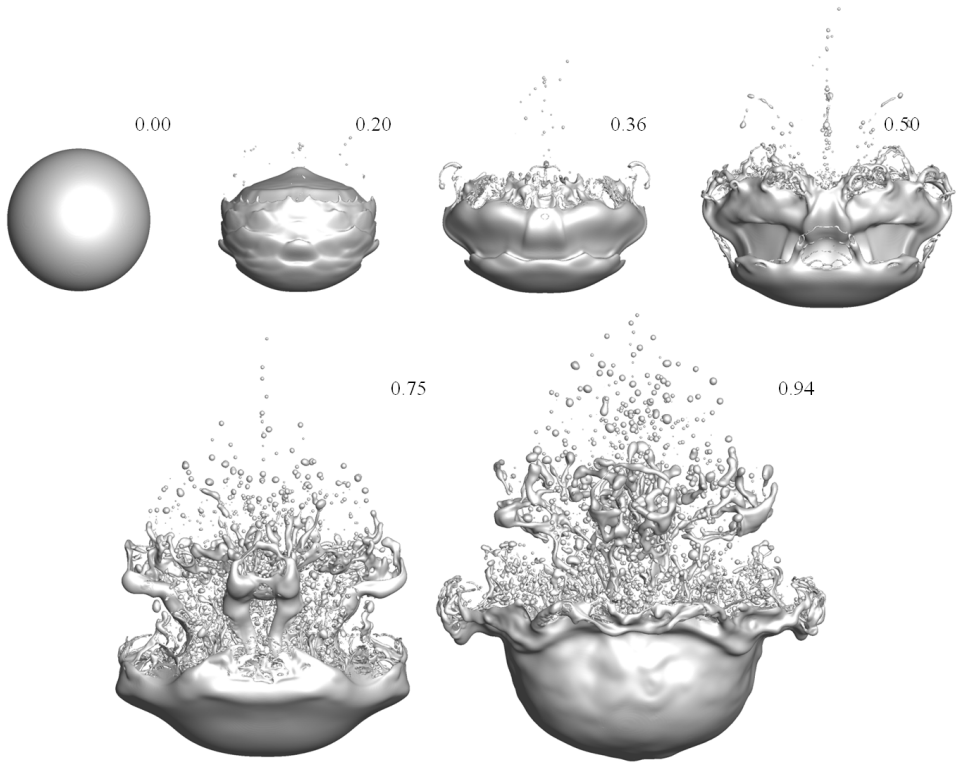

Figure 4.13. Shear breakup - $We = 486$, $P = 60$ atm. Temporal evolutions of 3D droplet structure in non dimensional time. Droplet iso-surface at various times. Non-dimensional time, t = T*U/D.

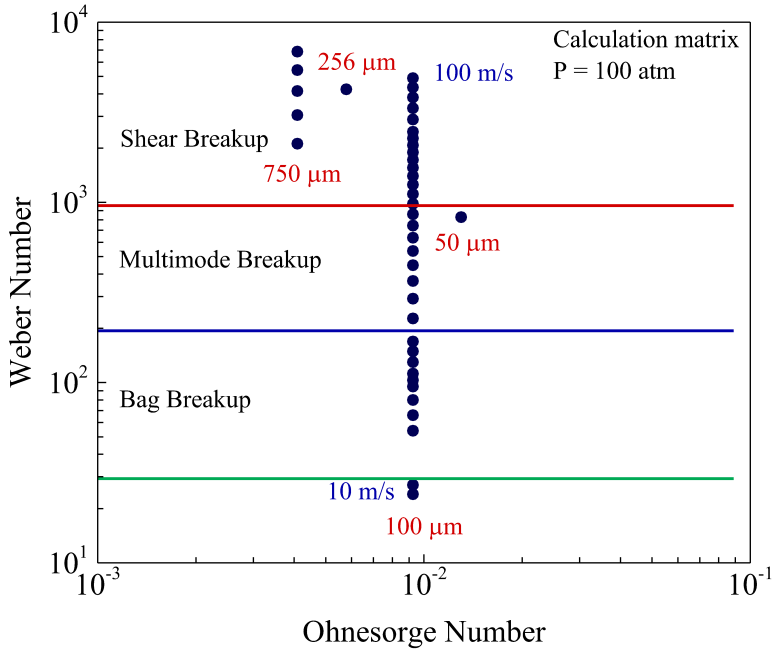

Figure 4.14. Regime diagram for 100 atm.

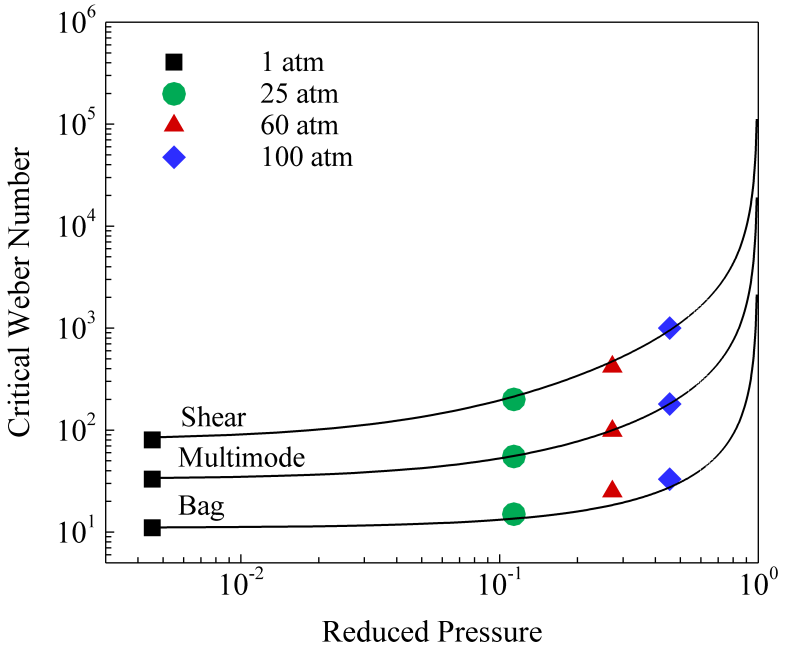

Figure 4.15. Generalized regime diagram.

$$We = We_{ref}\left\{1 + \frac{c}{1-p_r}We_{ref}\left[\left(\frac{\rho_g}{\rho_l}\right) - \left(\frac{\rho_g}{\rho_l}\right)_{ref}\right]\right\}$$
$$p_r = \frac{p}{p_{cr}},\ p_{ref} = 1atm,\ c = 0.62 \tag{4.1}$$

4.6 Child Droplet Diameter Distribution

Child droplet diameter distributions were studied for a wide range of Weber numbers. Interestingly, it was found that the normalized probability density distribution of the droplet diameters (shifted by 0.05), could be correlated using a log-normal distribution for $We > 300$ given by:

$$probability_{normalized} = \frac{1}{dC_1\sqrt{2\pi}}exp\left\{-\frac{(ln(d) - C_2)^2}{2C_1^2}\right\} \text{ for } We > 300,\ Oh < 0.1 \tag{4.2}$$

where d is the representative child droplet diameter, C_1 and C_2 are the correlation constants. Figure 4.16 shows the normalized probability density function of the child droplet diameters for Weber numbers of 365, 537, 636, 742, 858 and 1400. The symbols show the results obtained from the numerical simulations while the line is a log-normal distribution fitted to the data points. The PDFs are decidedly similar with almost the same C_1 and C_2 as listed in Table 4.3. Coincidently, $We > 300$ also corresponds approximately to the boundary between bag and multimode (and shear) breakup mechanisms.

For Weber numbers less than 300, the droplet distribution is discontinuous. As the droplet moves, it decelerates due to the action of drag force. This reduction in the relative velocity of the droplet changes the breakup mode to oscillatory breakup. This leads to the formation of relatively larger child droplets containing a large percentage of the original droplet mass. For example, during the bag breakup process, the bag thinning takes place with the formation of a thick rim, which has most of the mass from the original droplet. The bag breaks up with the formation of small fragments. This is also accompanied by the reduction in the instantaneous Weber

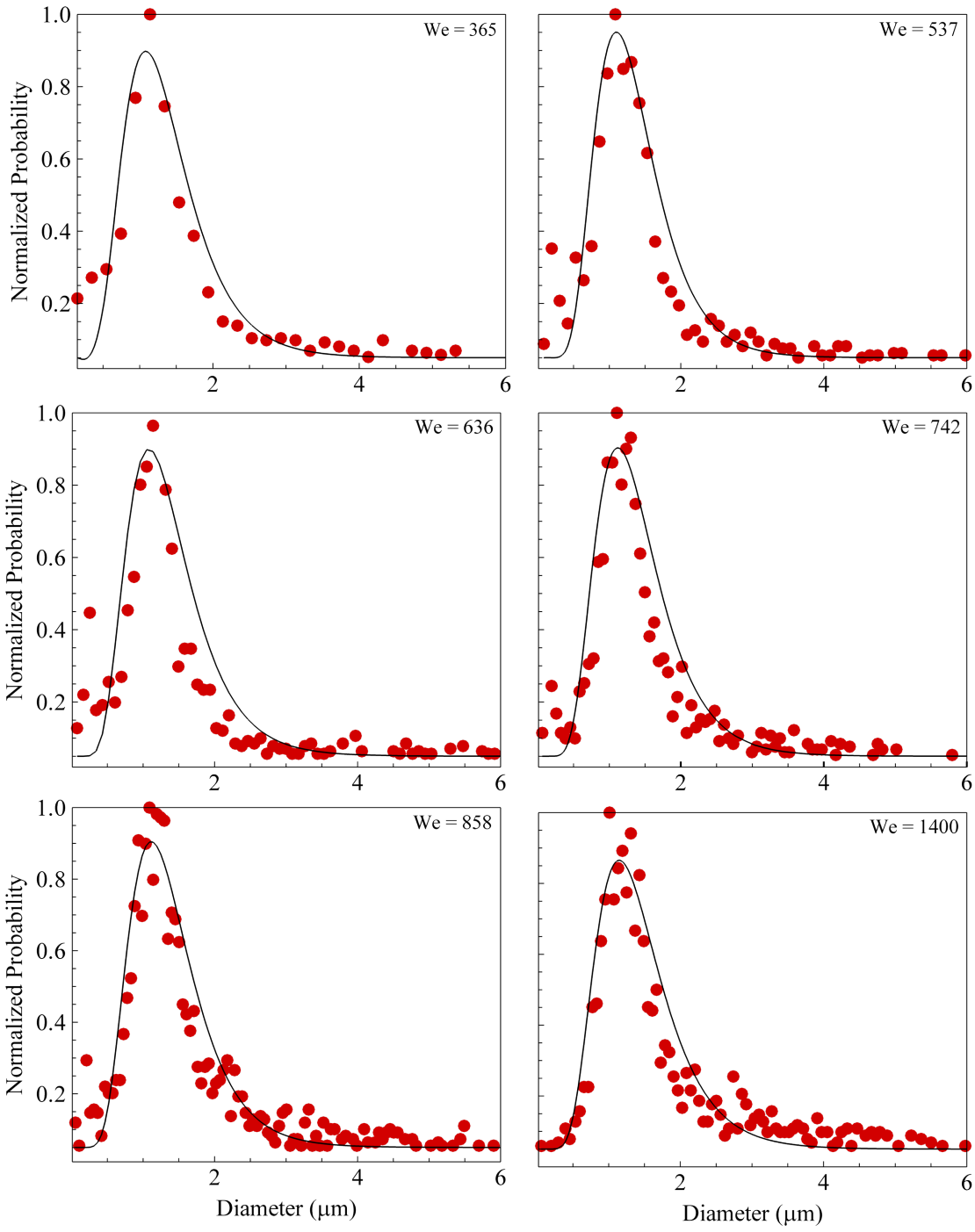

Figure 4.16. Normalized probability distribution of child droplet diameter for Weber numbers of 365, 537, 636, 742, 858 and 1400.

Table 4.3. Correlation coefficients C_1 and C_2 for a range of Weber numbers.

Weber number	C_2	C_1
365	0.2395	0.4010
447	0.2417	0.3646
537	0.2357	0.3753
636	0.2384	0.4005
742	0.2626	0.3877
858	0.2586	0.3884
981	0.2480	0.4041
1112	0.2879	0.4120
1253	0.3182	0.4218
1400	0.2926	0.3947

number of the droplet; as a result, the rim breakup takes place via oscillatory breakup mode producing larger droplets, and hence an overall discontinuous child droplet distribution.

The normalized probability distribution function of droplet sizes presented above is a number based probability normalized by its maximum value (so that the maximum value on the y-axis is 1). In order to take into account the liquid volume, we develop a correlation to predict the sauter mean diameter (SMD), d_{32}, of the droplet distribution. The end of breakup is marked by a steady state value of surface tension and inertial aerodynamic forces. Since these are competing forces and the breakup of the droplet primarily depends on them, the end of breakup process implies that they reach a certain kind of an equilibrium. If an effective representative sphere of diameter, d, is assumed for a given volume of liquid, the surface tension and aerodynamic forces can be written as:

$$\begin{aligned} F_{aerodynamic} &= \frac{1}{2} C_d \rho_g u_{rel}^2 A_{frontal} \\ where A_{frontal} &= \frac{\pi d^2}{4} \end{aligned} \tag{4.3}$$

$$F_{surface\,tension} = \sigma \pi d \tag{4.4}$$

$$\begin{aligned} &At\,equilibrium,\ F_{aerodynamic} = k F_{surface\,tension} \\ &k = constant,\ d = \frac{8k\sigma}{C_d \rho_g u_{rel}^2} \Longrightarrow \frac{d}{D} = \frac{8k}{C_d We} \end{aligned} \tag{4.5}$$

SMD was calculated for a range of Weber numbers from the present DNS calculations. Since SMD and d are characteristic diameters associated with a particular Weber number, they can be correlated using the relation obtained in equation 4.5, given by:

$$\frac{d_{32}}{D} = f(We)\frac{d}{D} = k f(We)\frac{8}{C_d We} \tag{4.6}$$

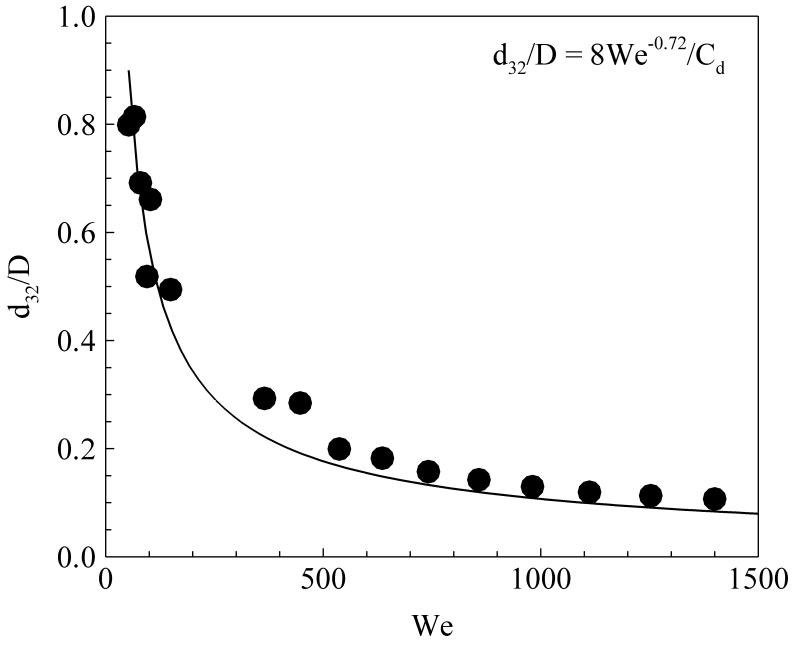

Figure 4.17. Sauter mean diameter, d_{32}, correlated using an analytical model .

where $f(We)$ is chosen not only because it is the most important non-dimensional quantity in the present physical situation but also because it represents a quantity similar to d_{32}. Figure 4.17 shows the predicted SMD along with the one obtained from the simulation. The final form of the correlation is given by:

$$kf(We) = We^{0.28} \tag{4.7}$$

$$\frac{d_{32}}{D} = \frac{8We^{-0.72}}{C_d} \tag{4.8}$$

Here, $C_d = 0.5$, which corresponds to the drag coefficient of flow over solid spheres in the range $10^3 < Re < 10^5$, where all the numerical simulations were performed. In general, C_d changes throughout the lifetime of the droplet, as will be seen in Chapter 5, but since the child droplets have a tendency to assume spherical geometry due to surface tension, the use of drag coefficient corresponding to flow over solids spheres seems appropriate for the determination of d_{32}. Excellent agreement between the model and the numerical data is observed. The correlation predicts that the SMD

distribution does not change significantly beyond We of 300, which also bolsters the previous finding that the PDF of droplet diameter follows a universal log-normal distribution for $We > 300$. The results for SMD for shear breakup regime, which we define beyond Weber numbers of approximately 1000 for 100 atm pressure conditions, seems to asymptote to a value near 0.1.

As a last step, we use the generalized regime diagram and SMD correlation to predict the SMD of droplet distribution for a Weber number of 125 at 1 atm conditions. Quasi steady correlation developed by Chou *et al.* (1997) proposed that SMD/D = 0.09 (with a 22% standard deviation) for the shear breakup regime. If we use our generalized correlation (equation 4.1) to obtain the corresponding Weber number at 100 atm which pertains to the same breakup physics as exhibited by Weber number of 125 for water/air system at 1 atm, and use equation 4.8, we find that our correlation yields a value of 0.11, which is quite close to the experimental predictions and lies within the range of experimental error. This further validates the used approach and the generalized regime diagram developed during the course of this study. A similar procedure can be used to predict a number of properties associated with droplet breakup phenomena at a wide pressure range.

4.7 Concluding Remarks

To summarize, this chapter addresses the deformation and fragmentation of Newtonian liquid droplets over a broad range of operating pressures, Reynolds and Weber numbers. Even though single droplet deformation and breakup has been a subject of active research for a long time, to our knowledge, this is the perhaps the first time that a comprehensive study (experiments or computations) over a broad range of operating pressure, Weber and Reynolds numbers has been conducted, highlighting the temporal evolution of details, including pressure, velocity, structure dynamics and shear stress of this complex multiphase phenomena. Previous experimental studies relied

on visual graphics to describe the breakup process while computational studies were conducted either with two-dimensional or axisymmetric assumption, and thus were unable to capture all the details. For Newtonian fluids, we *quantitatively* identified four different breakup mechanisms, oscillatory, bag, multimode and shear breakup modes, which corroborates the observations made by other researchers. In general, the aerodynamic drag force exerted by the surrounding fluid causes the droplet to deform. The deformation is resisted by viscous and surface tension forces. The breakup mechanism becomes progressively violent as the Weber number increases and the breakup process changes from oscillatory to shear breakup. The droplet lifetime decreases as the inertial force increases in comparison to the surface tension force. The physical mechanism leading to breakup for the four breakup modes can be summarized as follows:

1. Oscillatory: The droplet deforms into an ellipsoid due to unequal pressure distribution on its surface. The pressure difference and vibration of the droplet further leads to the formation of a bowl, followed by a dome. This is followed by the stretching of the droplet in the flow direction, eventually, leading to breakup due to excessive shear stress development.

2. Bag: Similar to oscillatory breakup, the droplet first deforms into a disk and then into a bowl. Because of higher inertia, the bowl is further transformed into a thin bag. The bag becomes progressively thinner and finally breaks up followed by the disintegration of the rim.

3. Multimode: At progressively higher We numbers, multimode mechanism becomes the dominant mode of breakup. Due to an even higher inertial force, the bag development is accompanied by the formation of a "lip" and a stamen. The breakup process can either start from the lip or from the bag depending on the flow conditions. This is followed by the disintegration of the rim and the stem

to form ligaments and child droplets.

4. Shear: This is the most "explosive" breakup mode studied in this research. The droplet breaks up due to the formation of R-T waves, which enhances sheet thinning of the droplet at the periphery, eventually leading to child droplet shedding from the surface.

Child droplet diameter correlations were also developed and it was found that a log-normal distribution describes the child droplet diameter distribution with excellent accuracy. The distribution seemed to be similar for Weber number greater than about 300. For smaller Weber numbers, the distribution was found to be discontinuous due to smaller inertial force associated with it. A theoretical model was also developed to predict the SMD (d_{32}) of droplet distribution. The correlation agreed reasonably well with numerical and experimental results. Another highlight of the current work was the development of a generalized regime diagram, which was based on the current simulation results, along with data obtained from the literature to predict the critical Weber numbers at a wide range of pressure conditions valid for $Oh < 0.1$.

CHAPTER V

DRAG COEFFICIENTS OF DEFORMING AND FRAGMENTING LIQUID DROPLETS

5.1 Literature Review and General Overview

Coefficient of drag for flow over spherical objects is a fundamental quantity in fluid dynamics and has been a part of published literature for over 150 years (Stokes, 1851). According to Maxey & Riley (1983), the total force acting on a particle is given by:

$$f_i = f_i^d + f_i^l + f_i^{\nabla p} + f_i^v + f_i^b + mg_i \tag{5.1}$$

Here f_i^d is the steady-state drag force, f_i^l the lift force and $f_i^{\nabla p}$ includes the force due to the local pressure gradient and the shear-stress of the carrier phase. The unsteady forces can be divided into virtual mass force f_i^v due to the acceleration of the particle and the Basset history force, $mg_i$is the force due to gravity. Numerical study of liquid sprays and other particle laden flows traditionally involve Eulerian-Lagrangian framework where the Eulerian equations of motion, i.e., the Navier-Stokes equations, are used to model the continuous phase and the dispersed phase is modeled by Newtons second law of motion using Equation 5.1. For most practical purposes, steady-state drag force is the most important force acting on the particle and hence accurate evaluation of drag coefficient becomes extremely important. Figure 5.1 shows the variation of drag coefficient for non-deformable spheres as a function of Reynolds number (Schlichting, 1979). This plot can be divided into Stokes, viscous and Newton's regime based on the flow Reynolds number as suggested by Kolev (2012). Theoretical and experimental investigations have been conducted by numerous researchers in the past to study the motion of solid spheres and the drag coefficient associated with them (Proudman & Pearson, 1957; Odar & Hamilton, 1964; Taylor & Acrivos, 1964; Chester

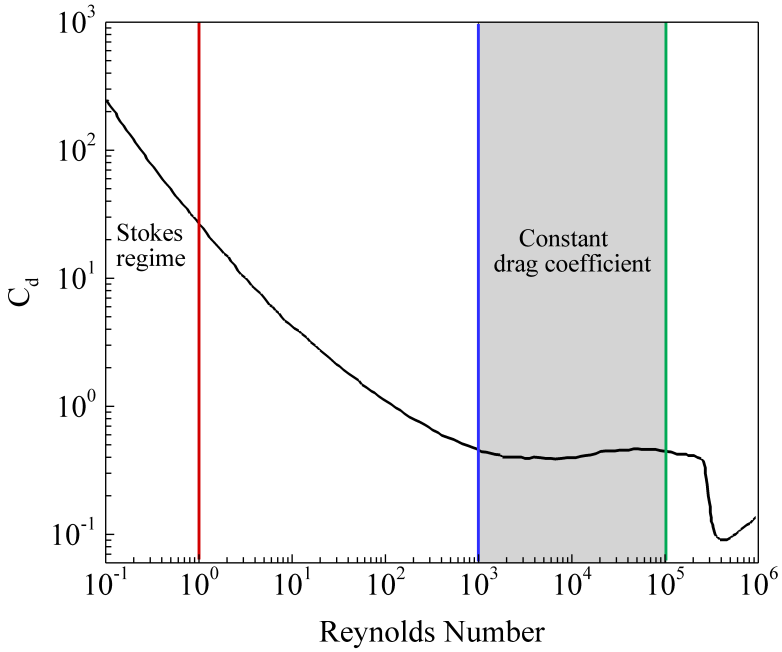

Figure 5.1. Drag coefficient for solid spheres as a function of Reynolds number (Schlichting, 1979).

et al., 1969; Pruppacher *et al.*, 1970; Ockendon & Evans, 1972; Flemmer & Banks, 1986; Turton & Levenspiel, 1986; Kim *et al.*, 1998; Kurose *et al.*, 2003; Michaelides, 2006; Almedeij, 2008). Kelbaliyev (2011) and Almedeij (2008) summarized some of the major empirical correlations which have been developed to predict drag coefficients on solid spheres. Several studies on non-spherical, non-deformable shapes have also been performed by researchers in the past (Kelly *et al.*, 1971; Swamee & Ojha, 1991; Michaelides, 2006; Gabitto & Tsouris, 2008). A review of currently available correlations for drag coefficient over non-spherical objects can be found in Chhabra *et al.* (1999) where the authors evaluated various correlations and compared them to experimental data obtained from independent sources.

Let us consider incompressible flow over a solid sphere. Figure 5.2 shows the recirculation bubble in $x - y$ plane for incompressible flow past a solid sphere for $Re < 200$. Air flows in the domain from left to right. At very low Reynolds numbers,

the flow is completely attached to the surface and there is no separation. As the Reynolds number increases, the flow separates due to adverse pressure gradient at the surface of the sphere and further reattaches to form a symmetric separation bubble. The rear stagnation point, $\theta = 0$, corresponds to the highest pressure and is called the stagnation pressure. The pressure decreases until $\theta = 90$, after which the flow experiences an adverse pressure gradient and it separates. Topologically similar flow features can be observed for $Re < 210$ (Johnson & Patel, 1999) with an increase in the length of the separation bubble and the movement of the separation point upstream with increasing Reynolds number as shown in Figure 5.2. Vorticity is generated near the surface due to no-slip boundary condition and pressure gradient at the wall. It is then convected and diffused downstream. Once the Reynolds number goes beyond 210, the flow does not reattach and the wake becomes unsteady, leading to vortex shedding. Figure 5.3 shows the length of recirculation bubble for axisymmetric wakes as a function of Reynolds number. Our results shows excellent agreement with other results published in the literature (Taneda, 1956; Tomboulides *et al.*, 1993; Johnson & Patel, 1999). Figure 5.4 shows the $x-y$ plane for incompressible flow over an ellipse. As before, air flows from left to right. Similar to the sphere, as the Reynolds number increases, the flow separates due to adverse pressure gradient and then reattaches to form a recirculation bubble. Once the Reynolds number reaches a high enough value, vortices are shed, as shown in Figure 5.5, which shows contour lines of y-velocity for flow over an ellipse for $Re = 1000$.

If the physical situation of interest involves deformable solids where the size changes, such as crystal formation, granulation, or a process where the particle disappears completely such as vaporization and combustion, theoretical determination of drag coefficient becomes extremely difficult, and it is usually estimated using empirical correlations based on experimental data. Determination of drag coefficient becomes

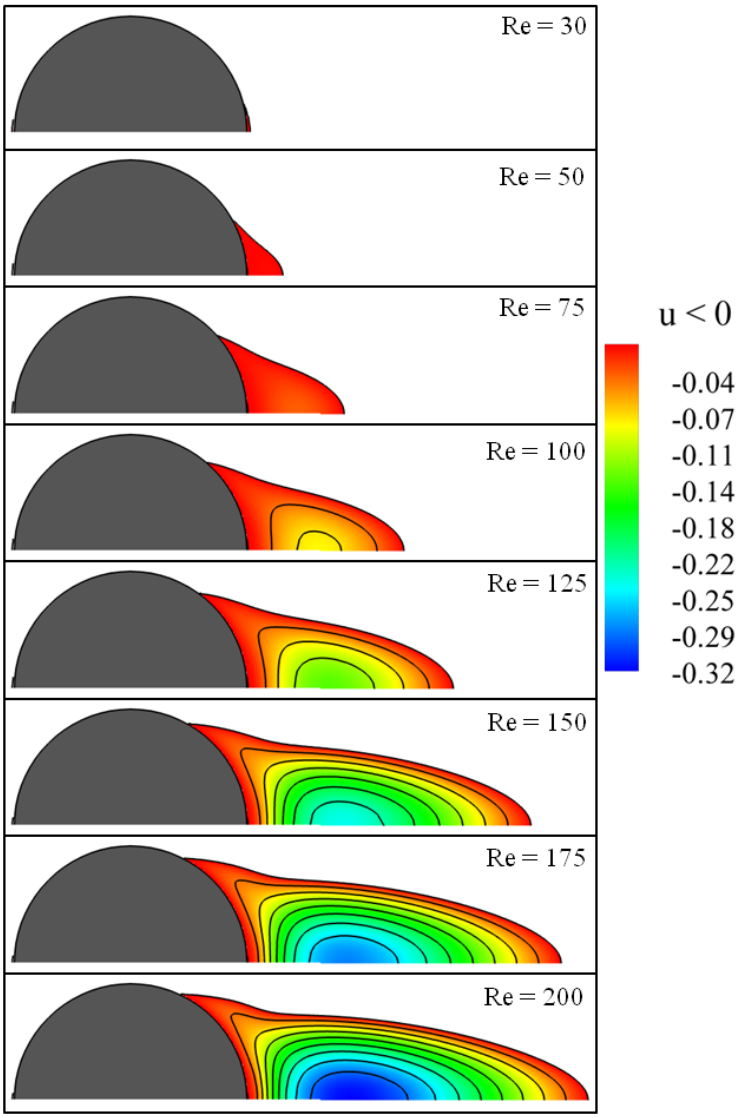

Figure 5.2. Flow over a sphere: recirculation zone for $Re < 200$. The contour shows $u < 0$.

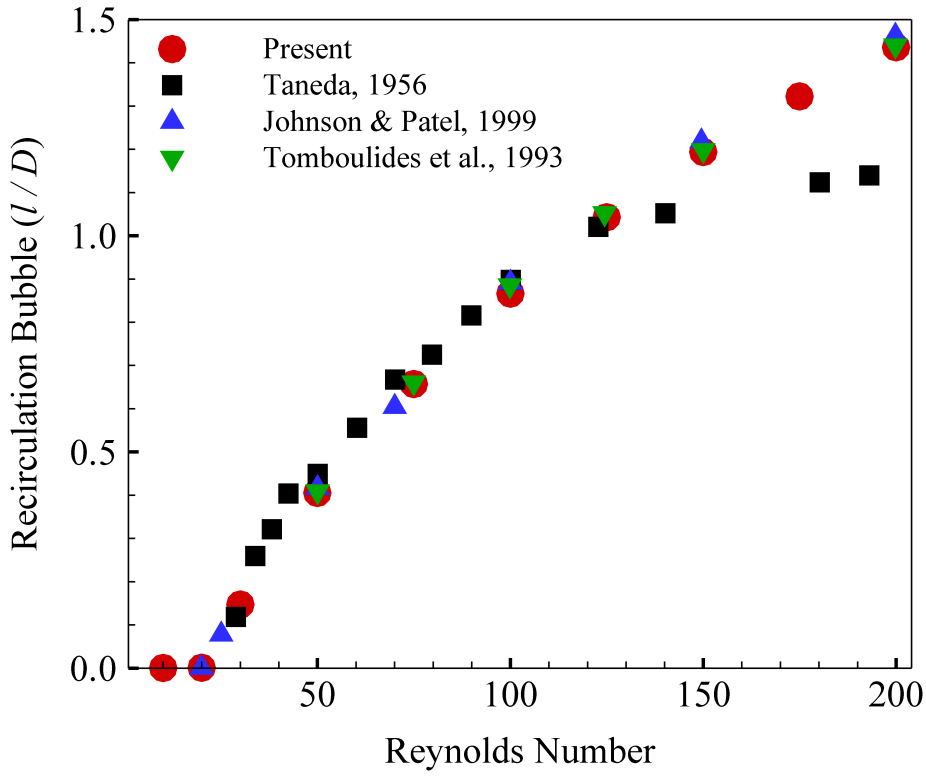

Figure 5.3. Length of recirculation bubble as a function of Reynolds number.

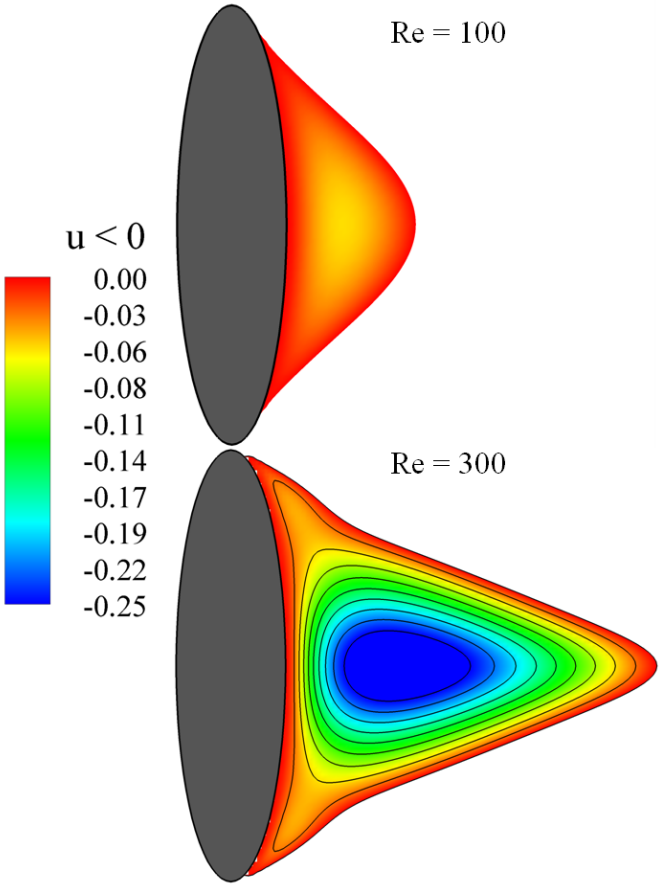

Figure 5.4. Flow over an ellipse: recirculation zone for $Re = 100$ and 300. The contour shows $u < 0$.

even more formidable in case of liquid droplets because of surface pulsations, hydrodynamic instabilities, evaporation, deformation and breakup. Spherical droplets deform due to the action of aerodynamic forces. The deformation and fragmentation is resisted by surface tension and viscous forces. As pointed out by researchers in the past, the magnitude of the inertial to surface tension force, i.e., the Weber number dictates the breakup mechanism (Krzeczkowski, 1980; Arcoumanis *et al.*, 1994; Faeth *et al.*, 1995; Arcoumanis *et al.*, 1996; Faeth, 1996, 2002).

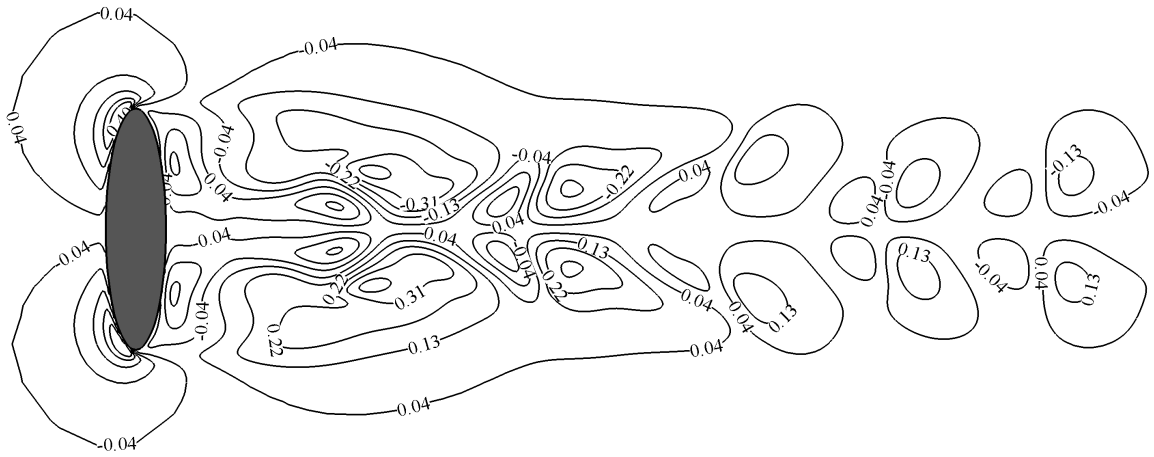

Figure 5.5. Flow over an ellipse: vortex shedding at $Re = 1000$.

Several experimental investigations on liquid droplet motion have been conducted in the past which have addressed droplet drag coefficient (Hadamard, 1911; Yuen & Chen, 1976; Stone, 1994; Warnica *et al.*, 1995*a*,*b*; Abbad & Souhar, 2004; Fisher & Golovin, 2007; Mashayek & Ashgriz, 2011). Temkin & Mehta (1982) performed experiments to study the motion of small droplets under the action of accelerating and decelerating flows using a shock tube facility. The Reynolds number was limited to 100 and the Weber number to 0.137 so that there was no deformation. A correlation for drag coefficient was proposed for practically non-deforming droplets in a strong unsteady environment. Drag coefficient of non-evaporating, spherical, liquid droplets in quiescent gaseous fields was also measured for a $20 < Re < 120$ and $We < 10$ by Warnica *et al.* (1995*a*). It was inferred that the drag coefficient decreases with increase in Reynolds and Weber number.

The time and length scales associated with physical processes at the interface of liquid droplet during the deformation and breakup process are often so small that experimental apparatus cannot resolve them and high fidelity numerical calculations are required to elucidate the phenomena. Sugioka & Komori (2007) conducted 3-D direct numerical simulations (DNS) to study drag and lift forces on a spherical water

droplet in homogeneous shear flow. The study was limited to particle Reynolds numbers of 300 and deformation was not considered in the study owing to an extremely low Weber number of 0.3. It was concluded that the drag coefficient on a spherical droplet increases with increasing shear rate for a fixed value of the particle Reynolds number.

More recently, Wadhwa *et al.* (2007) conducted axisymmetric calculations to study transient deformation and drag of decelerating droplets. Although deforming liquid droplets were considered but breakup of the droplet was not modeled in the study which can have considerable influence on the drag coefficient. Operating conditions corresponding to $We < 100$ and $0.001 < Oh < 0.1$ were considered and it was concluded that oblate shapes result in greater drag and prolate shapes in lower drag relative to the drag experienced by solid spheres.

In this chapter we focus on the determination of drag coefficient of deforming and fragmenting liquid droplets. The study focuses on the temporal evolution of drag coefficient along with the development of a correlation to predict the time averaged drag coefficient for a wide range Weber numbers. Practical Reynolds number of interest, especially for aerospace applications generally falls in the category of Newton's regime where the drag coefficient for a non-deformable sphere has a constant value. As a result, the most important non-dimensional parameter in the current study is the Weber number. To isolate the hydrodynamic mechanisms dictating droplet breakup phenomena, evaporation is neglected and simulations are performed at isothermal conditions. DNS calculations at a wide range of operating pressure conditions and Weber numbers are conducted. Since droplet dynamics inside a combustion chamber is one of the most challenging and unresolved problems in the literature, we concentrate on the results obtained at low density ratio environment. The droplet structure, and statistics associated with the parent and child droplets are tracked as a function of time, which are then used to evaluate the drag coefficient from first principles. Once

temporal evolution of drag coefficient is calculated, we develop a correlation for time-mean drag coefficient of deforming and breaking liquid droplets valid for a wide range of Weber numbers in a non-evaporating environment. The details of droplet breakup physics and child droplet statistics have been discussed in the previous sections. The results in this chapter are based on Khare & Yang (2013).

5.2 Data extraction and coefficient of drag for deforming and fragmenting droplets

As the droplet moves in the ambient environment, momentum is exchanged between the liquid droplet and the surrounding air. The drag coefficient is defined by:

$$C_d(t) = \frac{\frac{d\left(mu_{rel}(t)\right)}{dt}}{1/2\rho_g u_{rel}^2(t) A_{frontal}(t)} \qquad (5.2)$$
$$where A_{frontal}(t) = \pi r_{effective}^2(t)$$

The numerator is the time dependent drag force acting on the droplet. The projected frontal area, $A_{frontal}$, is defined as the frontal area of a sphere of equivalent surface area. The droplet shape evolves in time and as a result the frontal area is also a time varying quantity. Data extraction for the current research work is conducted by tracking the temporal location and associated properties of the liquid phase. Droplet momentum, relative velocity, location and surface area are calculated at each time step. Using these properties, the drag coefficient is calculated using equation 5.2 as the droplet moves in the ambient environment. A broad range of Weber numbers from 0.1 to 1400 was considered during the current work, encompassing bag, multimode and shear breakup mechanisms. Since most of the practical operating conditions lie in Newton's regime, where the drag coefficient over a solid sphere has a constant value independent of Re. All the results pertaining to the drag coefficient presented in this chapter are normalized by a constant value, $C_{d,0} = 0.45$ (Efstathios & Clayton, 2005). Consequently, the drag coefficient of deforming and breaking liquid droplets is

solely treated as a function of Weber number. Three different breakup mechanisms, namely, bag, multimode, and shear breakup modes are addressed during the current research effort. Weber number governs the transition from one breakup mechanisms to another. In the next three sections, the different breakup modes will be discussed in detail with emphasis on the evaluation of drag coefficient.

5.2.1 Bag breakup

Typical temporal evolution of droplet structure for bag breakup mechanism is shown in Figure 5.6. The figure corresponds to a water droplet of 100 μm with a velocity of 22 m/s. As the droplet starts to move in the ambient environment, it first deforms laterally into a disk with a lid. This is followed by the formation of a bowl. Because of inertia, the bowl is further transformed into a thin bag due to the movement of the liquid from the bottom to the rim. The bag becomes progressively thinner and finally breaks up starting with the formation of a web like structure followed by the disintegration of the rim. The detailed physics pertaining to this phenomena is discussed in Section 4.3. The physics we are interested in exploring in the current section pertains to time history of drag coefficient as the droplet moves. As reflected by equation 5.2, C_d for deformable objects is primarily dependent on the time history of momentum and frontal area. Therefore, it is informative to look at the bottom view of the droplet structure to appreciate the extent of area change during the droplet lifetime. This is shown in Figure 5.7. It is quite clear from the figure that there is a tremendous increase in the frontal, as well as the overall surface area of the droplet as it deforms and breaks up. Once the breakup initializes, there are two competing forces effecting the surface area; externally imposed inertial forces and formation of child droplets, which are trying to increase the surface area and surface tension force causing surface retraction to prevent the growth of surface area. Figure 5.8 shows the time history of momentum and surface energy during bag breakup process

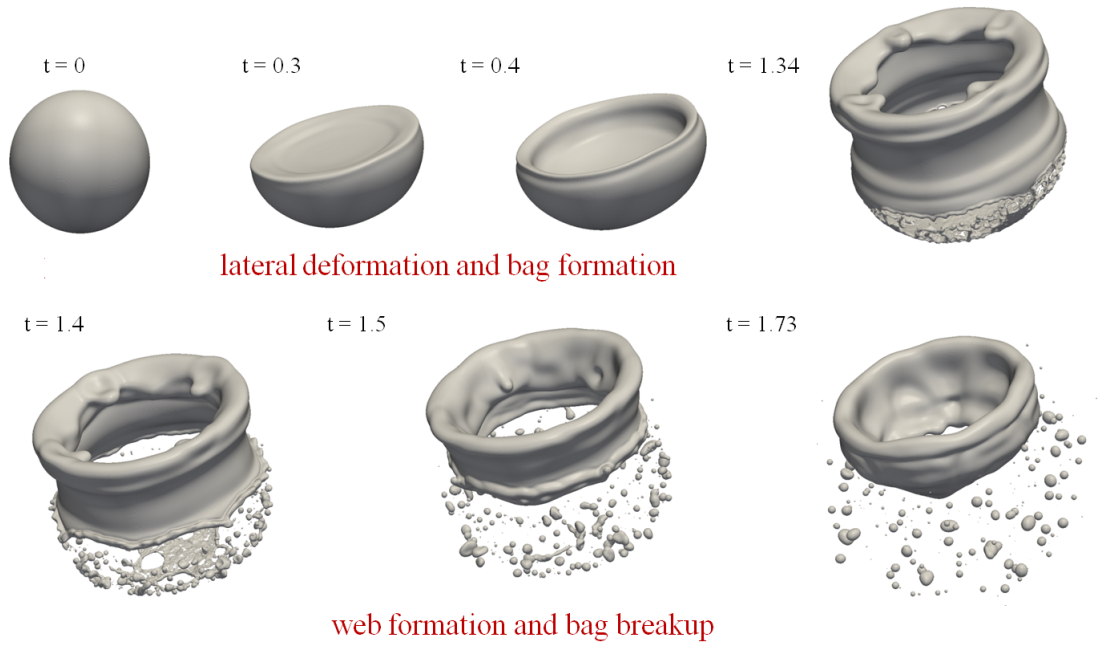

Figure 5.6. Perspective view of the temporal evolution of droplet structure for bag breakup mechanism. $We = 80$, $Re = 13951$, $\rho_l/\rho_g = 8.29$, $t = T * U/D$.

and elucidates this complex physics in a more quantitative manner. Momentum is normalized by its initial value, so that it takes a maximum value of 1. On the horizontal axis, non-dimensional time is defined as $t = T * U/D$, where D and U are the initial diameter and velocity of the droplet respectively. The droplet starts with some initial value of momentum, corresponding to the initial velocity imparted to the droplet. As it moves further, it is resisted by surface tension and viscous forces and the momentum is transferred to the surroundings. The surface energy, defined as the product of surface tension and surface area, has the minimum value at the beginning of the simulation when the droplet is spherical. It is normalized by this minimum value and hence has a value of 1 at $t = 0$. As the droplet deforms, the surface energy increases till the point of breakup where it falls suddenly due to surface retraction. Qualitatively, we can expect the drag coefficient to increase initially due to the rapid decrease of momentum associated with the droplet owing primarily to pressure drag. Once the droplet breakup initializes, the drag coefficient is expected to decrease.

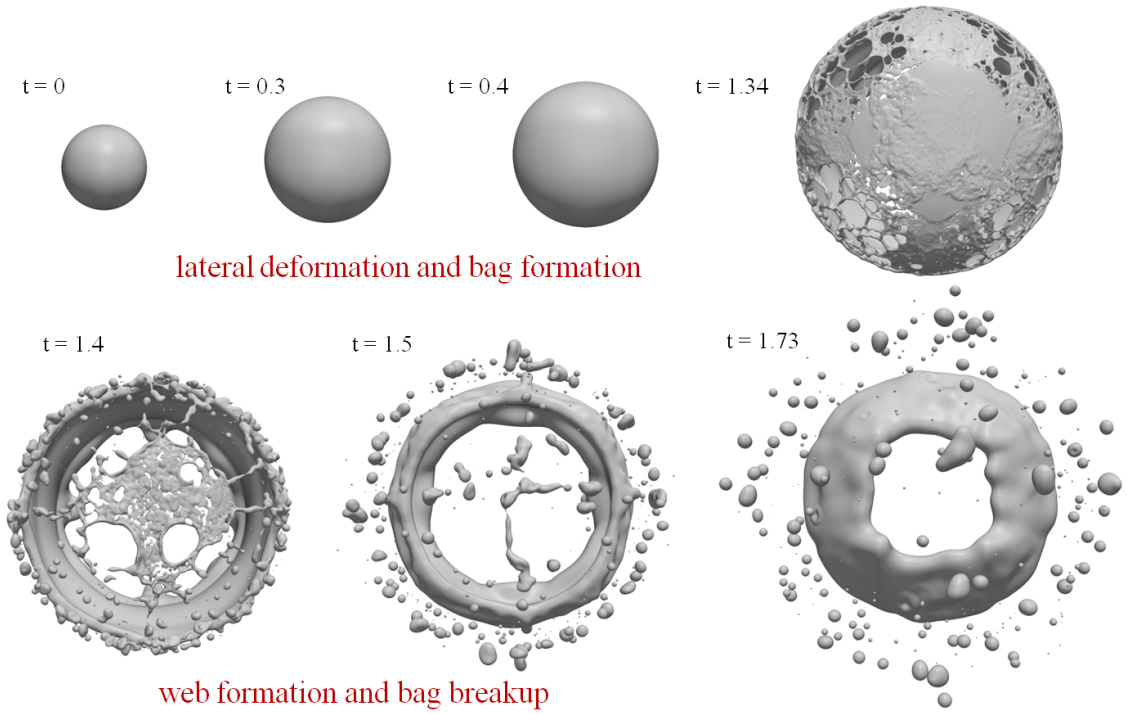

Figure 5.7. Bottom view of the temporal evolution of droplet structure for bag breakup mechanism. $We = 80$, $Re = 13951$, $\rho_l/\rho_g = 8.29$, $t = T * U/D$.

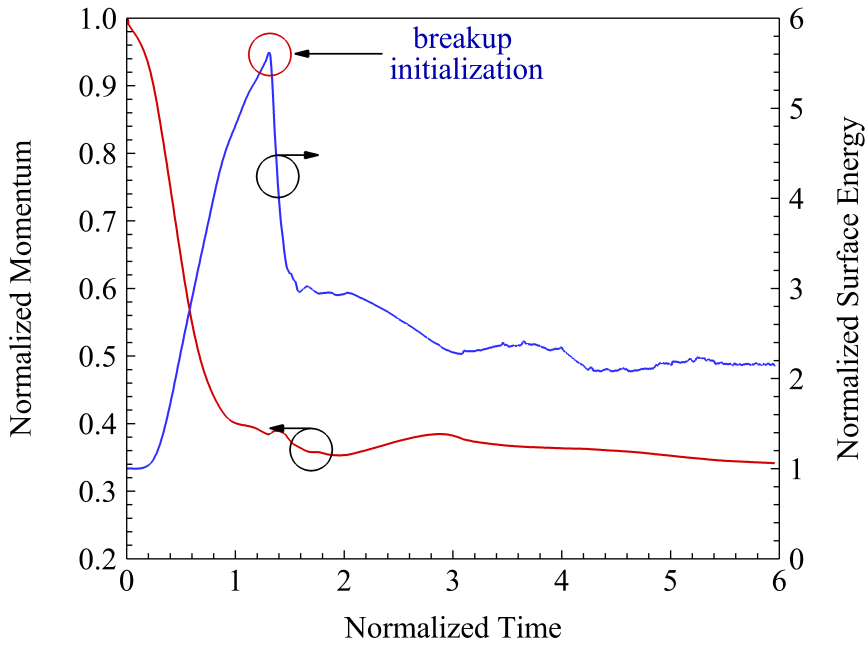

Figure 5.8. Time evolution of momentum and surface energy for $We = 80$.

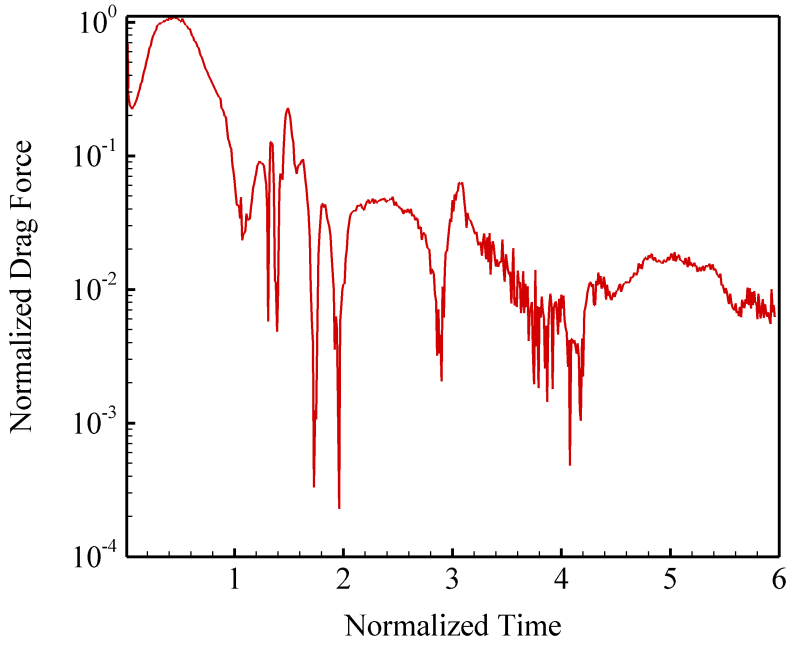

Figure 5.9. Time history of normalized drag force for bag breakup ($We = 80$).

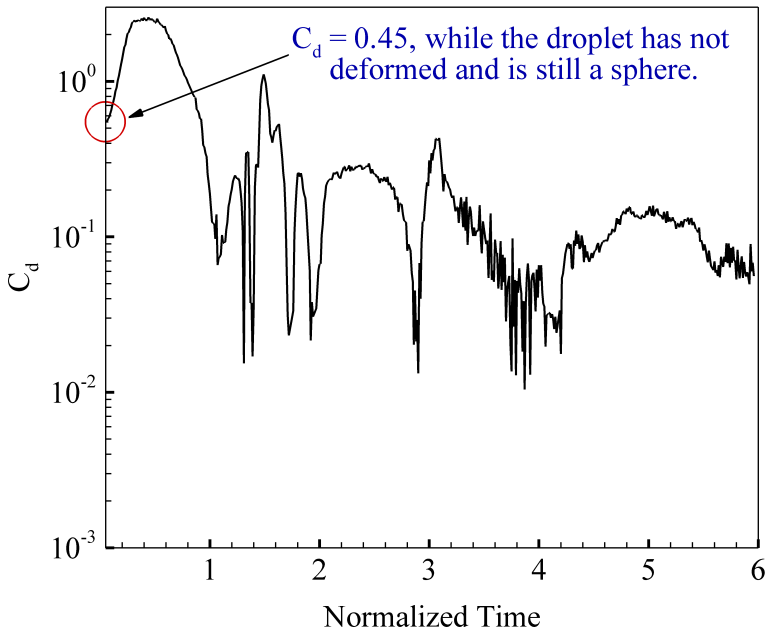

Figure 5.10. Time history of drag coefficient for bag breakup.

Figures 5.9 and 5.10 show the variation of normalized drag force and C_d for bag breakup process. This was calculated by taking the gradient of momentum shown in Figure 5.8 and using the definition of drag coefficient from equation 5.2. Initially, while the droplet is still spherical, the drag coefficient has a value corresponding to that of flow over a solid sphere. As expected, the drag coefficient first increases to a maximum value and then dips down. Once the droplet starts to breakup via the formation of webs and holes, as seen in Figure 11, the surface area and as a result the surface energy falls rapidly. By this time the droplet has already lost most of its momentum and hence the drag coefficient decreases. The instantaneous Weber number of the droplet reduces as time progresses and the surface tension force becomes comparable to the inertial forces acting on the droplet. This causes the droplet to oscillate. Oscillations of the droplet has a much more prominent effect on the surface area as compared to the momentum and as a result the drag coefficient oscillates between moderately small values (owing to a very small change in the droplet momentum).

5.2.2 Multimode breakup

At progressively higher Weber numbers, multimode mechanism becomes the dominant mode of breakup. Due to an even higher inertial force, the bag development is accompanied by the formation of a lip and a stamen. The breakup process can either start from the lip or from the bag depending on the flow conditions. This is followed by the disintegration of the rim and the stem to form ligaments and child droplets. This is shown in Figure 5.11. The droplet diameter and velocity in this case were 100 μm and 47 m/s respectively. The detailed physics associated with this breakup mode can be referred to in Section 4.3. Figure 5.12 shows the time evolution of momentum and surface energy associated with a droplet undergoing multimode breakup. The initial events during this breakup process are similar to bag breakup, as shown in the

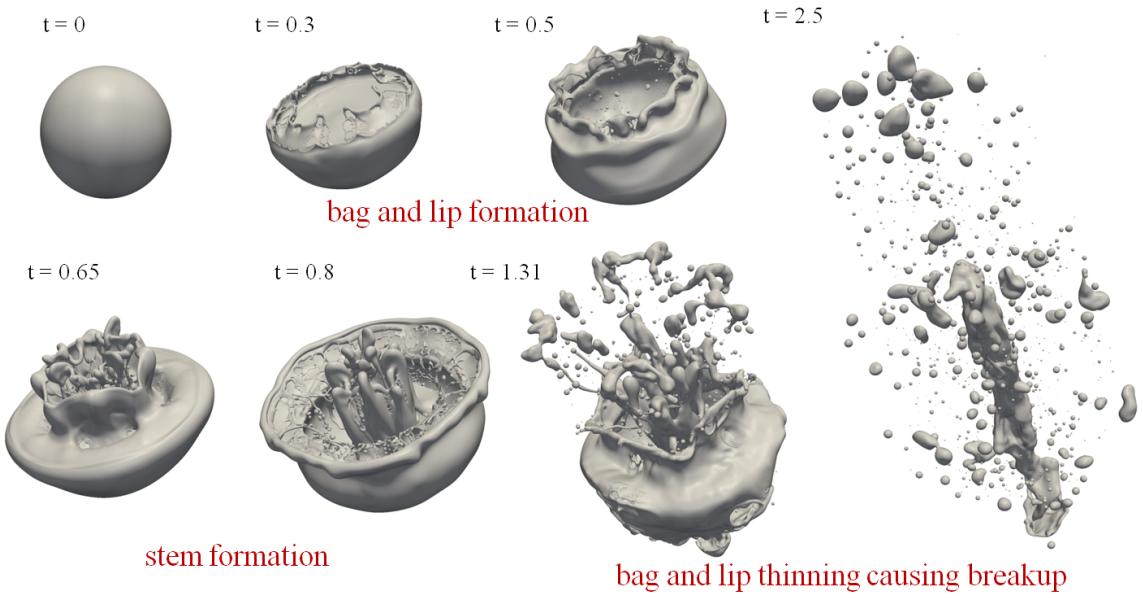

Figure 5.11. Perspective view of the temporal evolution of droplet structure for multimode breakup mechanism. $We = 365$, $Re = 29805$, $\rho_l/\rho_g = 8.29$, $t = T * U/D$.

3D figures as well as the evolution of momentum and surface energy associated with the droplet. As pointed before, there are two competing effects affecting the overall surface area; the liquid surface tension, which tries to minimize the liquid surface area, and the formation of child droplets, increasing the effective surface area. Depending on the breakup mechanism, the beginning of breakup is accompanied with a sharp or a gradual reduction in surface energy. In this case the decrease in surface energy is rather gradual, indicating that increase in surface area because child droplet formation plays a rather significant role and compensates the surface retraction effect caused due to surface tension to a much larger extent as compared to bag breakup.

Figures 5.13 and 5.14 show the evolution of normalized drag force and drag coefficient for multimode breakup mechanism. As the droplet starts to move, the drag coefficient is about 0.45 corresponding to that of flow over a sphere. Similar to bag breakup, once the droplet starts deforming laterally the drag coefficient starts to increase and reaches a maximum value. As shown in Figure 5.15 the frontal area of the water droplet increases multiple folds laterally before it breaks up. As the droplet

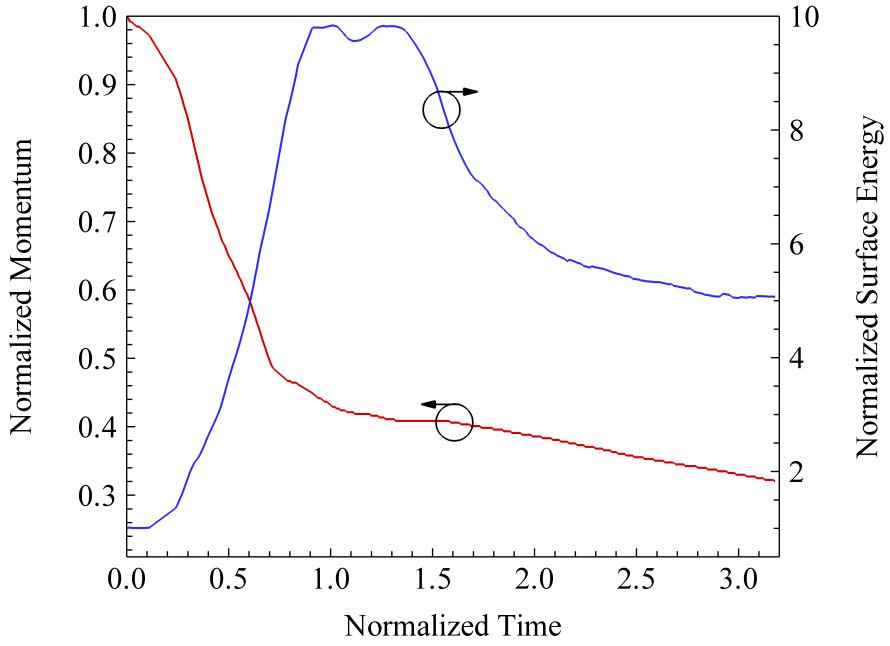

Figure 5.12. Time evolution of momentum and surface energy for $We = 365$.

starts to break up and holes and webs are developed in the parent droplet, drag coefficient starts to drop since ambient fluid can pass through the droplet without any resistance. The end of breakup process corresponds to a stationary value of surface and kinetic energies and the result is a steady distribution of child droplets. As a consequence, once the droplet breaks up completely, the drag coefficient also reaches a steady value.

5.2.3 Shear breakup

This is the most explosive breakup mode observed during this research. The droplet breaks up due to the formation of Rayleigh-Taylor (R-T) waves, which causes shear thinning of the droplet at the periphery, leading to child droplet formation. Temporal evolution of the front and bottom view of the droplet structure corresponding to $We = 1112$ is shown in Figure 5.16 and 5.17. Multimode and shear breakup phenomena differ in two ways; 1) formation of strong R-T waves on the droplet surface in case of

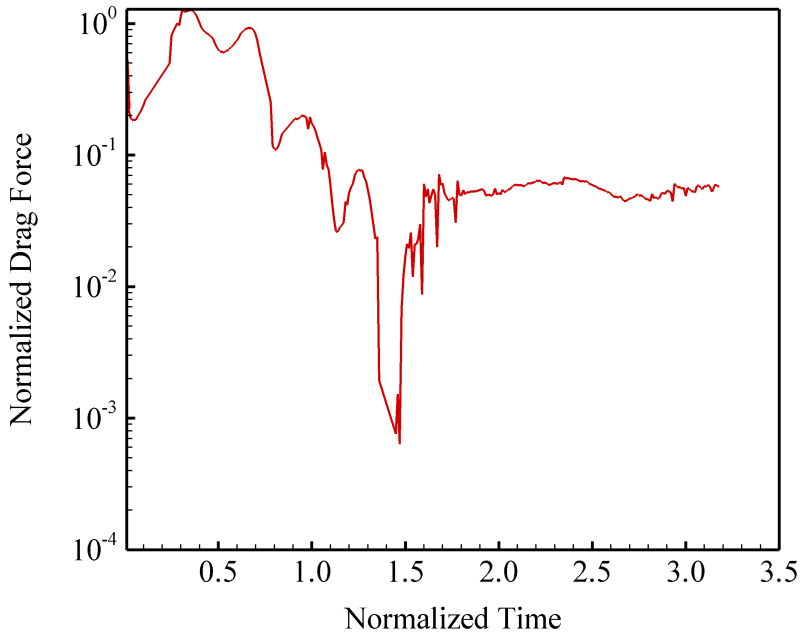

Figure 5.13. Time history of normalized drag force for multimode breakup ($We = 365$).

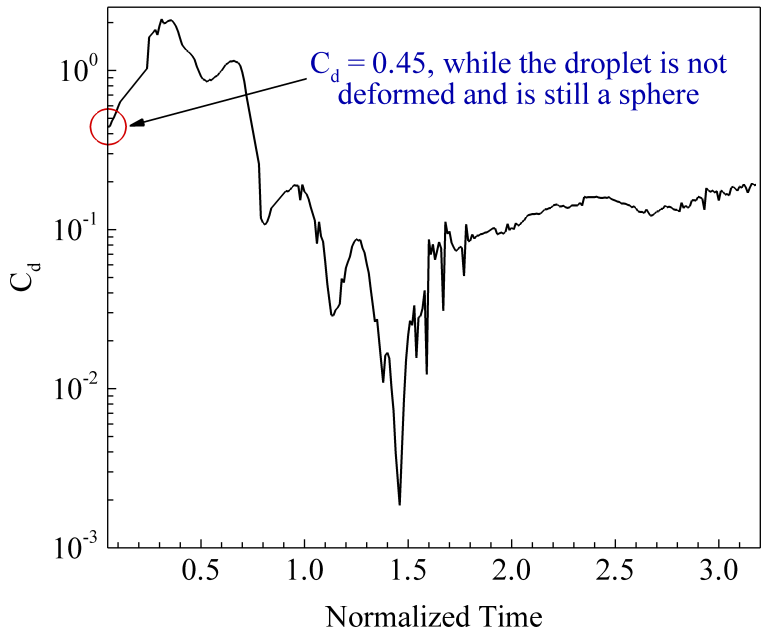

Figure 5.14. Time history of drag coefficient for multimode breakup.

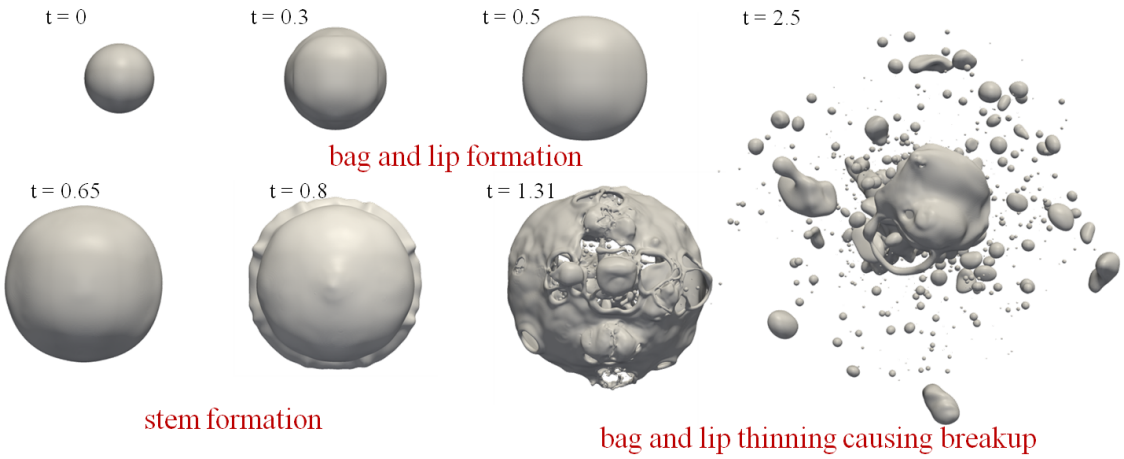

Figure 5.15. Bottom view of the temporal evolution of droplet structure for multimode breakup mechanism. $We = 365$, $Re = 29805$, $\rho_l/\rho_g = 8.29$, $t = T * U/D$.

shear breakup; and 2) formation of a hollow bag before the protrusion of stem which is unique for multimode breakup. Detailed discussion on the breakup characteristics of shear breakup mechanism can be found in Section 4.4.

Typical temporal variation of momentum and surface energy for shear breakup phenomena is shown in Figure 5.18. As is clear from the figure, the decrease in surface area is much more gradual in this case because child droplets are constantly being generated because of extremely high external forcing. The slopes of momentum and surface energy stay almost constant after $t = 1$ and $t = 1.5$ respectively. Because of this the drag coefficient tend to a stationary value at later stages of the breakup process. The variation of normalized drag force and drag coefficient for this case are shown in Figures 5.19 and 5.20.

5.3 Time averaged drag coefficient of deforming and fragmenting droplets

As pointed before, practical multiphase engineering problems are often investigated using a Eulerian-Lagrangian framework. To account for the steady-state drag force experienced by a liquid droplet in such a framework, accurate knowledge of time averaged drag coefficient is of immense importance. Average value of drag coefficient

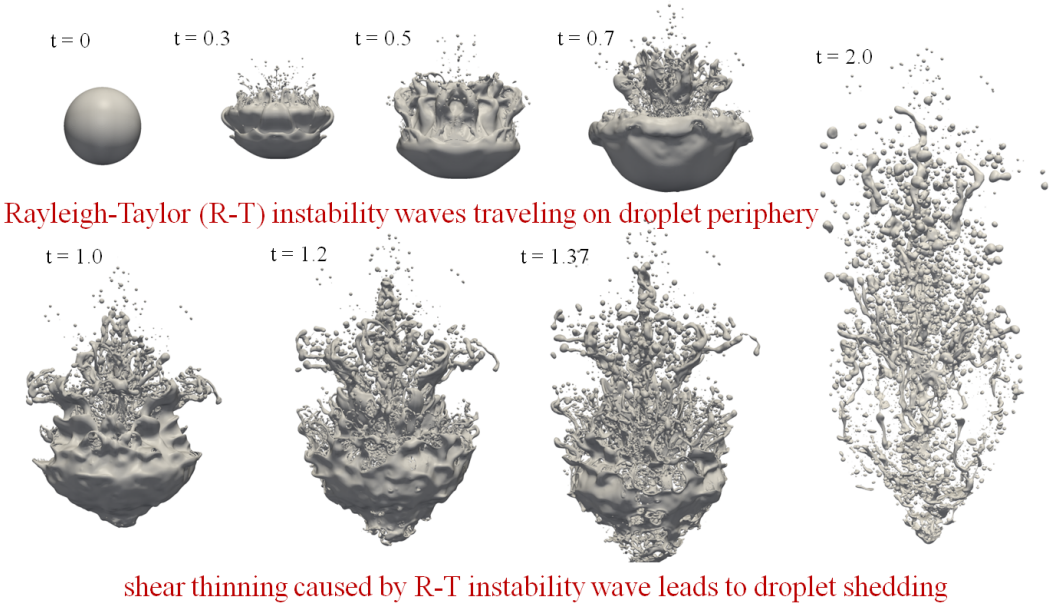

Figure 5.16. Perspective view of the temporal evolution of droplet structure for shear breakup mechanism. $We = 1112$, $Re = 52000$, $\rho_l/\rho_g = 8.29$, $t = T * U/D$.

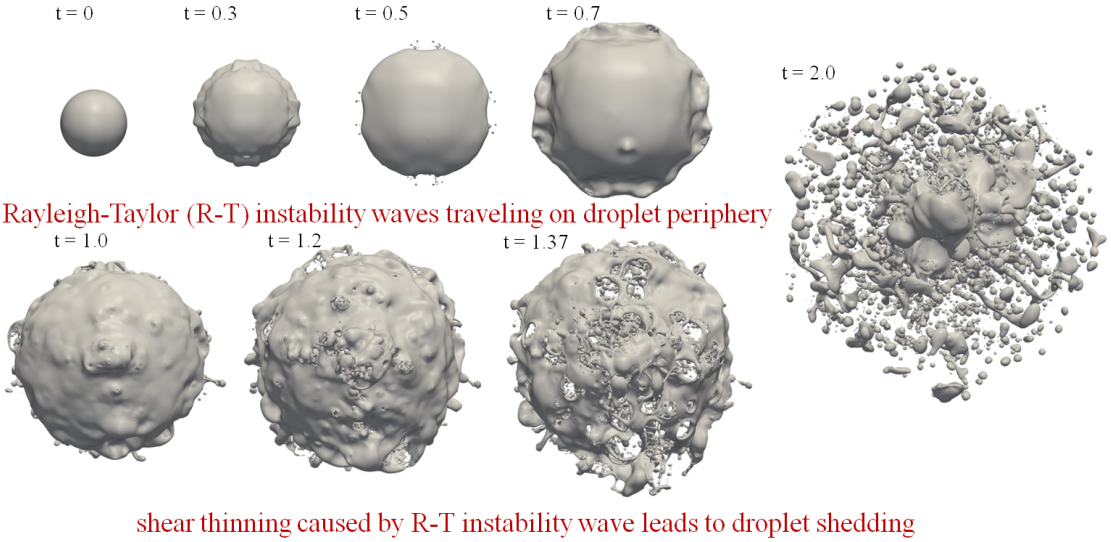

Figure 5.17. Bottom view of the temporal evolution of droplet structure for shear breakup mechanism. $We = 1112$, $Re = 52000$, $\rho_l/\rho_g = 8.29$, $t = T * U/D$.

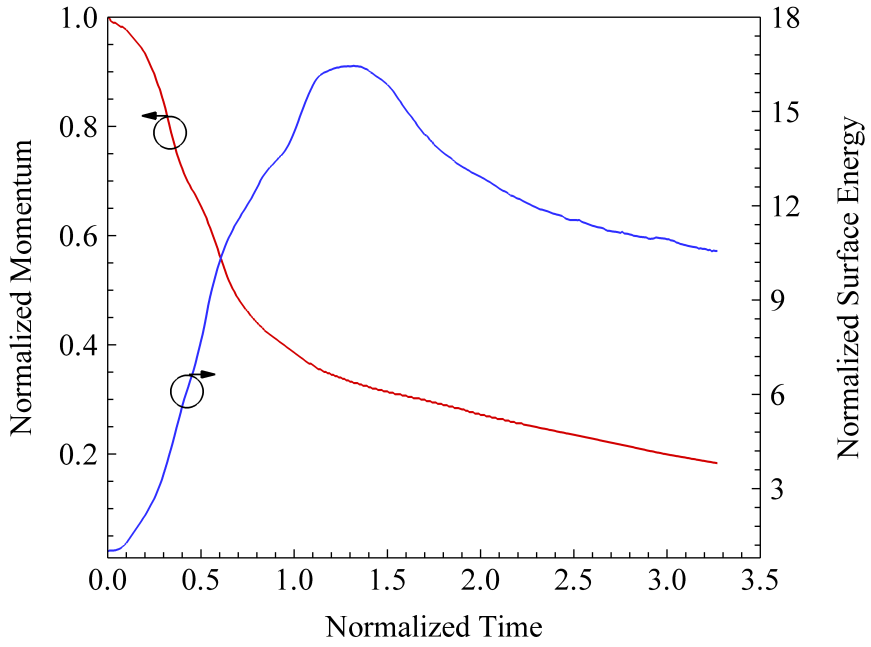

Figure 5.18. Time evolution of momentum and surface energy for $We = 1112$.

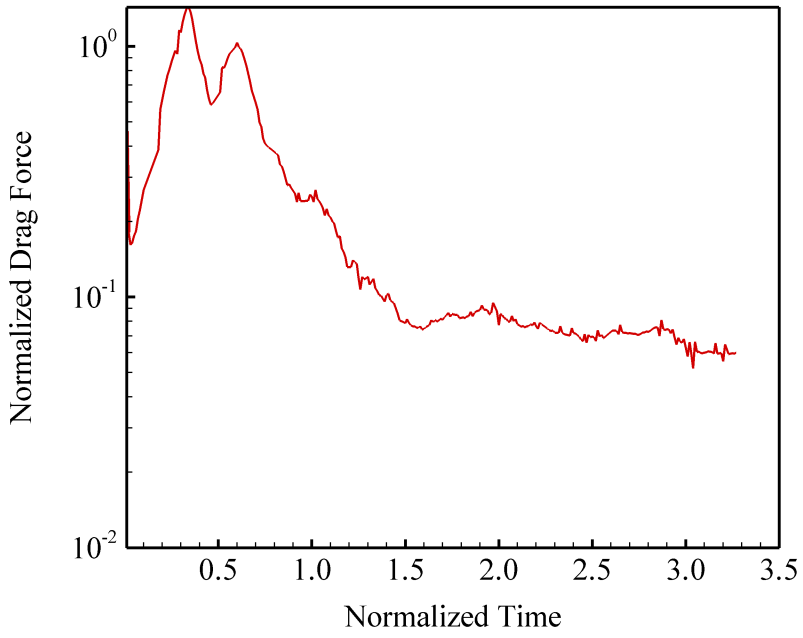

Figure 5.19. Time history of normalized drag force for shear breakup ($We = 1112$).

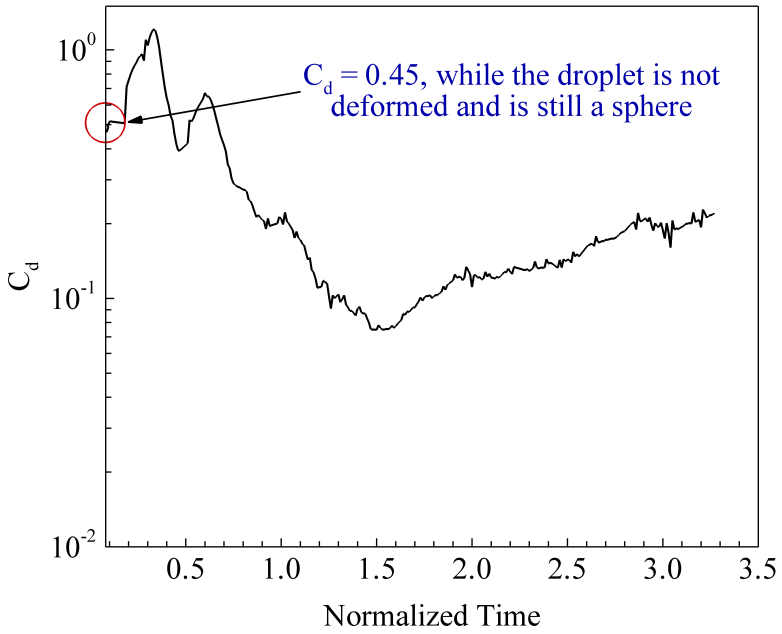

Figure 5.20. Time history of drag coefficient for shear breakup.

is obtained by calculating the area under the curve of the temporal evolution of drag coefficient, and dividing it by the droplet lifetime. Time averaged drag coefficient is calculated for a range of Weber numbers and a correlation is developed to predict the value of drag coefficient for a given Weber number. The correlation is given by:

$$\frac{C_d}{C_{d,0}} = 2We^{-0.175} \quad We > 0.1,\, Oh < 0.1 \tag{5.3}$$

The variation of time-mean drag as a function of Weber number is shown in Figure 5.21. The time averaged drag coefficient decreases as the Weber number is increased. To explain this phenomena, it is useful to look at the breakup mechanisms dominant at various Weber numbers. When the Weber number is small the breakup process usually proceeds via bag breakup mechanism and the droplet deformation before the initialization of breakup is large. In addition, the time associated with this large deformation is usually very large. This in affect corresponds to a larger drag coefficient in comparison to the processes taking place at higher Weber numbers, where fragmentation proceeds quickly. Maximum value of drag coefficient was also

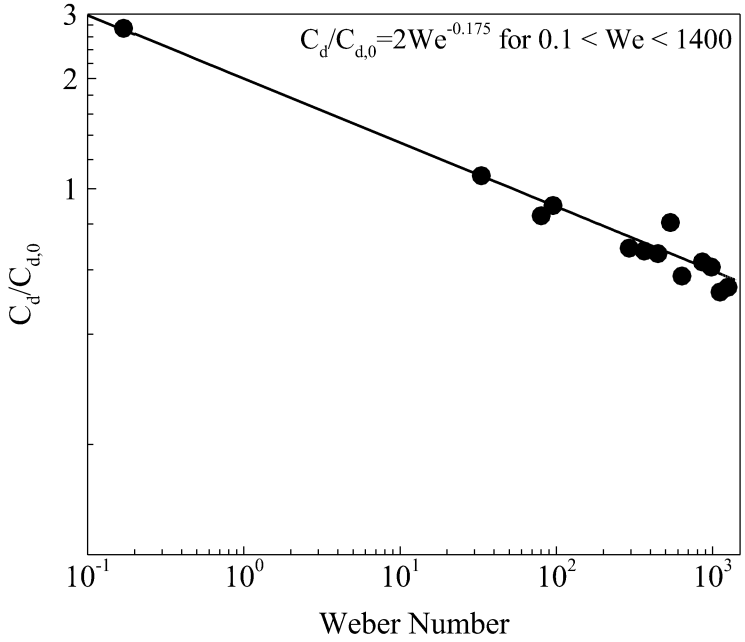

Figure 5.21. Variation of average drag coefficient with Weber number.

investigated for the range of Weber numbers investigated in this research and is shown in Table 5.1. If the value of maximum drag coefficient is linearly extrapolated for $We = 10$, we obtain a value of 2.58 which agrees closely with the value obtained by Wadhwa *et al.* (2007). The decreasing trend of the maximum and average drag coefficient was also observed in experiments conducted by Warnica *et al.* (1995*a*) although the Weber numbers studied during their experiments were very low.

The time-mean drag coefficient for fragmenting liquid droplets at different operating pressures can be predicted by using the generalized regime diagram (equation 4.1) along with the correlation developed in this section given by equation 5.3.

5.4 Concluding Remarks

In this chapter, a numerical study investigating transient deformation and breakup of liquid droplets is presented for a wide range of Weber and Reynolds numbers. As

Table 5.1. Maximum value of drag coefficient as a function of Weber number.

Weber number	**Maximum C_d**
23	2.44
33	2.56
66	2.60
80	2.58
95	2.62
292	2.15
365	2.11
447	2.10
537	2.04
636	1.75
858	1.37
981	1.33
1112	1.21
1253	1.08
1400	1.03

a droplet moves through a gaseous environment with a velocity relative to the ambient, it deforms and eventually breaks up into a number of child droplets. Temporal evolution of momentum balance and droplet structure is used to calculate the drag coefficient at each time step from first principles. Results show that the drag coefficient first increases to a maximum as the droplet frontal area increases and then decreases at the initiation of breakup. The drag coefficient reaches a steady value at the end of droplet lifetime, corresponding to the momentum retained by the droplet. A correlation to predict the time-mean drag coefficient given by, $\frac{C_d}{C_{d,0}} = 2We^{-0.175}$, is developed, which indicates that the time averaged drag coefficient decreases with Weber number. This is attributed to the physics associated with the breakup processes at different Weber numbers. This model can be used in Eulerian-Lagrangian based large scale numerical simulations of practical multiphase problems.

CHAPTER VI

BREAKUP AND DYNAMICS OF NON-NEWTONIAN LIQUID DROPLETS

6.1 Overview and Literature Review

The motivation to study non-Newtonian liquid droplet breakup stems from the various advantages gelled propellants offer as compared to traditional liquid or solid propellants in combustion systems, particularly in rocket engines. According to Natan & Rahimi (2002):

"From the atomization point of view, very little is known about the atomization mechanism of non-Newtonian fluids and even less regarding gel propellants." In addition it is noted that, *"From the combustion point of view, gels burn at a lower burning rate than non-gelled fuels and exhibit lower combustion efficiency. Secondary atomization seems to be a key parameter in order to obtain complete burning within a reasonable combustion chamber length."*

Gelled propellants are characterized by unique viscosity and chemical behavior. Their viscosity can often be modeled as a non-Newtonian fluid, where the viscosity depends on the shear rate. Density impulse, thrust modulation and energy management capabilities, offering mission cycle flexibility provided by gelled propellants is comparable to that of state-of-the-art solid and liquid propellants (Hodge *et al.*, 1999; Natan & Rahimi, 2002). Apart from performance aspects, safety and storage capabilities offered by gelled propellants are insurmountable by either liquid or solid propellants. Accidental leaks, spills and toxicity hazards caused by fuel vapors can

be avoided in feeding systems or during storage because gel surface tends to harden when in contact with gaseous atmosphere (Hodge *et al.*, 1999). Other safety features presented by gelled propellants include lower sensitivity to impact, friction and electrostatic discharge preventing any accidental ignition or uncontrolled combustion (Hodge *et al.*, 1999). In addition, gelled propellants are highly stable and have exhibited long term storage capabilities. In contrast to the various benefits of gelled propellants, their non-Newtonian rheology is also the reason of the several disadvantages with respect to their atomization, burning, phase separation, instabilities, feeding process and cost. Further details on the current understanding of gelled propellants, their rheology, flow behavior, atomization and combustion characteristics can be obtained from the review article by Natan & Rahimi (2002).

Limited literature exists on breakup of non-Newtonian liquid droplets. One of the earliest studies on non-Newtonian liquid droplets was performed by Wilcox *et al.* (1961). The study was motivated by spray from high-speed aircraft for dissemination of insecticides, which are polymeric solutions and exhibit viscoelastic behavior. A shocktube setup along with shadowgraphy, as described in Sections 1.2.1 and 1.2.3, was used in the experiments. 3 mm drops of polyisobutyl methacrylate in BIS, polyvinyl acetates in DBP and nitrocellulose in DBP were exposed to air stream at 366 m/s. It was found that the use of polymers, even in small concentrations, retards drop breakup by imparting viscoelatic properties to the fluid. Visually, most of the results exhibited breakup behavior phenomenologically similar to shear breakup for Newtonian liquids, but with the formation of stretched ligaments.

Matta & Tytus (1982) used high velocity air stream from a wind tunnel to investigate mass median diameter (MMD) of various Newtonian and viscoelastic droplets. It was found that the measured MMDs were an order of magnitude larger than what was predicted by Weiss (1959). It can be inferred from their results that non-Newtonian liquid droplets break up into much larger sizes as compared to Newtonian drops for

similar flow conditions.

Arcoumanis *et al.* (1994, 1996) conducted experiments on Newtonian and non-Newtonian liquid droplet breakup phenomena in an air jet and high-speed photography. About 16 different non-Newtonian fluids were used with diameters ranging from 2-4 mm and velocities up to 540 m/s. Only shear breakup was observed in all the experiments conducted on non-Newtonian drops. Waves were observed on the surface of droplets as they entered the air stream with the formation of elongated ligaments. As expected, total breakup time increased with increasing concentration of the thickening agent. Arcoumanis *et al.* (1996) shows intriguing photographs comparing Newtonian and non-Newtonian droplet breakup.

One of the most recent experiments on non-Newtonian droplet breakup was conducted by Lopez-Rivera & Sojka (2009); Lopez-Rivera (2010). Droplet morphology and breakup times were studied for six different solutions of carboxymethyl cellulose (CMC) in water with concentrations varying from 0.05 to 1.4 % by weight. Bag and multimode breakup mechanisms were reported with significant stretching prior to breakup. Breakup times were recorded for each breakup mode along with its variation with flow behavior index, n and the consistency index, m. Except for the breakup initialization time, all the other significant temporal events were shortened with decrease in n and m. An analytical model was developed by modifying the TAB breakup model of O'Rourke & Amsden (1987) to include the effects of shear-thinning, power-law behavior.

Non-dimensional quantities, Weber and Ohnesorge numbers, have been used by most researchers while describing their results for Newtonian liquid droplets. Contrary to this, there is no clear consensus on which non-dimensional should be used (if at all) to describe the research findings for non-Newtonian fluids. Arcoumanis *et al.* (1994, 1996) used critical speed to correlate their data. They reasoned that variation in surface tension on the drop surface, in addition to viscosity, makes the definition

of Weber and Ohnesorge numbers ambiguous. Perhaps, this is also the reason why a regime diagram similar to the one developed by Hsiang & Faeth (1995); Chou *et al.* (1997), shown in Figure 4.1 was never constructed for non-Newtonian fluids. However, recent studies by Joseph *et al.* (1999, 2002); Lopez-Rivera & Sojka (2009) and Lopez-Rivera (2010) have used Weber number to describe the breakup dynamics of shear thinning and viscoelastic droplets.

To the best of our knowledge, this is the first numerical investigation on non-Newtonian droplet breakup. In general, non-Newtonian liquids are difficult to atomize and require higher injection pressures. Since their viscosity depends on the shear rate, it is beneficial if they behave as shear-thinning, i.e., their viscosity deceases with shear rate. This situation is ideal for combustion applications since it offers the advantages of non-Newtonian nature of the propellant during storage and is also relatively easy (as compared to shear-thickening fluids for example) to atomize when subjected to appropriate injection pressure. Therefore, in this research we use 0.5% CMC water solution, which exhibits shear-thinning power-law behavior, as the working fluid and define Weber and Ohnesorge numbers similar that defined by Lopez-Rivera (2010). The main purpose of this chapter is to identify the physics underlying the breakup of non-Newtonian liquid droplets and compare the differences between Newtonian and shear-thinning non-Newtonian drop breakup in terms of basic structural phenomenology and droplet size distribution. The rest of the chapter is divided in three sections. We begin with the description of non-Newtonian fluids followed by the presentation of results and comparison with Newtonian droplet breakup. The chapter ends with concluding remarks.

6.2 Non-Newtonian Fluids

Probably the single most important characteristic of non-Newtonian fluids, which differentiates them from Newtonian liquids is their shear-rate dependent viscosity. To

understand the behavior of non-Newtonian fluids, let's consider the flow of Newtonian and non-Newtonian liquids from an orifice. Under the same pressure drop, if the non-Newtonian liquid flows out faster than the Newtonian fluid, it is called shear thinning or pseudoplastic. Their viscosity decreases with increasing shear rates. Examples of such liquids are molten polyethylene, solutions of carboxymethyl cellulose in water, polyacrylamide in water and glycerin (Bird *et al.*, 1987). In fact, shear thinning liquids are the most common non-Newtonian fluids which exhibit shear-rate dependent viscosity. On the other hand, if the flow rate of non-Newtonian liquid is much smaller than Newtonian fluid, it is called shear thickening or dilatant. Dilatants are relatively less abundant and include fairly concentrated suspensions of small particles such as suspensions of titanium dioxide in sucrose and corn starch in ethylene-glycol-water mixture. In addition to shear thinning and thickening behavior, some non-Newtonian liquids do not flow unless subjected to a critical shear stress, called the yield stress. These are called viscoplastic or Bingham fluids. Common examples of Bingham liquids are slurries, paints and cement. Still different behavior is shown by fluids which needs a yield stress but also exhibit shear thinning property (Bird *et al.*, 1987; Guillope, 2006), called Herschel-Bulkley fluids in the literature. Figure 6.1 shows the stress-strain relationship for various non-Newtonian liquids.

Several important non-Newtonian effects can be explained using the normal stress differences exhibited by polymeric liquids in shear flows. Let us consider a coordinate system where "1" denotes the flow direction, "2" is the direction of velocity variation and "3" is the neural direction. In Newtonian liquids $\tau_{11} - \tau_{22}$, the first normal stress difference and $\tau_{22} - \tau_{33}$, the second normal stress difference is zero. In contrast, for non-Newtonian fluids, the first normal stress difference is negative and much larger in magnitude as compared to the second normal stress difference (which is often positive). Extrudate swell and rod climbing nature of polymeric liquids is partially attributed to to the normal shear stress differences. A detailed discussion of how

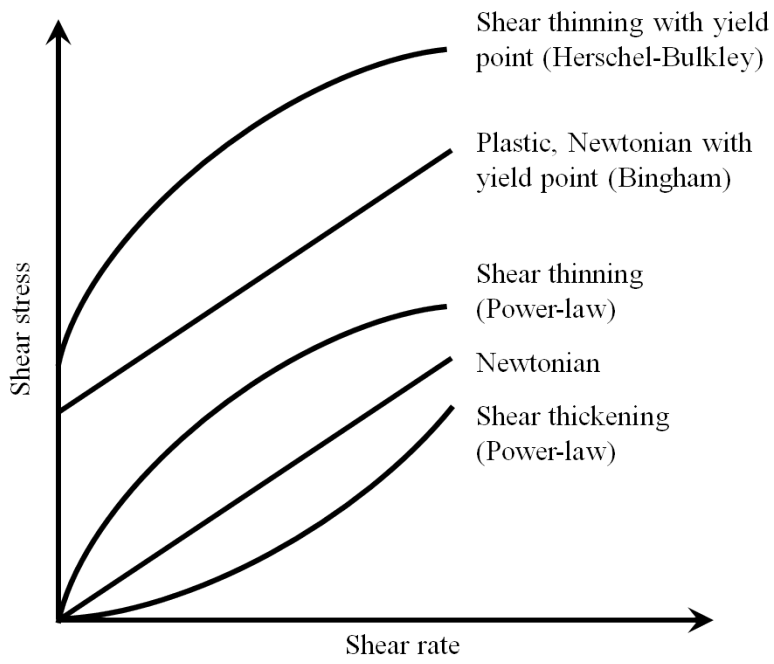

Figure 6.1. Schematic figure showing the variation of shear stress as a function of shear strain for Newtonian and common non-Newtonian fluids (Natan & Rahimi, 2002).

normal stress differences manifests themselves in various situations and effect the behavior of non-Newtonian liquids can be found in Bird *et al.* (1987).

6.2.1 Constitutive Relations

The fundamental relationship between the stress tensor and flow dependent objective variables such as pressure and rate of deformation for a liquid is called the constitutive equation. For incompressible Newtonian liquids, shear stress is linearly proportional to strain, the constant of proportionality being the dynamic viscosity (a constant for a given temperature, pressure and composition). For non-Newtonian liquids, the situation is quite different and the constitutive equation is more complex. The most commonly used stress-strain relationship in engineering practice can be categorized under generalized Newtonian fluids and takes into account the effect of shear-rate on viscosity. However, normal stress or time-dependent elastic effects cannot be explained using this model. Stress tensor at some point in space for a generalized

Newtonian fluid is related to the rate-of-strain tensor at the same point and time. In general for an incompressible generalized Newtonian fluid:

$$\begin{aligned} \widetilde{\tau} &= -\eta(\dot{\gamma})\dot{\gamma} \\ \dot{\gamma} &= \left(\nabla \mathbf{u} + (\nabla \mathbf{u})^T\right) \end{aligned} \tag{6.1}$$

If $\eta = \mu$, we recover equation 2.5. The power-law model of Ostwald (1925) and De Waele (1923) is the most widely used constitutive relation to model non-Newtonian fluids in practical problems in engineering and industry. It is a two parameter model and the definition of viscosity η is given by:

$$\eta = m\dot{\gamma}^{n-1} \tag{6.2}$$

As described before, m is called the consistency index and has units of $Pa.s^n$, while n is a non-dimensional constant and is called the flow behavior index. When $n = 1$ and $m = \mu$, Newtonian fluid is recovered. If $0 < n < 1$, the fluid behaves as shear thinning or pseudoplastic and if $n > 1$, the fluid is called dilatant or shear thickening. Table 6.1 lists the commonly used empirical relations used to model generalized Newtonian fluids. Even though, power-law models are widely used in engineering, their applicability is associated with several caveats (Bird *et al.*, 1987): (a) viscosity associated with very small shear rates cannot be defined. (b) effect of molecular weight and composition on viscosity cannot be related to m and n. (c) time history effects on viscosity, especially for viscoelatic fluids cannot be modeled using generalized Newtonian fluid constitutive relations and thus power-law models are inappropriate where the elastic response of the polymeric liquid becomes important. More sophisticated models are required to explain the behavior of viscoelastic non-Newtonian fluids. These include linear viscoelastic models such as generalized Maxwell model, shear stress models defined by differential equations such as the famous convected Jeffreys model or Oldroyd's fluid B (Oldroyd, 1950), Giesekus model (Giesekus, 1982) and integral relations for stress tensor such as Factorized Rivlin-Sawyer model. An exhaustive list

of these models, their applicability and limitations is given by Bird *et al.* (1987).

In the next section, fundamental physics governing the breakup of a 512 μm droplet of 0.5% (by wt.) CMC-water solution, given an initial velocity of 55 m/s is discussed. The corresponding Weber number is 2411 and the density ratio is 8.29. Various instabilities underlying the breakup process are discussed in detail. Child droplet size distribution for a wide range of Weber numbers ($2000 < We < 10000$) are examined and compared with that obtained after Newtonian liquid droplet breakup.

6.3 Results and Discussion

Before we begin our discussion on the breakup and dynamics of non-Newtonian liquid droplets, lets take a step back and consider 2D creeping couette flow inside two co-axial cylinders of generalized Newtonian fluids. Figure 6.2 shows the schematic of the setup and the comparison of the computed tangential velocity as a function of radial position with analytical solutions of Bird *et al.* (1987). Each of these fluids can be modeled by the relations, $\eta = \frac{\eta_0}{2\dot{\gamma}} + m\dot{\gamma}^{n-1}$. The values of η_0, m and n for the various fluids used are listed in Table 6.2. As seen in the figure, excellent agreement is obtained with theoretical results for Newtonian, power-law and Herschel-Bulkley fluids.

Recently, the current approach was used to study the primary atomization of non-Newtonian impinging jets (Chen & Yang, 2013). Numerical simulations were conducted using TS-720 silica (5 wt. %) and 981A Carbopol (0.1 wt. %) in 75/25 by vol. ethanol/water mixture. Results were compared with experiments of Fakhri (2009) for three different Weber numbers showing phenomenological similarity as shown in Figure 6.3.

As exemplified by the two numerical simulations just described, our approach is capable of handling non-Newtonian liquids with reasonable accuracy. Next, lets turn our attention to the problem in hand, deformation and fragmentation of power-law

Table 6.1. Constitutive relations for time-independent non-Newtonian liquids (Bird *et al.*, 1987; Natan & Rahimi, 2002).
η_0 : zero-shear-rate viscosity
η_∞ : infinity-shear-rate viscosity
λ : time constant
τ_0 : yield stress
$\dot{\gamma}_0$: value of $\dot{\gamma}$ where shear-thinning begins
$\tau_{1/2} : \tau = \sqrt{(\tau : \tau)/2}$ at $\eta = \eta_0/2$

Model	**Equation**
Power law	$\eta = m\dot{\gamma}^{n-1}$
Carreau-Yasuda	$\dfrac{\eta - \eta_\infty}{\eta_0 - \eta_\infty} = [1 + (\lambda\dot{\gamma})^a]^{(n-1)/a}$
Cross	$\dfrac{\eta - \eta_\infty}{\eta_0 - \eta_\infty} = [1 + (\lambda\dot{\gamma})]^{(n-1)}$
Spriggs' truncated power law	$\eta = \begin{cases} \eta_0 & \dot{\gamma} \le \dot{\gamma}_0 \\ \eta_0 \left(\dot{\gamma}/\dot{\gamma}_0\right)^{n-1} & \dot{\gamma} \ge \dot{\gamma}_0 \end{cases}$
Bingham	$\eta = \begin{cases} \infty \\ \mu_0 + \dfrac{\tau_0}{\dot{\gamma}} \end{cases}$
Ellis	$\dfrac{\eta_0}{\eta} = 1 + \left(\dfrac{\tau}{\tau_{1/2}}\right)^{n-1}$
Eyring ($\eta_1 = 0, \alpha = 1$); Powell-Eyring ($\alpha = 1$); Sutterby ($\eta_1 = 0$)	$\eta = \lambda_0\tau_0 \left(\dfrac{arcsinh\left(\lambda_0\dot{\gamma}\right)}{\lambda_0\dot{\gamma}}\right)^\alpha + \eta_1$

Table 6.2. Values of η_0, m and n for Newtonian, power-law and Herschel-Bulkley fluids.

Liquid	η_0	m	n
Newtonian	0	1	0
Power-law	0	0.08	0.5
Herschel-Bulkley	0.12	0.0672	0.5

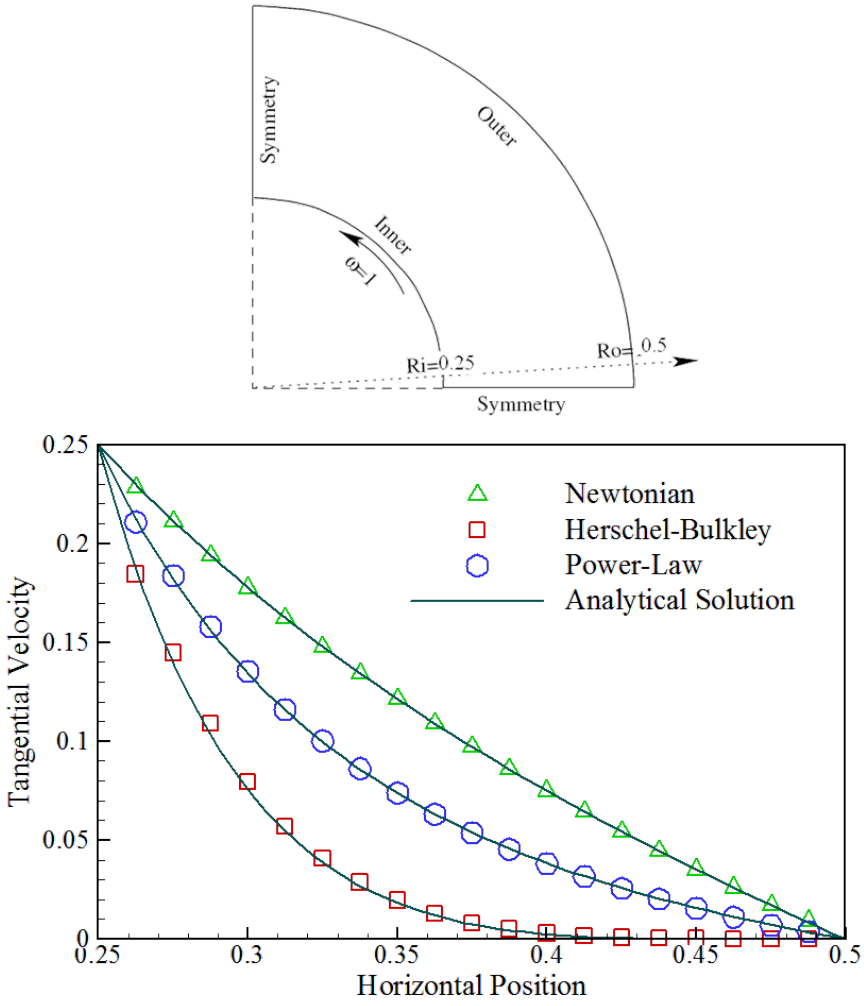

Figure 6.2. Comparison of tangential velocity as a function of radial position for various Newtonian, power-law and Herschel-Bulkley fluids with analytical solutions.

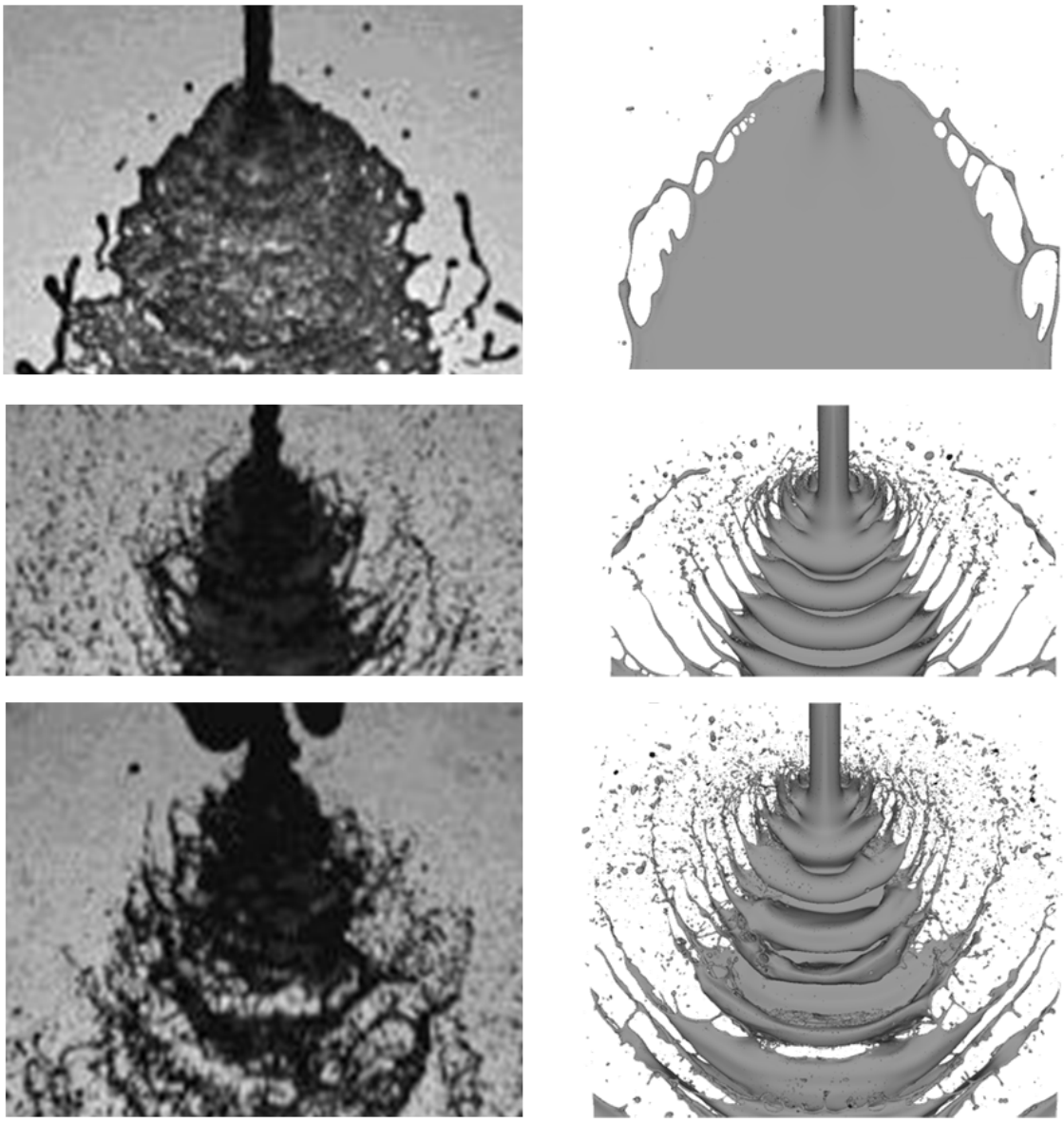

Figure 6.3. Comparison of flow patterns for non-Newtonian impinging jets at Weber numbers of 1549, 6195 and 12390 (from top to bottom). Images in the left row are obtained from experiments by Fakhri (2009), and on the right from Chen & Yang (2013) who used the present methodology for their simulations.

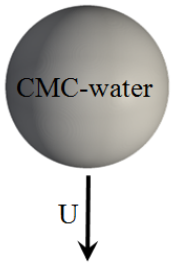

Figure 6.4. Computational setup. 0.5% (by wt.) CMC-water droplet is given an initial velocity and droplet structure and flowfield evolves in time.

drops. Similar to Newtonian droplets, we consider the breakup of a single non-Newtonian droplet which is imparted an initial velocity. The schematic of the setup is shown in Figure 6.4. CMC-water solution is treated as a power-law fluid with $m = 0.36$ and $n = 0.67$ and has a surface tension of 0.0774 N/m (Lopez-Rivera, 2010). The corresponding Weber number is 2411.

Figure 6.5 shows the temporal evolution of droplet structure for a drop of diameter 512 μm when subjected to an initial velocity of 55 m/s. As is clear from the figures, the breakup mechanism is drastically different from that of Newtonian liquids. The droplet, as it is decelerating downwards, stretches in the flow direction. The stretching quickly becomes asymmetric because the fluid is non-Newtonian and experiences different values of stresses at different regions of the droplet. This is attributed to differential shear-rates leading to different values of viscosity at different points on the droplet. Eventually two things happen: 1) droplet stretching creating a dimple and eventually a bowl, and 2) it creates a torque due to unbalanced forces and the droplet starts rotating. This process continues for a while before the bag becomes thin enough so that it breaks up. The initial breakup, shown in Figure 6.6 resembles a very common non-Newtonian phenomena, beads-on-a-string (BOAS) structure (Bhat *et al.*, 2010). This breakup creates additional non-uniformity in the shear strain experienced by the droplet leading to additional unbalanced forces. As a result, the droplet starts to rotate rapidly. This is analogous to uniformly rotating

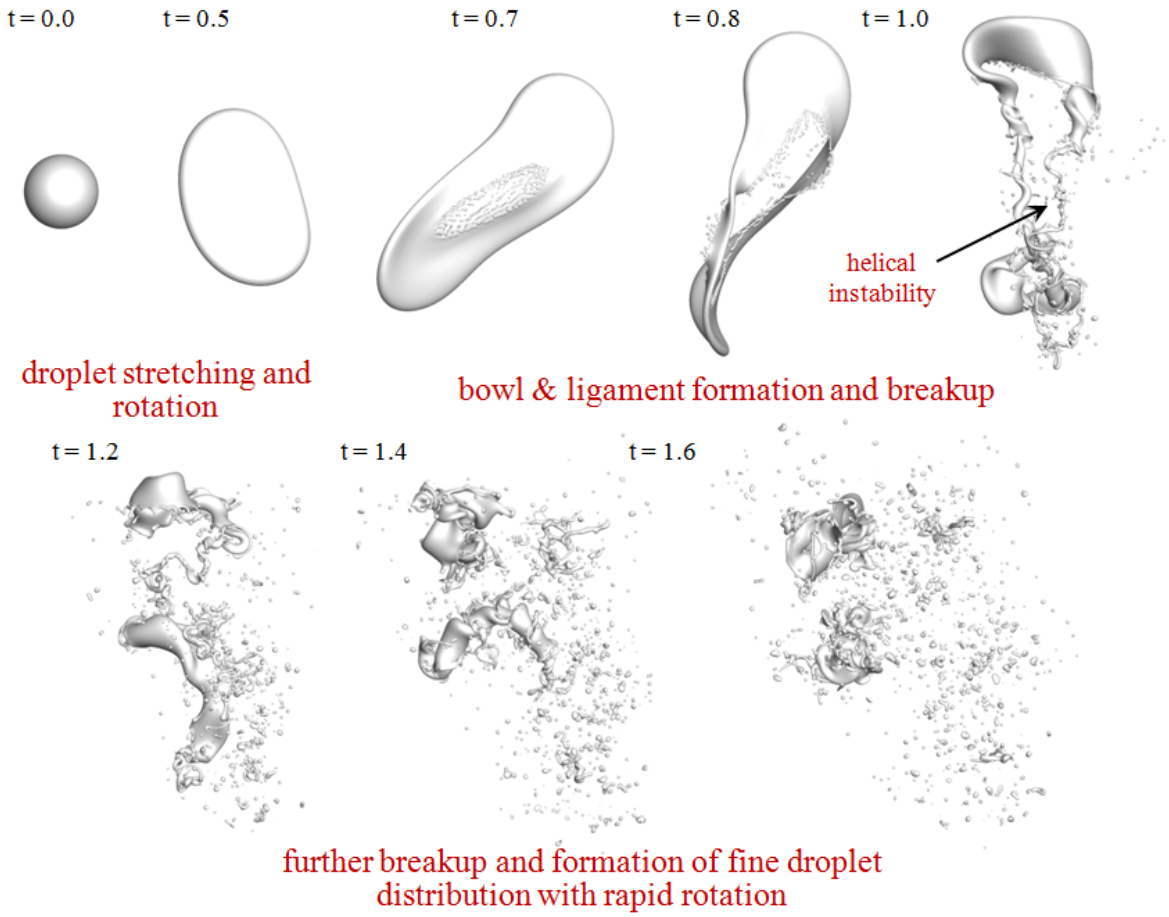

Figure 6.5. Non-Newtonian droplet breakup - $We = 2411$, $\rho_l/\rho_g = 8.29$. Perspective view of temporal evolutions of 3D droplet structure in non-dimensional time. Non-dimensional time, t = T*U/D.

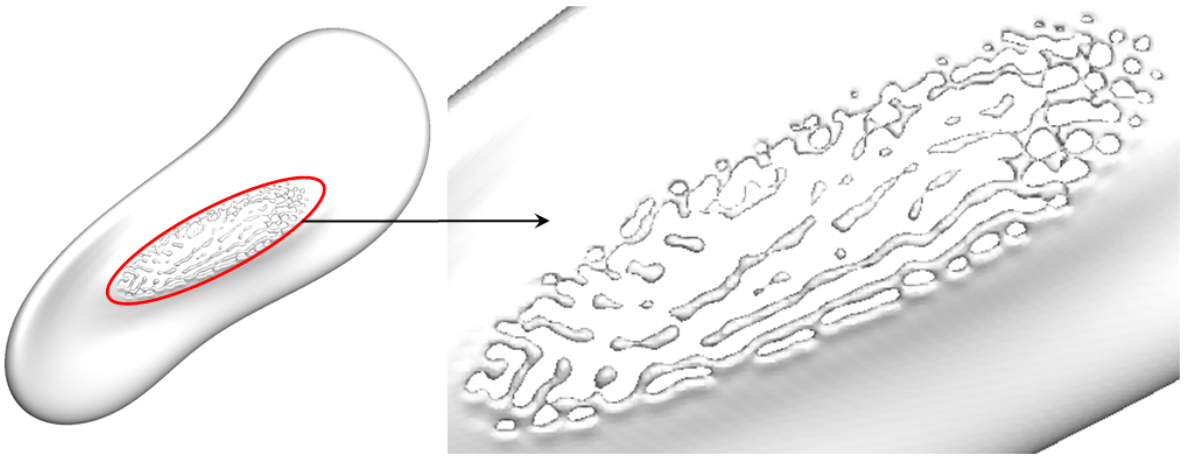

Figure 6.6. Beads-on-a-string structure during the breakup of non-Newtonian liquid drops.

liquid column where planar disturbances rotate with the stretched droplet. Twisting and growth of these disturbances evolve into helical instabilities with a central core. As it evolves in time, secondary capillary instabilities appear forming droplet ejection sites in the form of liquid knots. Primary and secondary satellite drops result from these sites due to pinching. These instabilities are shown more clearly in Figure 6.7.

Child droplet size distribution was also extracted during the breakup of non-Newtonian droplets. Figure 6.8 shows the normalized pdf of the size distribution for $We = 2411$. The size distribution follows a Gaussian distribution, shown by the black line on the figure. Interestingly, the Gaussian distribution seems to be a universal fit for the a wide range of Weber numbers, as shown in Figure 6.9. The symbols show the results obtained from the numerical simulations while the line is a Gaussian fitted to the data points. The distribution can be written as:

$$probability_{normalized} = \alpha exp\left(-\left(\frac{d-\beta}{\zeta}\right)^2\right) \text{ for } 2000 < We < 10000 \qquad (6.3)$$

where d is the representative child droplet diameter, α, β and ζ are the correlation constants. The values of correlation constants are listed in Table 6.3. Due to lack of experimental data, we could not compare our results with known correlations or data points.

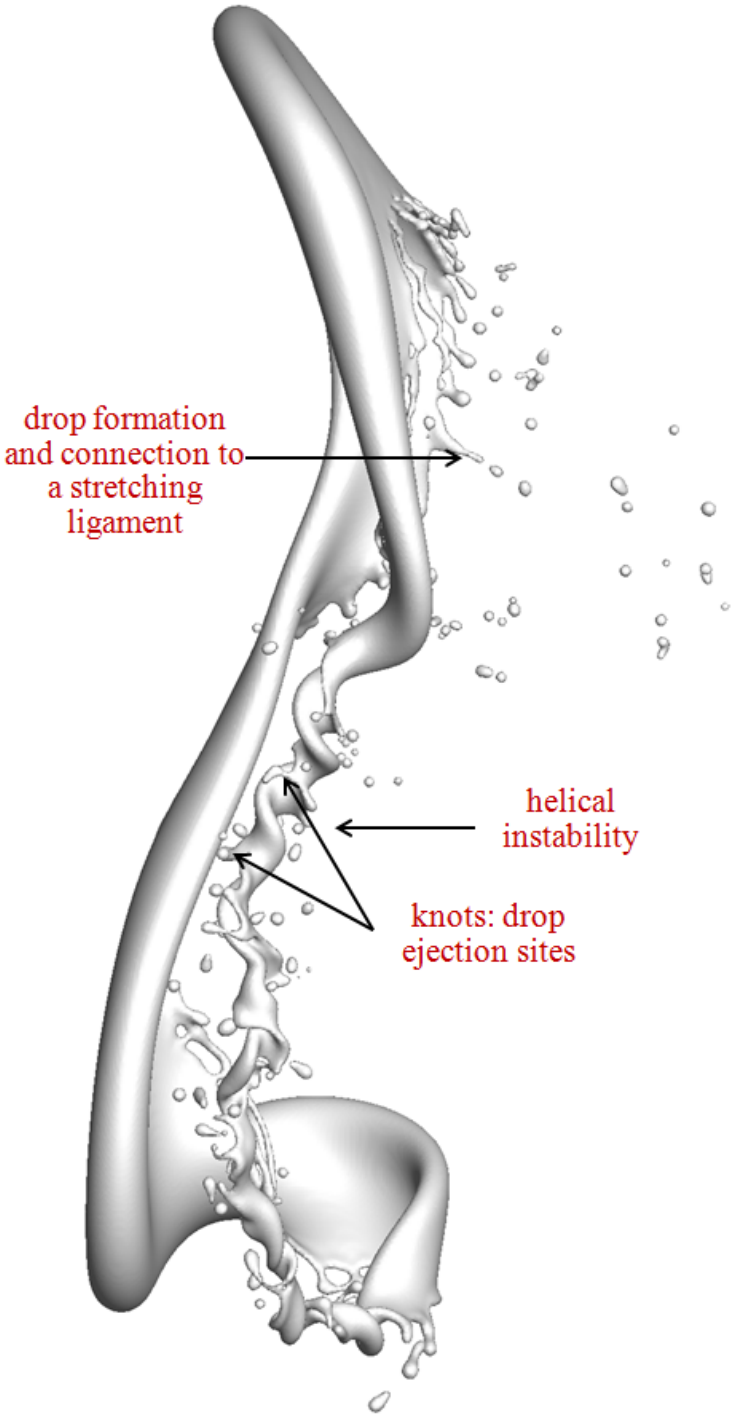

Figure 6.7. Helical instability, liquid drop ejection sites and formation of primary and satellite droplets during the breakup of non-Newtonian liquid drops.

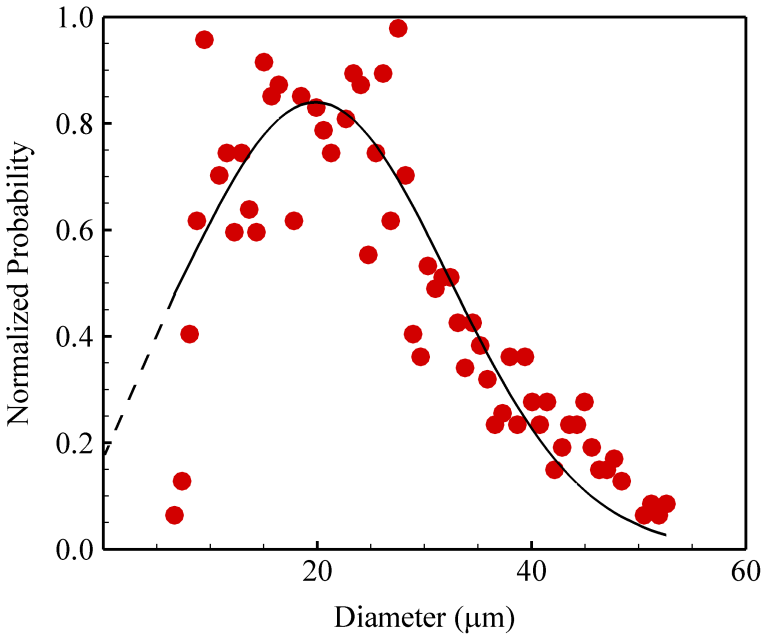

Figure 6.8. PDF of droplet size distribution for non-Newtonian droplet breakup - $We = 2411$, $\rho_l/\rho_g = 8.29$.

Table 6.3. Correlation coefficients α, β and ζ for droplet size distribution for a range of Weber numbers for non-Newtonian droplet breakup.

Weber number	α	β	ζ
2411	0.8398	19.85	17.620
3367	0.8904	11.87	7.026
4483	0.9987	10.47	6.959
5758	0.9990	10.80	5.768
7193	0.8781	8.39	6.520
9457	0.9566	14.88	6.182

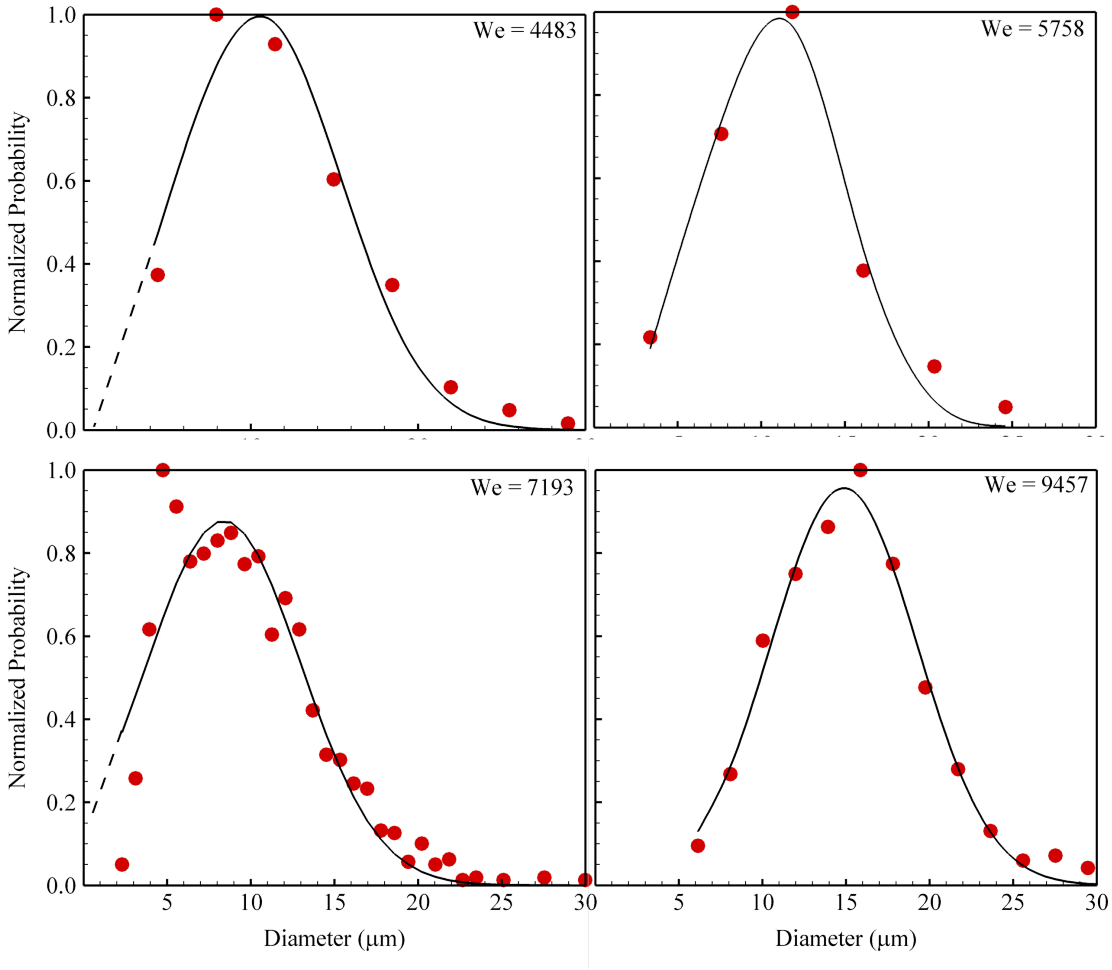

Figure 6.9. Normalized probability distribution of child droplet diameter for Weber numbers of 4483, 5758, 7193 and 9457. Symbols are results from numerical simulations and the line is a Gaussian curve.

Several differences between Newtonian and non-Newtonian droplet breakup are observed during the course of this research effort. They are summarized below:

1. The Weber numbers required for non-Newtonian droplet breakup are much larger than that required for Newtonian liquids. This is attributed to the higher viscosity of non-Newtonian liquids due to which they offer higher resistance to the inertial aerodynamic forces acting to shatter the droplet.

2. In the range of Weber numbers studied, for Newtonian drops, four distinct breakup mechanisms were observed while we observed only one kind of breakup mode for non-Newtonian droplet breakup.

3. The breakup time for non-Newtonian droplets was much larger as compared to Newtonian drops.

4. Beads-on-a-string structures were observed for non-Newtonian liquid droplet breakup while the pinch off process during Newtonian droplet breakup did not show any such structures.

5. Strong helical instabilities were observed (and caused) during the breakup of non-Newtonian drops. No such instabilities were observed for Newtonian fluids.

6. The droplet size distribution followed log-normal distribution for Newtonian droplets while it was Gaussian for non-Newtonian fluids.

6.4 Concluding Remarks

In this chapter, basic physics underlying non-Newtonian liquid droplet breakup was analysed. It was found that the droplet stretches in the flow direction until a bowl is formed which becomes thinner as time evolves. The breakup initiates with the formation of beads-in-a-string due to the non-Newtonian nature of the fluid under consideration. This is followed by rapid rotation of the droplet with the appearance

of helical instability and liquid budges, which forms the sites for primary and satellite droplet shedding. Child droplet size distribution were also examined and it was found that a Gaussian curve universally characterizes the droplets produced during non-Newtonian droplet breakup process. The differences between Newtonian and non-Newtonian droplet breakup process are also identified and summarized in the last section of the chapter.

CHAPTER VII

CONCLUDING REMARKS AND RECOMMENDATIONS FOR FUTURE RESEARCH

This chapter summarizes the major contributions of this work and outlines the recommendations for future work to improve and enhance the knowledge base of droplet breakup dynamics.

7.1 Contributions

The objectives of this research were to enhance the understanding of single droplet deformation and breakup behavior and develop correlations which can be used in large-scale Eulerian-Lagrangian LES based modeling methodologies to study systems of practical engineering interest. Consequently, the contributions of this work can be broadly divided into two categories - breakup physics and correlations. A summary of these contributions is given in the next two sections.

7.1.1 Contributions to Droplet Breakup Physics

Even though single droplet deformation and breakup has been a subject of active research for a long time, to our knowledge, this is the perhaps the first time that a comprehensive study (experiments or computations) over a broad range of operating pressure, Weber and Reynolds numbers has been conducted, highlighting the temporal evolution of details, including pressure, velocity, structure dynamics and shear stress of this complex multiphase phenomena. Previous experimental studies relied on visual graphics to describe the breakup process while computational studies were conducted either with two-dimensional or axisymmetric assumption, and thus were unable to capture all the details. For Newtonian fluids, we *quantitatively* identified

four different breakup mechanisms, oscillatory, bag, multimode and shear breakup modes, which corroborates the observations made by other researchers. Physics underlying the different breakup mechanisms is summarized in brief below:

1. Oscillatory breakup: In general, oscillatory breakup takes place at relatively low Weber numbers. After a short travelling distance, the inertial and surface tension forces compete with each other, which leads to oscillations of the droplet (and hence the name). The droplet deforms into an ellipsoid due to unequal pressure distribution on its surface. The pressure difference and vibration of the droplet further leads to the formation of a bowl, followed by a dome. This stretching, twisting and turning of the droplet continues until it breaks up due to excessive shear stress development.

2. Bag breakup: As the Weber number is increased, the breakup mechanism changes to bag breakup mode. Similar to oscillatory breakup, the droplet first deforms into a disk and then into a bowl. Because of higher inertia, the bowl is further transformed into a thin bag. The bag becomes progressively thinner and finally breaks up followed by the disintegration of the rim.

3. Multimode breakup: At progressively higher We numbers, multimode mechanism becomes the dominant mode of breakup. Due to an even higher inertial force, the bag development is accompanied by the formation of a "lip" and a stamen. The breakup process can either start from the lip or from the bag depending on the flow conditions. This is followed by the disintegration of the rim and the stem to form ligaments and child droplets.

4. Shear breakup: This is the most "explosive" breakup mode studied in this research. The droplet breaks up due to the formation of R-T waves, which enhances sheet thinning of the droplet at the periphery, eventually leading to child droplet shedding from the surface.

Another major contribution of this work to breakup physics is the quantification of breakup initialization in terms of the surface energy associated with the droplet. It was found that, irrespective of the breakup mechanism, there is a decrease in the surface energy of the droplet at the point where it starts to break. The characteristics of surface energy evolution changes from sudden to a gradual decrease at breakup initialization as the Weber number is increased. This is an important finding from a modeling standpoint and provides a universal criterion to identify the beginning of the breakup process.

Extraction of drag coefficient for deforming and fragmenting liquid droplets is another significant contribution to the physics of droplet breakup and dynamics. The drag coefficient is evaluated from first principles based on the time evolution of the droplet structure and momentum balance. For low Reynolds numbers, the calculated drag coefficient shows excellent agreement against measurements for solid spheres. As the Weber number increases, the droplet deforms laterally, and the drag coefficient increases. Further, as the droplet starts to break up with the formation of holes and web-like structures, the drag coefficient decreases. Once the breakup process is complete, the drag coefficient asymptotes to a stationary value corresponding to the momentum retained by the droplet.

Basic physics underlying non-Newtonian liquid droplet breakup was also analysed during the course of this thesis. It was found that the droplet stretches in the flow direction until a bowl is formed which becomes thinner. Breakup initiates with the formation of beads-in-a-string due to the non-Newtonian nature of the fluid under consideration. This is followed by rapid rotation of the droplet with the appearance of helical instability and liquid budges, which forms the sites for primary and satellite droplet shedding.

7.1.2 Contributions to Correlations for Droplet Breakup and Dynamics

Three major correlations developed during the present study - generalized regime diagram, child droplet size distribution and time-mean drag coefficients for a broad range of Reynolds and Weber numbers, are summarized in this section.

7.1.2.1 Generalized Regime Diagram

To the best of our knowledge, the effect of pressure on droplet breakup phenomena was comprehensively studied for the first time during this work. Based on this a generalized regime diagram was developed using the results from our research as well as results from the literature. This is conceivably one of the most important correlations developed during this research effort because it provides a way to predict the type of breakup at different operating pressure conditions for a given fluid. It was found that even though the fundamental breakup physics is independent of pressure, the critical Weber number for water droplets corresponding to different breakup regimes is dependent on pressure, in addition to the Weber number. The differences observed in critical Weber numbers at elevated pressure conditions (as compared to low pressures) can be explained using the fact that at higher pressures, the drag experienced by the droplet is much higher. This implies that the effective relative velocity between the droplet and the ambient environment reduces at a much higher rate as compared to lower pressures, i.e., the rate of change of momentum is much higher at high pressures. As a result the instantaneous Weber number decreases much faster and a higher Weber number is required to begin with for the droplet to undergo deformation and breakup (which shows phenomenological similarity to breakup process that occurs at lower pressure conditions) at higher pressure conditions. The correlation is given by:

$$We = We_{ref}\left\{1 + \frac{c}{1-p_r} We_{ref}\left[\left(\frac{\rho_g}{\rho_l}\right) - \left(\frac{\rho_g}{\rho_l}\right)_{ref}\right]\right\} \quad \text{valid for } Oh < 0.1$$
$$p_r = \frac{p}{p_{cr}},\ p_{ref} = 1atm,\ c = 0.62 \tag{7.1}$$

7.1.2.2 Droplet Size Distribution

Correlations to predict child droplet diameter distribution is another valuable addition to the literature. It was found that the normalized probability density distribution of the droplet diameters, shifted by 0.05, could be correlated using a universal log-normal distribution for $We > 300$ given by:

$$probability_{normalized} = \frac{1}{dC_1\sqrt{2\pi}} exp\left\{-\frac{(ln(d) - C_2)^2}{2C_1^2}\right\} \text{ for } We > 300,\ Oh < 0.1 \tag{7.2}$$

A theoretical, physics based correlation to predict the sauter mean diameter of the droplet size distribution, d_{32}, was also developed and is given by:

$$\frac{d_{32}}{D} = \frac{8We^{-0.72}}{C_d} \tag{7.3}$$

Generalized regime diagram and the SMD correlation were used to predict and compare the SMD of the droplet distribution a water droplet at a Weber number of 125 at 1 atm conditions. Our predictions compared very well with the experimental data, demonstrating the usability of our correlations at different pressure and operating conditions.

Child droplet size distribution were also examined for non-Newtonian droplets. It was found that a Gaussian curve universally characterizes the droplets produced during breakup process. The correlation is given by:

$$probability_{normalized} = \alpha exp\left(-\left(\frac{d-\beta}{\zeta}\right)^2\right) \text{ for } 2000 < We < 10000 \tag{7.4}$$

7.1.2.3 Time-mean Drag Coefficients

To complete the picture, a correlation to predict time-mean drag coefficients was also developed during the present research effort. Time averaged drag coefficient was calculated for a range of Weber numbers and a correlation was developed to predict

the value of drag coefficient for a given Weber number. The correlation is given by:

$$\frac{C_d}{C_{d,0}} = 2We^{-0.175} \;\; We > 0.1,\, Oh < 0.1 \tag{7.5}$$

To put all things in perspective, as noted before, the idea behind developing these correlations was to use them in an Eulerian-Lagrangian framework. To do this, let us go back and identify what is needed in an algorithm where the droplets are treated in Lagrangian coordinates. The first term on the RHS in Equation 5.1, the steady state drag force, is the most important term and is often the only term used to evaluate the droplet/particle trajectory. Given the initial droplet diameter and relative velocity, Weber number can easily be calculated, then the time mean drag coefficient correlation can be used to reasonably approximate trajectory. Once the velocity is decreased to a small fraction (approximately 5%) of the original velocity, the droplet size correlations can be used to find the distribution of the resulting child droplets. However, these correlations were developed for 100 atm pressure conditions and cannot be used otherwise. This is when the generalized regime diagram can be used to first calculate the equivalent Weber number, which can then be used to calculate the drag coefficient and child droplet diameter distributions.

7.2 Recommendations for Future Work

There are several questions, relevant to studies on Newtonian and non-Newtonian droplet breakup and dynamics, which needs to be addressed by future studies. Some of these are given below (in some sort of a logical order):

- How different is heat transfer in a deforming and fragmenting liquid droplet in a high temperature environment as compared to a solid spherical drop?

  From a computational perspective, to start with, heat transfer to/from the droplet in a high temperature quiescent atmosphere (without vaporization) is a good starting point. Preliminary results for this configuration can be seen in

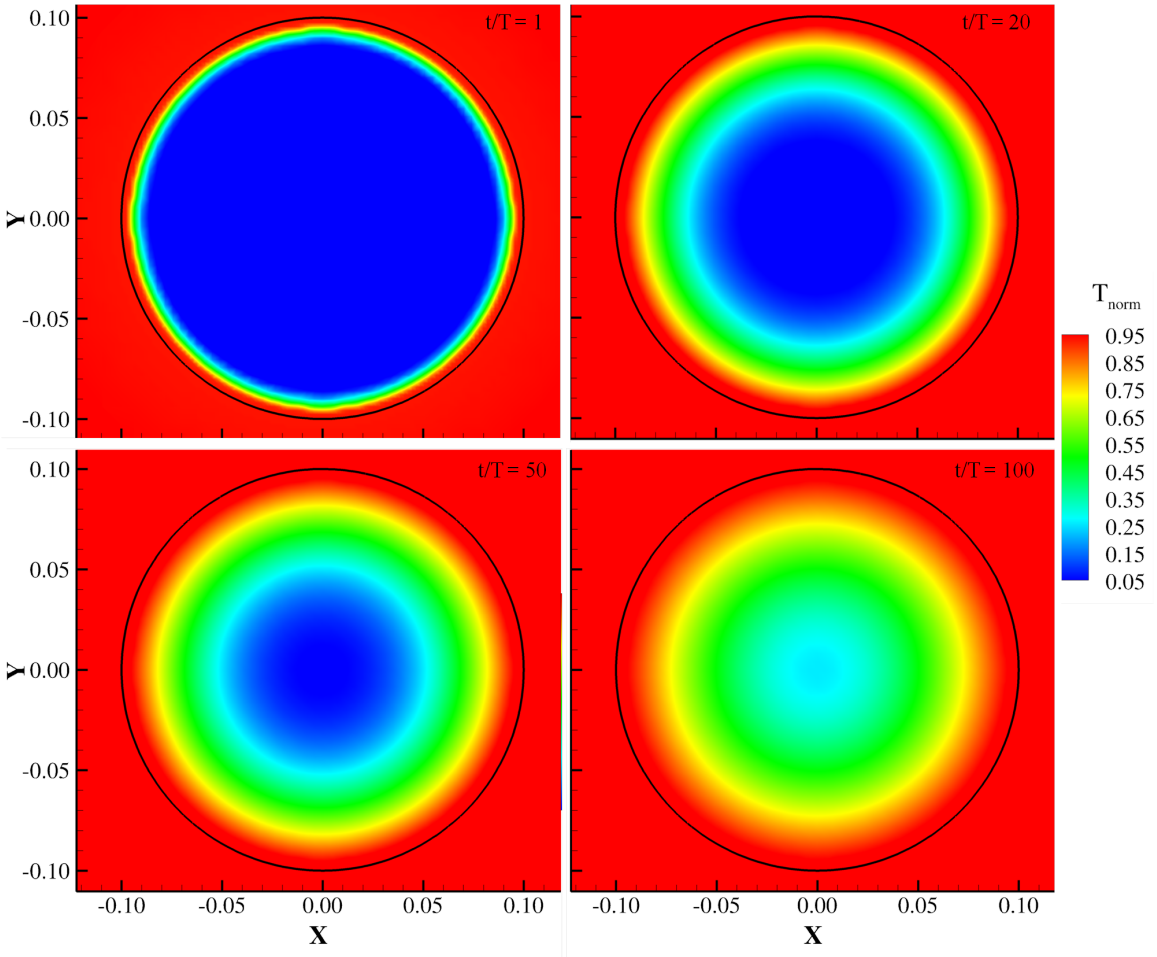

Figure 7.1. Normalized temperature contours for heat transfer in a spherical heptane droplet at 300K in a quiescent air environment at 643K at four different non-dimensional times.

Figure 7.1. The figure shows the temperature contours for a heptane droplet at 300 K in an air bath at 643 K. The normalized temperature profile at a section going through the center of the droplet is shown in Figure 7.2. Since the droplet is not undergoing any deformation, the results are compared to the theoretical solution of the heat equation in a sphere, showing excellent agreement. Once the droplet starts to deform, it will be interesting to how the heat transfer rate is affected.

- What happens to the vaporization characteristics of a deforming liquid droplet when it is subjected to a high temperature convective environment, similar to

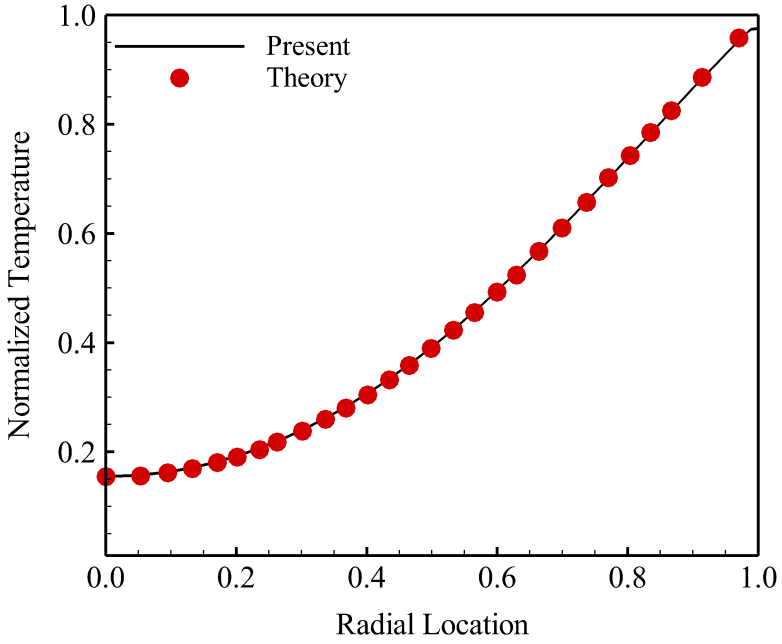

Figure 7.2. Comparison of normalized temperature profile for heat transfer in a spherical heptane droplet at 300K in a quiescent air environment at 643K with theory.

the conditions in a real combustor?

This is a question of paramount importance since it resembles the situations inside a practical combustion device. In a spherical droplet, convective heat transfer should ideally enhance vaporization but when the droplet starts to deform and break, which in turn increases the effective surface area, what will be the extent of increase of heat transfer and vaporization rate?

- Once this vaporizing droplet is ignited, how does it differ from that of a spherical droplet ignition? What does the transients look like?

- Lastly, how do the combustion characteristics change when the droplet is deforming, breaking, vaporizing and burning when subjected to an oxidizing convective environment?

This will perhaps be one of the most important, and simultaneously, most complicated phenomena to measure/compute because of the tremendously different time scales involved in the problem. It will be quite intriguing to see the combustion behavior in such a configuration.

- What will be the combustion behavior when a fuel and oxidizer (hypergolic or non-hypergolic) droplet collide with each other in a high temperature oxidizing environment?

These are some of the important question to be addressed by researchers working on droplet breakup and dynamics. Apart from this, development of generalized regime diagram (if possible) for non-Newtonian fluids is an important issue which should be addressed. It is a difficult task because of the different types of non-Newtonian fluids found in nature, governed by different constitutive relations. In addition, surface tension might change over the range of operating conditions, making the task even more challenging. Correlations for droplet size distribution and drag coefficient should also be developed for non-Newtonian fluids. They will most likely have at least two independent variables, thus increasing the degree of freedom of the system and will require much broader parametric studies for their development. Another important study which can be undertaken is the breakup of viscoelastic liquid drops using more sophisticated constitutive relations. From a computational perspective, while undertaking the above mentioned research avenues, it is imperative to develop more efficient algorithms which exhibit high parallel scalability to ensure that the numerical calculations do not become cost prohibitive and have a reasonable turn around time. We hope that this research contributed to droplet breakup and dynamics literature by providing a more thorough understanding of the breakup phenomena of liquid droplets.

REFERENCES

Abbad, M. & Souhar, M. 2004 Experimental investigation on the history force acting on oscillating fluid spheres at low reynolds number. *Physics of Fluids* **16** (10), 3808–3817.

Ackermann, G.K. & Eichler, J. 2007 *Holography: A Practical Approach*. Wiley.

Aidun, Cyrus K. & Clausen, Jonathan R. 2010 Lattice-boltzmann method for complex flows. *Annual Review of Fluid Mechanics* **42** (1), 439–472.

Alcouffe, RE, Brandt, Achi, Dendy, Jr, JE & Painter, JW 1981 The multi-grid method for the diffusion equation with strongly discontinuous coefficients. *SIAM Journal on Scientific and Statistical Computing* **2** (4), 430–454.

Alejandre, Jose, Tildesley, Dominic J. & Chapela, Gustavo A. 1995 Molecular dynamics simulation of the orthobaric densities and surface tension of water. *The Journal of Chemical Physics* **102** (11), 4574–4583.

Almedeij, Jaber 2008 Drag coefficient of flow around a sphere: Matching asymptotically the wide trend. *Powder Technology* **186** (3), 218–223.

Almgren, A., Bell, J. & Crutchfield, W. 2000 Approximate projection methods: Part i. inviscid analysis. *SIAM Journal on Scientific Computing* **22** (4), 1139–1159.

Arcoumanis, C., Khezzar, L., Whitelaw, D. S. & Warren, B. C. H. 1994 Breakup of newtonian and non-newtonian fluids in air jets. *Experiments in Fluids* **17** (6), 405–414.

Arcoumanis, C, Whitelaw, D. S. & Whitelaw, J.H. 1996 Breakup of droplets of newtonain and non-newtonain fluids. *Atomization and Sprays* **6**, 245–256.

Batchelor, G.K. 2000 *An Introduction to Fluid Dynamics*. Cambridge University Press.

Bell, John 2005 Amr for low mach number reacting flow. In *Adaptive Mesh Refinement - Theory and Applications* (ed. Tomasz Plewa, Timur Linde & V. Gregory Weirs), *Lecture Notes in Computational Science and Engineering*, vol. 41, pp. 203–221. Springer Berlin Heidelberg.

Bell, John B, Colella, Phillip & Glaz, Harland M 1989 A second-order projection method for the incompressible navier-stokes equations. *Journal of Computational Physics* **85** (2), 257 – 283.

Bellman, R. & Pennington, R.H. 1954 Effects of surface tension and viscosity on taylor instability. *Quarterly of applied mathematics* **12**, 151–162.

Berger, Marsha & Aftosmis, Michael 1998 Aspects (and aspect ratios) of cartesian mesh methods. In *Sixteenth International Conference on Numerical Methods in Fluid Dynamics* (ed. Charles-Henri Bruneau), *Lecture Notes in Physics*, vol. 515, pp. 1–12. Springer Berlin Heidelberg.

Bergmans, J., Keppens, R., Odyck, D.E.A. & Achterberg, A. 2005 Simulations of relativistic astrophysical flows. In *Adaptive Mesh Refinement - Theory and Applications* (ed. Tomasz Plewa, Timur Linde & V. Gregory Weirs), *Lecture Notes in Computational Science and Engineering*, vol. 41, pp. 223–233. Springer Berlin Heidelberg.

Berthoumieu, P., Carentz, H., Villedieu, P. & Lavergne, G. 1999 Contribution to droplet breakup analysis. *International Journal of Heat and Fluid Flow* **20**, 492–498.

Bhat, Pradeep P, Appathurai, Santosh, Harris, Michael T, Pasquali, Matteo, McKinley, Gareth H & Basaran, Osman A 2010 Formation of beads-on-a-string structures during break-up of viscoelastic filaments. *Nature Physics* **6** (8), 625–631.

Bird, R Byron, Armstrong, Robert C & Hassager, Ole 1987 *Dynamics of polymeric liquids. Vol. 1: Fluid mechanics*. John Wiley and Sons Inc., New York, NY.

Boiko, V. M., Papyrin, A. N. & Poplavskii, S. V. 1987 Dynamics of droplet breakup in shock waves. *Journal of Applied Mechanics and Technical Physics* **28** (2), 263–269.

Borisov, A. A., Gel'fand, B. E., Natanzon, M. S. & Kossov, O. M. 1981 Droplet breakup regimes and criteria for their existence. *Journal of Engineering Physics and Thermophysics* **40** (1), 44–49.

Brackbill, J.U, Kothe, D.B & Zemach, C 1992 A continuum method for modeling surface tension. *Journal of Computational Physics* **100** (2), 335 – 354.

Bremond, N. & Villermaux, E. 2006 Atomization by jet impact. *Journal of Fluid Mechanics* **549**, 273–306.

Brunauer, S. 1945 *The adsorption of gases and vapors. The Adsorption of Gases and Vapors* v. 1. Princeton University Press.

Brunauer, Stephen, Emmett, P. H. & Teller, Edward 1938 Adsorption of gases in multimolecular layers. *Journal of the American Chemical Society* **60** (2), 309–319.

Bryan, Greg L. & Norman, Michael L. 2000 A hybrid amr application for cosmology and astrophysics. In *Structured Adaptive Mesh Refinement (SAMR) Grid Methods* (ed. ScottB. Baden, NikosP. Chrisochoides, DennisB. Gannon & MichaelL.

Norman), *The IMA Volumes in Mathematics and its Applications*, vol. 117, pp. 165–170. Springer New York.

Burdon, R. S. 1940 *Surface Tension and the Spreading of Liquids*. Cambridge University Press Archive.

Chan, Tony F & Wan, WL 2000 Robust multigrid methods for nonsmooth coefficient elliptic linear systems. *Journal of Computational and Applied Mathematics* **123** (1), 323–352.

Chen, Long-Qing 2002 Phase-field models for microstructure evolution. *Annual Review of Materials Research* **32** (1), 113–140.

Chen, Shiyi & Doolen, Gary D. 1998 Lattice boltzmann method for fluid flows. *Annual Review of Fluid Mechanics* **30** (1), 329–364.

Chen, Xiaodong & Yang, Vigor 2013 Numerical simulation of primary atomization of non-newtonian impinging jets. In *ILASS Americas, 25th Annual Conference on Liquid Atomization and Spray Systems, Pittsburgh, PA*.

Chester, W., Breach, D. R. & Proudman, Ian 1969 On the flow past a sphere at low reynolds number. *Journal of Fluid Mechanics* **37** (04), 751–760.

Chhabra, R. P., Agarwal, L. & Sinha, N. K. 1999 Drag on non-spherical particles: an evaluation of available methods. *Powder Technology* **101** (3), 288–295.

Choptuik, Matthew W. 2000 Making arbitrarily small black holes: Experiences with amr in numerical relativity. In *Structured Adaptive Mesh Refinement (SAMR) Grid Methods* (ed. ScottB. Baden, NikosP. Chrisochoides, DennisB. Gannon & MichaelL. Norman), *The IMA Volumes in Mathematics and its Applications*, vol. 117, pp. 153–163. Springer New York.

Chou, W. H. & Faeth, G. M. 1998 Temporal properties of secondary drop breakup in the bag breakup regime. *International Journal of Multiphase Flow* **24**, 889–912.

Chou, W. H., Hsiang, L. P. & Faeth, G. M. 1997 Temporal properties of drop breakup in the shear breakup regime. *International Journal of Multiphase Flow* **23** (4), 651–669.

Clift, R., Grace, J. R. & Weber, M. E. 2005 *Bubbles, Drops, and Particles*. Dover Publications.

Cristini, Vittorio & Tan, Yung-Chieh 2004 Theory and numerical simulation of droplet dynamics in complex flowsa review. *Lab on a Chip* **4** (4), 257–264.

Dabora, EK 1967 Production of monodisperse sprays. *Review of Scientific Instruments* **38** (4), 502–506.

Dabora, E.K. Ragland, K.W. Ranger A.A. 1966 Two phase detonations and drop shattering studies: Second annual progress report, february 1, 1965 to january 31, 1966. *Tech. Rep.*. University of Michigan.

Dai, Z. & Faeth, G. M. 2001 Temporal properties of secondary drop breakup in the multimode breakup regime. *International Journal of Multiphase Flow* **27**, 217–236.

De Waele, A 1923 Viscometry and plastometry. *Oil Color Chem Assoc J* **6**, 33–88.

Desjardins, O & Moureau, V 2010 Methods for multiphase flows with high density ratio. In *Proceedings of the Summer, Program*.

Dombrowski, N. Dombrowski & Hooper, P. C. 1964 A study of the sprays formed by impinging jets in laminar and turbulent flow. *Journal of Fluid Mechanics* **18** (03), 392–400.

Efstathios, Michaelides & Clayton, Crowe 2005 *Basic Concepts and Definitions*, pp. 1–1–1–79. CRC Press, doi:10.1201/9781420040470.ch1.

Eotvos, R. 1886 Ueber den zusammenhang der oberflachenspannung der flussigkeiten mit ihrem molecular volumen. *Weid. Ann.* **27**, 448–459.

Faeth, G. M. 1996 Spray combustion phenomena. *Twenty-Sixth Symposium (International) on Combustion. The Combustion Institute* **26** (1), 1593–1612.

Faeth, G. M. 2002 Dynamics of secondary drop breakup - a rate controlling process in dense sprays. In *ILASS-Europe*.

Faeth, G. M., Hsiang, L. P. & Wu, P. K. 1995 Structure and breakup properties of sprays. *International Journal of Multiphase Flow* **21** (Supplement 1), 99–127.

Fakhri, Syed Abdul Khader 2009 A study on the atomization and spray characteristics of gelled simulants formed by two impinging jets. Master's thesis, The Pennsylvania State University.

Fisher, L. S. & Golovin, A. A. 2007 Motion of a droplet near an evaporating liquid-gas interface. *Physics of Fluids* **19** (3), 032101.

Flemmer, R. L. C. & Banks, C. L. 1986 On the drag coefficient of a sphere. *Powder Technology* **48**, 217–221.

Francois, Marianne M., Cummins, Sharen J., Dendy, Edward D., Kothe, Douglas B., Sicilian, James M. & Williams, Matthew W. 2006 A balanced-force algorithm for continuous and sharp interfacial surface tension models within a volume tracking framework. *Journal of Computational Physics* **213** (1), 141 – 173.

Freundlich, H. 1922 *Colloid & capillary chemistry*. E.P. Dutton & Company.

Gabitto, Jorge & Tsouris, Costas 2008 Drag coefficient and settling velocity for particles of cylindrical shape. *Powder Technology* **183** (2), 314–322.

Gefland, B. E. 1996 Droplet breakup phenomena in flows with velocity lag. *Progress in Energy and Combustion Science* **22**, 201–265.

Gel'fand, B. E., Gubin, S. A. & Kogarko, S. M. 1974 The varieties of droplet breakup behind the shock waves and their characteristic. *Journal of Engineering Physics and Thermophysics* **27** (1), 119–126.

Gerlach, D., Tomar, G., Biswas, G. & Durst, F. 2006 Comparison of volume-of-fluid methods for surface tension-dominant two-phase flows. *International Journal of Heat and Mass Transfer* **49** (34), 740 – 754.

Giesekus, H 1982 A simple constitutive equation for polymer fluids based on the concept of deformation-dependent tensorial mobility. *Journal of Non-Newtonian Fluid Mechanics* **11** (1), 69–109.

Giffen, E. & Muraszew, A. 1953 *The atomisation of liquid fuels*, 1st edn. Chapman & Hall.

Gorokhovski, Mikhael & Herrmann, Marcus 2008 Modeling primary atomization. *Annual Review of Fluid Mechanics* **40** (1), 343–366.

Greaves, Deborah 2004 A quadtree adaptive method for simulating fluid flows with moving interfaces. *J. Comput. Phys.* **194** (1), 35–56.

Greaves, Deborah M. & Borthwick, Alistair G. L. 1998 On the use of adaptive hierarchical meshes for numerical simulation of separated flows. *International Journal for Numerical Methods in Fluids* **26** (3), 303–322.

Guggenheim, E. A. 1945 The principle of corresponding states. *The Journal of Chemical Physics* **13** (7), 253–261.

Guildenbecher, D. R., Lopez-Rivera, C. & Sojka, P. E. 2009 Secondary atomization. *Experiments in Fluids* **46**, 371–402.

Guillope, C. 2006 *Non-Newtonian Fluids*. Oxford: Academic Press.

Hadamard, J. S. 1911 Mouvement permanent lent dune sphere liquid et visqueuse dans une liquid visquese. *C. R. Acad. Sci.* **152**, 1735–1738.

Han, Jaehoon & Tryggvason, Gretar 1999 Secondary breakup of axisymmetric liquid drops. i. acceleration by a constant body force. *Physics of Fluids* **11** (12), 3650–3667.

Han, Jaehoon & Tryggvason, Gretar 2001 Secondary breakup of axisymmetric liquid drops. ii. impulsive acceleration. *Physics of Fluids* **13** (6), 1554–1565.

Harlow, Francis H. & Welch, J. Eddie 1965 Numerical calculation of time-dependent viscous incompressible flow of fluid with free surface. *Physics of Fluids* **8** (12), 2182–2189.

Harvie, D.J.E., Davidson, M.R. & Rudman, M. 2006 An analysis of parasitic current generation in volume of fluid simulations. *Applied Mathematical Modelling* **30** (10), 1056 – 1066, ¡ce:title¿Special issue of the 12th Biennial Computational Techniques and Applications Conference and Workshops (CTAC-2004) held at The University of Melbourne, Australia, from 27th September to 1st October 2004¡/ce:title¿.

Hasson, David & Peck, Ralph E. 1964 Thickness distribution in a sheet formed by impinging jets. *AIChE Journal* **10** (5), 752–754.

Helenbrook, B. T. & Edwards, C. F. 2002 Quasi-steady deformation and drag of uncontaminated liquid drops. *International Journal of Multiphase Flow* **28** (10), 1631–1657.

Hinze, J. O. 1955 Fundamentals of the hydrodynamic mechanism of splitting in dispersion processes. *AIChE Journal* **1** (3), 289–295.

Hodge, K, Crofoot, T & Nelson, S 1999 Gelled propellants for tactical missile applications. *AIAA paper* **2976**, 1999.

Hsiang, L. P. & Faeth, G. M. 1992 Near-limit drop deformation and secondary breakup. *International Journal of Multiphase Flow* **18**, 635–652.

Hsiang, L. P. & Faeth, G. M. 1993 Drop properties after secondary breakup. *International Journal of Multiphase Flow* **19** (Copyright 1994, IEE), 721–35, 4569571.

Hsiang, L. P. & Faeth, G. M. 1995 Drop deformation and breakup due to shock wave and steady disturbances. *International Journal of Multiphase Flow* **21** (4), 545–560.

Huang, J. C. P. 1970 The break-up of axisymmetric liquid sheets. *Journal of Fluid Mechanics* **43** (02), 305–319.

Ibrahim, E. A. & Przekwas, A. J. 1991 Impinging jets atomization. *Physics of Fluids A* **3** (12), 2981.

Jamet, Didier, Torres, David & Brackbill, J.U. 2002 On the theory and computation of surface tension: The elimination of parasitic currents through energy conservation in the second-gradient method. *Journal of Computational Physics* **182** (1), 262 – 276.

Johnson, T. A. & Patel, V. C. 1999 Flow past a sphere up to a reynolds number of 300. *Journal of Fluid Mechanics* **378**, 19–70.

Joseph, D. D., Beavers, G. S. & Funada, T. 2002 Rayleigh-taylor instability of viscoelastic drops at high weber numbers. *Journal of Fluid Mechanics* **453**, 109–132.

Joseph, D. D., Belanger, J. & Beavers, G. S. 1999 Breakup of a liquid drop suddenly exposed to a high-speed airstream. *International Journal of Multiphase Flow* **25** (6-7), 1263–1303.

Jourdren, Herve 2005 Hera: A hydrodynamic amr platform for multi-physics simulations. In *Adaptive Mesh Refinement - Theory and Applications* (ed. Tomasz Plewa, Timur Linde & V. Gregory Weirs), *Lecture Notes in Computational Science and Engineering*, vol. 41, pp. 283–294. Springer Berlin Heidelberg.

Jung, Sungjune, Hoath, Stephen D., Martin, Graham D. & Hutchings, Ian M. 2010 Atomization patterns produced by the oblique collision of two newtonian liquid jets. *Physics of Fluids* **22** (4), 042101.

Karam, H. J. & Bellinger, J. C. 1968 Deformation and breakup of liquid droplets in a simple shear field. *Industrial and Engineering Chemisty Fundamentals* **7** (4), 576–581.

Katayama, M. 1916 *Science Reports Thoku Imperial University Ser.1* **4**, 373–.

Kelbaliyev, G. 2011 Drag coefficients of variously shaped solid particles, drops, and bubbles. *Theoretical Foundations of Chemical Engineering* **45** (3), 248–266.

Kelly, Thomas J., Adornato, Rudolph J., Bobashev, Sergei V., Golovachov, Yurii P., Van Wie, David M., Roos, F. W. & Willmarth, W. 1971 Some experimental results on sphere and disk drag. *Aiaa Journal* **9** (2), 285–291.

Khare, P., Ma, D., Chen, X. & Yang, V. 2011 Phenomenology of secondary breakup of newtonian liquid droplets. In *50th AIAA Aerospace Sciences Meeting*.

Khare, P., Ma, D., Chen, X. & Yang, V. 2012 Breakup and dynamics of liquid droplets. In *ILASS Americas, 24th Annual Conference on Liquid Atomization and Spray Systems, San Antonio, TX*.

Khare, Prashant & Yang, Vigor 2013 Drag coefficients of deforming and fragmenting liquid droplets. In *ILASS Americas, 25th Annual Conference on Liquid Atomization and Spray Systems, Pittsburgh, PA*.

Khokhlov, A.M 1998 Fully threaded tree algorithms for adaptive refinement fluid dynamics simulations. *Journal of Computational Physics* **143** (2), 519 – 543.

Khosla, S., Smith, C.E. & Throckmorton, R.P. 2006 Detailed understanding of drop atomization by gas crossflow using the volume of fluid method. In *ILASS Americas, 19th Annual Conference on Liquid Atomization and Spray Systems*.

Kim, Inchul, Elghobashi, Said & Sirignano, William A. 1998 On the equation for spherical-particle motion: effect of reynolds and acceleration numbers. *Journal of Fluid Mechanics* **367**, 221–253.

Kolev, NikolayIvanov 2012 *Drag, lift, and virtual mass forces*, chap. 2, pp. 31–85. Springer Berlin Heidelberg.

Krauss, W. E. & Leadon, B. M. 1971 Deformation fragmentation of water drops due to shock wave impact. In *AIAA Aerospace Sciences Meeting*. AIAA.

Krzeczkowski, Stefan A. 1980 Measurement of liquid droplet disintegration mechanisms. *International Journal of Multiphase Flow* **6** (3), 227–239.

Kurose, Ryoichi, Makino, Hisao, Komori, Satoru, Nakamura, Mariko, Akamatsu, Fumiteru & Katsuki, Masashi 2003 Effects of outflow from the surface of a sphere on drag, shear lift, and scalar diffusion. *Physics of Fluids* **15** (8), 2338–2351.

Lafaurie, Bruno, Nardone, Carlo, Scardovelli, Ruben, Zaleski, Stephane & Zanetti, Gianluigi 1994 Modelling merging and fragmentation in multiphase flows with {SURFER}. *Journal of Computational Physics* **113** (1), 134 – 147.

Langmuir, Irving 1918 The adsorption of gases on plane surfaces of glass, mica and platinum. *Journal of the American Chemical Society* **40** (9), 1361–1403.

Lee, C.H. & Reitz, R.D. 1999 Modeling the effects of gas density on the drop trajectory and breakup size of high-speed liquid drops. *Atomization and Sprays* **9** (5), 497–517.

Lee, C.H. & Reitz, R.D. 2000 An experimental study of the effect of gas density on the distortion and breakup mechanism of drops in high speed gas stream. *International Journal of Multiphase Flow* **26**, 229–244.

Lee, C.S. & Reitz, R.D. 2001 Effect of liquid properties on the breakup mechanism of high-speed liquid drops. *Atomization and Sprays* **11** (1), 1–19.

Lefebvre, A. H. 1988 *Atomization and Sprays*. CRC Press.

Levich, V. 1962 *Physicochemical Hydrodynamics*. Prentice Hall.

Li, Ri & Ashgriz, Nasser 2006 Characteristics of liquid sheets formed by two impinging jets. *Physics of Fluids* **18** (8), 087104.

Lin, S. P. 2003 *Breakup of Liquid Sheets and Jets*. Cambridge University Press.

Liu, Z. & Reitz, R.D. 1997 An analysis of the distortion and breakup mechanism of high speed liquid drops. *International Journal of Multiphase Flow* **23** (4), 631–650.

Lopez-Rivera, C 2010 Secondary breakup of inelastic non-newtonian liquid drops. PhD thesis.

Lopez-Rivera, C & Sojka, PE 2009 Secondary breakup of non-newtonian liquid drops. In *ICLASS 2009, 11th Triennial International Annual conference on Liquid Atomization and Spray Systems*.

Luijten, C.C.M., Bosschaart, K.J. & van Dongen, M.E.H. 1997 High pressure nucleation in water/nitrogen systems. *The Journal of Chemical Physics* **106** (19).

Mashayek, A. & Ashgriz, N. 2011 *Dynamics of Liquid Droplets*, pp. 97–123. Springer US.

Massoudi, R. & King Jr., A.D. 1974 Effect of pressure on the surface tension of water. adsorption of low molecular weight gases on water at 250c. *The Journal of Physical Chemistry* **78** (22).

Matta, J. E. & Tytus, R. P. 1982 Viscoelastic breakup in a high velocity airstream. *Journal of Applied Polymer Science* **27** (2), 397–405.

Maxey, Martin R. & Riley, James J. 1983 Equation of motion for a small rigid sphere in a nonuniform flow. *Physics of Fluids* **26** (4), 883–889.

McKinley, G. H. 2005 Visco-elasto-capillary thinning and break-up of complex fluids.

Michaelides, E. E. 2006 *Non-spherical particles, bubbles and drops*, pp. 157–190.

Miller, B., Sallam, K. A., Bingabr, M., Lin, K. C. & Carter, C. 2007 Secondary breakup of aerated liquid jets in subsonic crossflow. In *45th AIAA Aerospace Sciences Meeting*, , vol. 23, pp. 15993–16004. AIAA.

Mittal, Rajat & Iaccarino, Gianluca 2005 Immersed boundary methods. *Annual Review of Fluid Mechanics* **37** (1), 239–261.

Myers, Christopher R. 2000 The dynamics of localized coherent structures and the role of adaptive software in multiscale modeling. In *Structured Adaptive Mesh Refinement (SAMR) Grid Methods* (ed. ScottB. Baden, NikosP. Chrisochoides, DennisB. Gannon & MichaelL. Norman), *The IMA Volumes in Mathematics and its Applications*, vol. 117, pp. 111–125. Springer New York.

Natan, Benveniste & Rahimi, Shai 2002 The status of gel propellants in year 2000. *International Journal of Energetic Materials and Chemical Propulsion* **5** (1-6), 172–194.

Ockendon, J. R. & Evans, G. A. 1972 The drag on a sphere in low reynolds number flow. *Journal of Aerosol Science* **3** (4), 237–242.

Odar, Fuat & Hamilton, Wallis S. 1964 Forces on a sphere accelerating in a viscous fluid. *Journal of Fluid Mechanics* **18** (02), 302–314.

Ohnesorge, Wolfgang V. 1936 Die bildung von tropfen an dsen und die auflsung flssiger strahlen. *Zeitschrift fr Angewandte Mathematik und Mechanik* **16** (6), 355–358.

Oldroyd, J. G. 1950 On the formulation of rheological equations of state. *Proceedings of the Royal Society of London. Series A. Mathematical and Physical Sciences* **200** (1063), 523–541.

O'Rourke, P.J. & Amsden, A.A. 1987 The tab method for numerical calculation of spray droplet breakup. *SAE Technical Paper 872089* .

Ostwald, WO 1925 About the rate function of the viscosity of dispersed systems. *Kolloid Z* **36**, 99–117.

Pernice, M., Bockelie, M.J., Swensen, D. & Smith, P.J. 2000 Progress, results, and experiences in developing an adaptive solver for steady state turbulent reacting flows in industrial boilers and furnaces. In *Structured Adaptive Mesh Refinement (SAMR) Grid Methods* (ed. ScottB. Baden, NikosP. Chrisochoides, DennisB. Gannon & MichaelL. Norman), *The IMA Volumes in Mathematics and its Applications*, vol. 117, pp. 127–151. Springer New York.

Peskin, C S 1982 The fluid dynamics of heart valves: Experimental, theoretical, and computational methods. *Annual Review of Fluid Mechanics* **14** (1), 235–259.

Peskin, Charles S 2002 The immersed boundary method. *Acta numerica* **11** (0), 479–517.

Pilch, M. & Erdman, C. A. 1987 Use of breakup time data and velocity history data to predict the maximum size of stable fragments for acceleration-induced breakup of a liquid drop. *International Journal of Multiphase Flow* **13** (6), 741–757.

Popinet, S. 2003 Gerris: a tree-based adaptive solver for the incompressible euler equations in complex geometries. *Journal of Computational Physics* **190** (2), 572 – 600.

Popinet, S. 2009 An accurate adaptive solver for surface-tension-driven interfacial flows. *Journal of Computational Physics* **228**, 5838–5866.

Popinet, S. http://gfs.sourceforge.net The gerris flow solver.

Popinet, Stephane & Zaleski, Stephane 1999 A front-tracking algorithm for accurate representation of surface tension. *International Journal for Numerical Methods in Fluids* **30** (6), 775–793.

Pozrikidis, C. 1992 *Boundary Integral and Singularity Methods for Linearized Viscous Flow*. Cambridge University Press.

Prosperetti, Andrea 1981 Motion of two superposed viscous fluids. *Physics of Fluids* **24** (7), 1217–1223.

Proudman, Ian & Pearson, J. R. A. 1957 Expansions at small reynolds numbers for the flow past a sphere and a circular cylinder. *Journal of Fluid Mechanics* **2** (03), 237–262.

Pruppacher, H. R., Clair, B. P. Le & Hamielec, A. E. 1970 Some relations between drag and flow pattern of viscous flow past a sphere and a cylinder at low and intermediate reynolds numbers. *Journal of Fluid Mechanics* **44** (04), 781–790.

Quan, Shaoping & Schmidt, David P. 2006 Direct numerical study of a liquid droplet impulsively accelerated by gaseous flow. *Physics of Fluids* **18** (10), 102103–9.

Ramsay, William & Shields, John 1893 The variation of molecular surface-energy with temperature. *Philosophical Transactions of the Royal Society of London. (A.)* **184**, 647–673.

Ranger, A. A. & Nicholls, J. A. 1968 Aerodynamic shattering of liquid drop. In *AIAA 6th Aerospace Sciences Meeting*. AIAA.

Rayleigh, Lord 1878 On the instability of jets. *Proceedings of the London Mathematical Society* **s1-10** (1), 4–13.

Rayleigh, Lord 1892 Xvi. on the instability of a cylinder of viscous liquid under capillary force. *Philosophical Magazine Series 5* **34** (207), 145–154.

Ruff, G. A., Wu, P. K., Bernal, L. P. & Faeth, G. M. 1992 Continuous- and dispersed-phase structure of dense nonevaporating pressure-atomized sprays. *Journal of Propulsion and Power* **8** (2), 280–289.

Rusanov, A.I. & Prokhorov, V.A. 1996 *Interfacial Tensiometry*. Elsevier Science.

Samet, H. 1990 *Applications of Spatial Data Structures: Computer Graphics, Image Processing, and Other Areas*. Addison-Wesley Longman, Incorporated.

Sangiovanni, J. J. & Kesten, A. S. 1977 A theoretical and experimental investigation of the ignition of fuel droplets. *Combustion Science and Technology* **16** (1-2), 59–70.

Scardovelli, Ruben & Zaleski, Stephane 1999 Direct numerical simulation of free-surface and interfacial flow. *Annual Review of Fluid Mechanics* **31** (1), 567–603.

Scardovelli, Ruben & Zaleski, Stephane 2000 Analytical relations connecting linear interfaces and volume fractions in rectangular grids. *Journal of Computational Physics* **164** (1), 228 – 237.

Schlichting, H. 1979 *Boundary Layer Theory*, 7th edn. McGraw-Hill Higher Education.

Schmelzer, J.W.P., Zanotto, E.D. & Fokin, V.M. 2005 Pressure dependence of viscosity. *The Journal of Chemical Physics* **122** (7).

Sehgal, B.R., Nourgaliev, R.R. & Dinh, T.N. 1999 Numerical simulation of droplet deformation and break-up by lattice-boltzmann method. *Progress in Nuclear Energy* **34** (4), 471 – 488.

Sethian, J. A. & Smereka, Peter 2003 Level set methods for fluid interfaces. *Annual Review of Fluid Mechanics* **35** (1), 341–372.

Stokes, George Gabriel 1851 On the effect of the internal friction of fluids on the motion of pendulums. *Cambridge Philosophical Society Transactions* **IX**, 8–106.

Stone, H A 1994 Dynamics of drop deformation and breakup in viscous fluids. *Annual Review of Fluid Mechanics* **26** (1), 65–102.

Sugioka, Ken-Ichi & Komori, Satoru 2007 Drag and lift forces acting on a spherical water droplet in homogeneous linear shear air flow. *Journal of Fluid Mechanics* **570**, 155–175.

Sussman, Mark & Puckett, Elbridge Gerry 2000 A coupled level set and volume-of-fluid method for computing 3d and axisymmetric incompressible two-phase flows. *Journal of Computational Physics* **162** (2), 301 – 337.

Swamee, P. & Ojha, C. 1991 Drag coefficient and fall velocity of nonspherical particles. *Journal of Hydraulic Engineering* **117** (5), 660–667.

Taneda, Sadatoshi 1956 Experimental investigation of the wake behind a sphere at low reynolds numbers. *Journal of the Physical Society of Japan* **11** (Copyright (C) 1956 The Physical Society of Japan), 1104.

Taylor, Geoffrey 1960 Formation of thin flat sheets of water. *Proceedings of the Royal Society of London. Series A. Mathematical and Physical Sciences* **259** (1296), 1–17.

Taylor, T. D. & Acrivos, Andreas 1964 On the deformation and drag of a falling viscous drop at low reynolds number. *Journal of Fluid Mechanics* **18** (03), 466–476.

Temkin, S. & Mehta, H. K. 1982 Droplet drag in an accelerating and decelerating flow. *Journal of Fluid Mechanics* **116**, 297–313.

Theofanous, T. G., Li, G. J. & Dinh, T. N. 2004 Aerobreakup in rarefied supersonic gas flows. *Journal of Fluids Engineering* **126** (4), 516–527.

Tomboulides, Ananias G, Orszag, SA & Karniadakis, George Em 1993 Direct and large-eddy simulations of axisymmetric wakes. *AIAA paper* **546**.

Tryggvason, G. Scardovelli, R. Zaleski S. 2011 *Direct Numerical Simulation of Gas-Liquid Multiphase Flows*. Cambridge.

Turton, R. & Levenspiel, O. 1986 A short note on the drag correlation of spheres. *Powder Technology* **47**, 83–86.

Villermaux, E. 2007 Fragmentation. *Annual Review of Fluid Mechanics* **39** (1), 419–446.

Villermaux, E. & Bossa, B 2009 Single-drop fragmentation determines size distribution of raindrops. *Nature Physics* **5**, 697 – 702.

van der Waals, JD 1894 Thermodynamische theorie der kapillaritt unter voraussetzung stetiger dichtenderung. *Z. Phys. Chem* **13**, 657–725.

Wadhwa, Amrita R., Magi, Vinicio & Abraham, John 2007 Transient deformation and drag of decelerating drops in axisymmetric flows. *Physics of Fluids* **19** (11), 113301.

Warnica, W. D., Renksizbulut, M. & Strong, A. B. 1995*a* Drag coefficients of spherical liquid droplets part 1: Quiescent gaseous fields. *Experiments in Fluids* **18** (4), 258–264.

Warnica, W. D., Renksizbulut, M. & Strong, A. B. 1995*b* Drag coefficients of spherical liquid droplets part 2: Turbulent gaseous fields. *Experiments in Fluids* **18** (4), 265–276.

Weber, Constantin 1931 Zum zerfall eines flssigkeitsstrahles. *Zeitschrift fr Angewandte Mathematik und Mechanik* **11** (2), 136–154.

Weiss, Malcolm A 1959 Atomization in high velocity airstreams. *ARS Journal* **29** (4), 252–259.

Wierzba, A. & Takayama, K. 1988 Experimental investigation of the aerodynamic breakup of liquid drops. *AIAA Journal* **26** (11), 1329–1335.

Wilcox, J. D., June, R. K., Brown, H. A. & Kelley, R. C. 1961 The retardation of drop breakup in high-velocity airstreams by polymeric modifiers. *Journal of Applied Polymer Science* **5** (13), 1–6.

Wilkes, Edward D., Phillips, Scott D. & Basaran, Osman A. 1999 Computational and experimental analysis of dynamics of drop formation. *Physics of Fluids* **11** (12), 3577–3598.

Yang, V. & Anderson, W. E. 1995 *Liquid Rocket Engine Combustion Instability*, *Progress in Astronautics and Aeronautics*, vol. 169. AIAA.

Yuen, M. C. & Chen, L. W. 1976 On drag of evaporating liquid droplets. *Combustion Science and Technology* **14** (4-6), 147–154.

Zakerzadeh, S.A. 2008 Applying dynamic contact angles to a three-dimensional vof model. PhD thesis, Department of Mechanical and Industrial Engineering, University of Toronto.

Zinchenko, Alexander Z., Rother, Michael A. & Davis, Robert H. 1997 A novel boundary-integral algorithm for viscous interaction of deformable drops. *Physics of Fluids* **9** (6), 1493–1511.

Zinchenko, A. Z., Rother, M. A. & Davis, R. H. 1999 Cusping, capture, and breakup of interacting drops by a curvatureless boundary-integral algorithm. *Journal of Fluid Mechanics* **391**, 249–292.

VITA

Prashant Khare comes from a small, hilly university town, Sagar, located in the North-central part of India. After completing high school in his home town, he joined National Institute of Technology, Calicut to study Mechanical Engineering in 2001. He joined Alstom as a Lead Engineer, after graduating with a Bachelor of Technology degree with distinction in 2005. Following two years of real world experience, he returned back to school as a graduate student at Pennsylvania State University, University Park, where he conducted research on ignition and decomposition of ionic propellants and graduated with a Master of Science degree in Mechanical Engineering. Electing to pursue a doctoral degree in Aerospace Engineering, Prashant decided to join Georgia Institute of Technology and moved to Atlanta in the spring of 2009. While at Georgia Tech, he served as a reviewer for the Presidential Undergraduate Research Award for several semesters. He continues to serves the scientific community as a book reviewer for Contemporary Physics, a journal published by the Taylor & Francis Group. His Ph.D. research work on the fundamental physics of breakup and dynamics of liquid droplets was awarded the *William Robert Marshall best paper award* at ILASS-Americas' 24th Annual Conference on Liquid Atomization and Spray Systems held in May 2012 in San Antonio, TX. He will be joining Georgia Tech as a postdoctoral research fellow to continue his research on multiphase flow physics.